

HDL-TM-77-6

ADA043971

12

B.S.

# Voltage and Current Measurements in HIFX Diodes

August 1977

ments in HIFX Diodes, by Joseph D. Silverstein

DDC



No. FILE COPY  
DDC



U.S. Army Materiel Development  
and Readiness Command  
HARRY DIAMOND LABORATORIES  
Adelphi, Maryland 20783

APPROVED FOR PUBLIC RELEASE; DISTRIBUTION UNLIMITED.

**BEST**

**AVAILABLE**

**COPY**

The findings in this report are not to be construed as an official Department of the Army position unless so designated by other authorized documents.

Citation of manufacturers' or trade names does not constitute an official indorsement or approval of the use thereof.

Destroy this report when it is no longer needed. Do not return it to the originator.

UNCLASSIFIED

SECURITY CLASSIFICATION OF THIS PAGE (When Data Entered)

REPORT DOCUMENTATION PAGE		READ INSTRUCTIONS BEFORE COMPLETING FORM
1. REPORT NUMBER HDL-TM-77-6	2. GOVT ACCESSION NO.	3. RECIPIENT'S CATALOG NUMBER
4. TITLE (and Subtitle) Voltage and Current Measurements in HIFX Diodes,	5. TYPE OF REPORT & PERIOD COVERED Technical Memorandum	
7. AUTHOR(s) Joseph D. Silverstein	6. PERFORMING ORG. REPORT NUMBER	
9. PERFORMING ORGANIZATION NAME AND ADDRESS Harry Diamond Laboratories 2800 Powder Mill Road Adelphi, MD 20783	8. CONTRACT OR GRANT NUMBER(s)	
11. CONTROLLING OFFICE NAME AND ADDRESS US Army Materiel Development and Readiness Command Alexandria, VA 22333	10. PROGRAM ELEMENT, PROJECT, TASK AREA & WORK UNIT NUMBERS (12) 116p.	
14. MONITORING AGENCY NAME & ADDRESS (if different from Controlling Office)	12. REPORT DATE Aug 1977	
	13. NUMBER OF PAGES 124	
	15. SECURITY CLASS. (of this report) Unclassified	
	15a. DECLASSIFICATION/DOWNGRADING SCHEDULE	
16. DISTRIBUTION STATEMENT (of this Report)  Approved for public release; distribution unlimited.		
17. DISTRIBUTION STATEMENT (of the abstract entered in Block 20, if different from Report)		
18. SUPPLEMENTARY NOTES  HDL Project: 269E29		
19. KEY WORDS (Continue on reverse side if necessary and identify by block number) Voltage monitor Diode impedance Current monitor Electron energy spectrum Field emission diode		
20. ABSTRACT (Continue on reverse side if necessary and identify by block number) Capacitive-voltage (V) monitors and shunt-resistor (I) monitors have been fabricated for the Harry Diamond Laboratories High-Intensity Flash X Ray Facility. Sensitivities of these monitors have been measured to an accuracy of 10 percent or better by improved pulse techniques. The monitors were used to measure V and I pulses at charge voltages between 2.0 and 5.0 MV for both high- and low-impedance		

DD FORM 1473 EDITION OF 1 NOV 65 IS OBSOLETE

UNCLASSIFIED  
SECURITY CLASSIFICATION OF THIS PAGE (When Data Entered)

163 050

UNCLASSIFIED

SECURITY CLASSIFICATION OF THIS PAGE(When Data Entered)

(Z) diodes. For the high-Z diode, consisting of a hemispherical cathode and a planar anode, Z increases from 70 to 120 ohms as the cathode-anode gap is increased from 1.5 to 3.8 cm. For the low-Z diode, whose cathode and anode are both planar, Z increases from 7 to 33 ohms as the cathode-anode gap is increased from 0.4 to 1.4 cm.

Electron energy spectra calculated from the V and I pulses are in reasonable agreement with those measured previously by means of a magnetic spectrometer. There is also general agreement between the time variation of gamma dose rate calculated from the V and I pulses and that measured with a scintillator-photodiode. However, the doses obtained by integrating the calculated dose rates are, on the average, 70 percent lower than those measured with  $\text{CaF}_2:\text{Mn}$  thermoluminescent dosimeters.

ACCESSION for	
NTIS	White Section <input checked="" type="checkbox"/>
DDC	Bull Section <input type="checkbox"/>
UNANNOUNCED	<input type="checkbox"/>
JUSTIFICATION	
BY	
DISTRIBUTION/AVAILABILITY CODES	
SPECIAL	
A	

UNCLASSIFIED

SECURITY CLASSIFICATION OF THIS PAGE(When Data Entered)

## CONTENTS

	<u>Page</u>
1. INTRODUCTION . . . . .	9
2. MONITOR CALIBRATIONS AND CIRCUIT PARAMETERS . . . . .	10
2.1 Introduction . . . . .	10
2.2 HDL-Built V-Monitor Pulse Calibrations . . . . .	12
2.3 SPI-Built V-Monitor Pulse Calibrations . . . . .	20
2.4 I-Monitor Pulse Calibrations . . . . .	26
2.5 Circuit Parameter Values . . . . .	30
3. MONITOR PULSES FROM HIFX . . . . .	33
3.1 Diode Geometries and Monitors . . . . .	33
3.2 High-Impedance Pulses . . . . .	36
3.3 Low-Impedance Pulses . . . . .	41
3.4 Shorted Diode Pulses . . . . .	46
4. ANALYSIS OF MONITOR PULSES . . . . .	52
4.1 Introduction . . . . .	52
4.2 Computer Program and Data Input . . . . .	52
4.3 Diode Impedance in High-Impedance Mode . . . . .	53
4.4 Diode Impedance in Low-Impedance Mode . . . . .	67
4.5 Electron Spectra . . . . .	73
4.6 Gamma Dose Rate and Dose . . . . .	88
5. CONCLUSIONS . . . . .	91
LITERATURE CITED . . . . .	93
DISTRIBUTION . . . . .	123

## APPENDICES

A.--VOLTAGE AND CURRENT MONITORS: THEORIES OF OPERATION AND SENSITIVITY . . . . .	95
B.--PULSE SYNCHRONIZATION . . . . .	107
C.--VOLTAGE-PULSE LATE TIME PHENOMENA . . . . .	115

## FIGURES

1 HDL-built tube extension . . . . .	13
--------------------------------------	----

# FIGURES (Cont'd)

	<u>Page</u>
2 HDL-built monitor assembly . . . . .	13
3 HDL-built tube extension, monitors and tantalum target holder . . .	13
4 The 222-ohm calibration fixture for HDL-built monitors . . .	15
5 Matched 125-ohm calibration fixture for HDL-built monitors . .	16
6 HDL-built V-monitor sensitivity versus shank diameter . . . .	16
7 HDL-built V-monitor calibration data . . . . .	17
8 Schematic for calibration of HDL-built monitors . . . . .	19
9 SPI-built V monitor and pump tee mounted on HIFX machine . . .	21
10 SPI-built V monitor showing capacitor band and buckle . . . .	21
11 Transmission line cones for bench test of SPI-built monitors .	21
12 Schematic for bench-test calibration of SPI-built V and I monitors . . . . .	22
13 Input and output pulses in SPI-built monitor bench-test calibration . . . . .	22
14 In-place method for SPI-built V-monitor calibration . . . . .	23
15 Input and output pulses in SPI-built V-monitor in-place cali- bration . . . . .	24
16 SPI-built I monitor . . . . .	27
17 HDL-built I-monitor calibration pulses . . . . .	28
18 HDL-built I-monitor calibration data . . . . .	29
19 Low-impedance diode geometry . . . . .	35
20 V, I, and R traces from G = 1.5 cm hemi-plane diode . . . . .	36
21 V, I, and R traces from G = 2.1 cm hemi-plane diode . . . . .	37
22 V, I, and R traces from G = 2.8 cm hemi-plane diode . . . . .	38

# FIGURES (Cont'd)

	<u>Page</u>
23 V, I, and $\dot{R}$ traces from G = 3.8 cm hemi-plane diode . . . . .	39
24 V, I, and $\dot{R}$ traces from G = 5.8 cm hemi-plane diode . . . . .	40
25 V, I, and $\dot{R}$ pulses from G = 2.6 cm, hemi-plane diode synchro- nized by method 3 . . . . .	42
26 V, I, and $\dot{R}$ pulses from G = 2.6 cm, hemi-plane diode synchro- nized by method 3 . . . . .	43
27 V and I pulses from low-impedance diodes synchronized by method 3 . . . . .	44
28 V and I pulses from low-impedance diodes synchronized by method 3 . . . . .	45
29 Shorted-diode geometries . . . . .	48
30 Pulses from shorted high-impedance diode . . . . .	49
31 Pulses from shorted low-impedance diode . . . . .	50
32 V, I, and Z traces: uncorrected and corrected by $L \frac{dI}{dt}$ . . . . .	51
33 Peak V and I versus charge voltage for G = 1.5 cm hemi-plane diode . . . . .	55
34 Peak V and I versus charge voltage for G = 2.1 cm hemi-plane diode . . . . .	56
35 Peak V and I versus charge voltage for G = 2.6 to 2.8 cm hemi- plane diode . . . . .	57
36 Peak V and I versus charge voltage for G = 3.8 cm hemi-plane diode . . . . .	58
37 V-I characteristics for G = 1.5 cm hemi-plane diode; primary peak . . . . .	59
38 V-I characteristics for G = 1.5 cm hemi-plane diode; secondary peak . . . . .	59
39 V-I characteristics for G = 2.1 cm hemi-plane diode; primary peak . . . . .	59



# FIGURES (Cont'd)

	<u>Page</u>
40 V-I characteristics for G = 2.1 cm hemi-plane diode; secondary peak . . . . .	59
41 V-I characteristics for G = 2.6 to 2.8 cm hemi-plane diode; primary peak . . . . .	60
42 V-I characteristics for G = 2.6 to 2.8 cm hemi-plane diode; secondary peak . . . . .	60
43 V-I characteristics for G = 3.8 cm hemi-plane diode; primary peak . . . . .	60
44 V-I characteristics for G = 3.8 cm hemi-plane diode; secondary peak . . . . .	60
45 Impedance histories for G = 1.51 cm hemi-plane diode . . . . .	63
46 Impedance histories for G = 2.1 cm hemi-plane diode . . . . .	63
47 Impedance histories for G = 2.6 cm hemi-plane diode . . . . .	64
48 Impedance histories for G = 2.8 cm hemi-plane diode . . . . .	64
49 Impedance histories for G = 3.8 cm hemi-plane diode . . . . .	65
50 Impedance histories for G = 2.8 cm hemi-plane diode for various delays of V relative to I . . . . .	65
51 Peak V and I versus cathode-anode gap for low-impedance diodes . . . . .	68
52 Peak V and I versus cathode-emitter diameter for low-impedance diodes . . . . .	69
53 Impedance histories for G = 0.4 cm low-impedance diodes . . . . .	71
54 Impedance histories for G = 0.7 cm low-impedance diodes . . . . .	71
55 Impedance histories for G = 1.0 cm low-impedance diode . . . . .	72
56 Impedance histories for G = 1.2 cm low-impedance diode . . . . .	72
57 Impedance histories for G = 1.4 cm low-impedance diodes . . . . .	73
58 Electron energy spectra for G = 1.5 cm hemi-plane diode . . . . .	74

# FIGURES (Cont'd)

	<u>Page</u>
59 Electron energy spectra for G = 2.1 cm hemi-plane diode . . .	75
60 Electron energy spectra for G = 2.6 cm hemi-plane diode . . .	76
61 Electron energy spectra for G = 2.8 cm hemi-plane diode . . .	77
62 Electron energy spectra for G = 3.8 cm hemi-plane diode . . .	78
63 Electron energy spectra measured with magnetic spectrometer for G = 3.2 cm, point-plane diode . . . . .	80
64 Electron energy spectra for G = 2.8 cm hemi-plane diode for various delays of V relative to I . . . . .	81
65 Electron energy spectra for G = 0.4 cm low-impedance diodes .	83
66 Electron energy spectra for G = 0.7 cm low-impedance diodes .	84
67 Electron energy spectra for G = 1.0 cm low-impedance diode .	85
68 Electron energy spectra for G = 1.2 cm low-impedance diode .	86
69 Electron energy spectra for G = 1.4 cm low-impedance diode .	87
70 Measured and calculated gamma dose rate pulses . . . . .	89

# TABLES

I Circuit Parameter Bridge Measurements for HDL-Built Monitors . . . . .	31
II Circuit Parameter Bridge Measurements for SPI-Built Monitors . . . . .	32
III High Impedance Characteristics Based on Primary Peaks of V and I . . . . .	61
IV High-Impedance Values Based on Impedance Time Histories . . . . .	67
V Low-Impedance Values from Time Histories . . . . .	73
VI Gamma Doses at 30.5 cm from Hemisphere-Plane Diodes . . . . .	90

## 1. INTRODUCTION

The importance of voltage (V) and current (I) monitors as a diagnostic tool for pulsed-electron beam machines such as High-Intensity Flash X Ray (HIFX) is well known. Routine measurements of the kilovolt to megavolt voltages and of the tens to hundreds of kiloamperes current in the field-emission (FE) diode are necessary to monitor shot-to-shot variations in beam intensity and to detect anomalous diode behavior. The V and I measurements are especially desirable during experiments in which the setup prevents dose measurements from being made. In addition, the V and I pulses used together yield information on diode impedance (Z) and electron energy spectrum, which is useful for optimizing the diode geometry during design studies.

To achieve these capabilities for the HIFX machine, a capacitive V monitor and shunt-resistor I monitor were designed, built, and calibrated at the Harry Diamond Laboratories (HDL). These monitors have been described by Sazama and Stewart.<sup>1</sup> Also reported in that paper are some of the V and I data obtained with those monitors with HIFX operating in its hemisphere-plane high-Z mode. Subsequent modifications in the HIFX tube-mount flange made it necessary to build new V and I monitors. These monitors were built by Simulation Physics Incorporated (SPI).

The present work extended that of Sazama and Stewart in the following ways. (1) Calibrations of the HDL-built V monitor were repeated using a new fixture with the same diameter shank used in the FE tube. This avoided having to assume that the sensitivity of this V

---

<sup>1</sup>F. J. Sazama and A. G. Stewart, *Design and Testing of a Current and Voltage Monitor for HIFX*, Harry Diamond Laboratories TR-1558 (August 1971).

monitor could be predicted by the simple formula for coaxial capacitance. An analysis of the sensitivities of this V monitor measured with a number of different shank diameters showed that this assumption is questionable. (2) For each diode geometry the impedance,  $Z$ , was calculated from an appropriately computed average of  $V/I$  over that part of the pulse during which  $V$  and  $I$  vary little. In addition, for the high- $Z$  diodes (for which data were obtained over a 3-MV range in charge voltage,  $V_c$ ),  $Z$  was also obtained from plots of peak  $I$  versus peak  $V$ . (3) Electron energy spectra were calculated for each diode by integrating  $I$  over time intervals of approximately constant  $V$ . (4) Gamma dose-rate histories for many shots were calculated from  $V$  and  $I$  by means of a semiempirical formula and compared to gamma pulses obtained with a scintillator-photodiode. (5) Total gamma dose was obtained by integrating the calculated dose-rate histories, and was then compared to doses measured with  $\text{CaF}_2\text{:Mn}$  thermoluminescent dosimeters. Such a comparison was important since it afforded a type of check on the sensitivities of the  $V$  and  $I$  monitors at the megavolt and kiloampere levels.

## 2. MONITOR CALIBRATIONS AND CIRCUIT PARAMETERS

### 2.1 Introduction

The reliability of the data obtained with  $V$  and  $I$  monitors depends both on accurate calibrations and on accurate measurements of circuit values. Since both the HDL-built and the SPI-built  $V$  monitors are of the capacitor-divider type and both  $I$  monitors are of the return-current shunt type, the calibration methods discussed in appendix A are directly applicable to each of them. We show (app A) that the  $V$ -monitor sensitivity ( $K_V$ ) is given by\*

---

\*See appendix A for derivation of equations (1)--(A-5)--and (2)--(A-8).

$$K_V = \bar{K}_V \left( \frac{C_1}{\bar{C}_1} \right) \left( \frac{\bar{C}_2}{C_2} \right) \left( \frac{\bar{R}_x + 50}{R_x + 50} \right), \quad (1)$$

where

$C_1$  = shank-to-wall capacitance,

$C_2$  = thin-film capacitance, and

$R_x$  = series resistance.

The I-monitor sensitivity ( $K_I$ ) is given by

$$K_I = \bar{K}_I \left( \frac{R_p}{\bar{R}_p} \right), \quad (2)$$

where

$R_p$  = resistance formed by a band of parallel resistors.

A barred symbol denotes the value of the quantity in the calibration fixture at the time of calibration and an unbarred one denotes its value in the FE diode at the time of the machine V- and I-pulse measurements.

Pulse calibration techniques for the HDL-built monitors were described by Sazama and Stewart.<sup>1</sup> In the present work (see sect. 2.2), we found that the scaling of  $K_V$  predicted by equation (1) based on a simple calculation of  $C_1/\bar{C}_1$  was incorrect for the calibration geometry used by Sazama and Stewart. The correct scaling was therefore measured directly. To avoid any possible scaling ambiguity, a new fixture was used in which  $C_1 = \bar{C}_1$ .

<sup>1</sup>F. J. Sazama and A. G. Stewart, *Design and Testing of a Current and Voltage Monitor for HIFX*, Harry Diamond Laboratories TR-1558 (August 1971).

The fixture used to calibrate the SPI-built V monitor employed a geometry in which  $C_1 = \bar{C}_1$  for the low-impedance diode, thus yielding an unambiguous calibration for that mode. The same pulse techniques were used as were used for the HDL-built V monitor. In addition, an "in-place" method was used, which allows the V monitor to be calibrated while mounted on the machine (see sect. 2.3 for description of calibration).

Both the HDL-built and SPI-built I monitors were calibrated (see sect. 2.4); the final value of  $\bar{K}_I$  for the HDL-built I monitor represents an average over measurements made both with the calibration fixture of Sazama and Stewart and the new calibration fixture.

The effect of given changes in the monitor circuit parameters on  $K_V$  and  $K_I$  can be calculated from equations (1) and (2). Such changes are found to occur over long periods of time (see sect. 2.5).

## 2.2 HDL-Built V-Monitor Pulse Calibrations

The construction details of the HDL-built V monitor have been discussed by Sazama and Stewart.<sup>1</sup> Figures 1 and 2 show the FE tube extension on which the HDL-built V and I monitors are mounted. Figure 1 shows the curved plate on the inside of the FE tube extension. This plate and the cathode shank make up the capacitor  $C_1$  (see fig. A-1, app A). Figure 2 shows the port on which is mounted the General Radio (GR) connector for the V-monitor signal. Figure 3 shows a cross-sectional view of the HDL-built monitors together with the 3.18-cm diam cathode shank and tantalum-target anode plate used for most of the high-impedance mode measurements.

---

<sup>1</sup>F. J. Sazama and A. G. Stewart, *Design and Testing of a Current and Voltage Monitor for HIFX*, Harry Diamond Laboratories TR-1558 (August 1971).

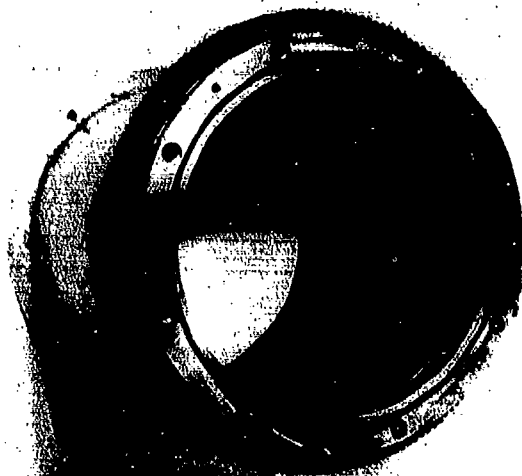


Figure 1. HDL-built tube extension showing resistors of I monitor and curved capacitor plate of V monitor.

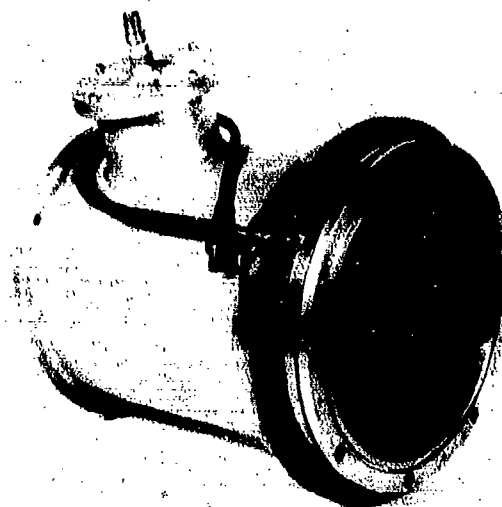


Figure 2. HDL-built monitor assembly showing belt of carbon resistors, V- and I-monitor signal cable connectors and tube extension.

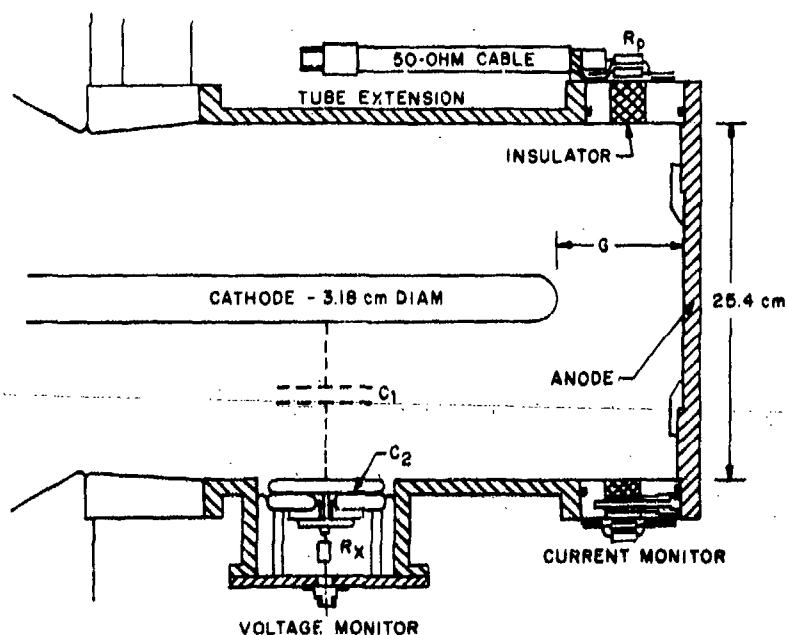


Figure 3. HDL-built tube extension, monitors and tantalum target holder (anode).

The pulse-calibration measurements on the HDL-built monitors discussed by Sazama and Stewart were performed with the calibration fixture shown in figure 4. It was assumed<sup>1</sup> that for both the calibration fixture of figure 4 and the FE diode geometry of figure 3, the appropriate values of  $C_1$  to be used in equation (1) should be based on the simple coaxial line expression,

$$C_{\text{coax}} = \frac{55.54}{\ln \frac{D}{d}} \text{ pF/m} , \quad (3)$$

where  $D$  = FE tube extension inner diameter, and  $d$  = FE shank diameter. Thus, the ratio of the capacitance,  $C$ , of the FE tube extension having a shank of  $d = 3.18$  cm to the capacitance,  $\bar{C}$ , of a calibration fixture having a shank of  $d'$  (when both have a tube extension inner diameter  $D = 25.4$  cm) is

$$\frac{C_1}{\bar{C}_1} = \frac{\ln \frac{25.4}{d'}}{\ln \frac{25.4}{3.18}} . \quad (4)$$

Then, assuming that  $R_x = \bar{R}_x$  and  $C_2 = \bar{C}_2$  for the two measurements, equation (1) yields

$$\frac{K_V(3.18)}{K_V(d')} = \frac{\ln \frac{25.4}{d'}}{\ln \frac{25.4}{3.18}} . \quad (5)$$

In particular, for the calibration fixture of figure 4,

$$\frac{K_V(3.18)}{K_V(0.64)} = \frac{\ln \frac{25.4}{0.64}}{\ln \frac{25.4}{3.18}} = 1.77 . \quad (6)$$

<sup>1</sup>F. J. Sazama and A. G. Stewart, *Design and Testing of a Current and Voltage Monitor for HIFX*, Harry Diamond Laboratories TR-1558 (August 1971).



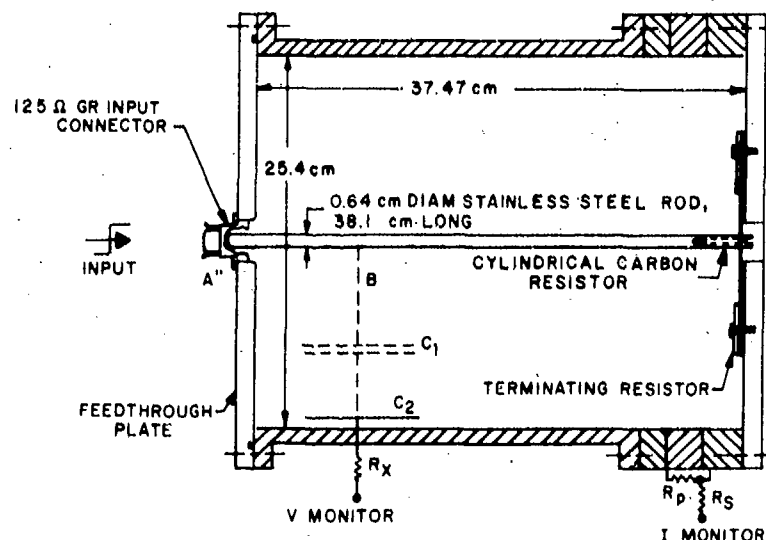


Figure 4. The 222-ohm calibration fixture for HDL-built monitors.

One of the main purposes of the new calibration fixture for the HDL-built monitors was to test equation (5) empirically. The new fixture is shown in figure 5 with a 3.18-cm diam shank, i.e., the same size shank as that used in the FE diode shown in figure 3. However, additional plastic holding rings were made to accommodate shanks having diameters of 0.64, 1.27, 1.91, and 2.54 cm. Calibration pulses were obtained for all these shank diameters, as well as for 3.18 cm, and V-monitor sensitivities were measured for each.\* Figure 6 shows the data plotted as  $K_V(3.18 \text{ cm})/K_V(d)$  versus  $d$ . The solid curve is a plot of the expression in equation (5). Agreement is seen to be satisfactory for the three largest diameters but not for the 0.64-cm diameter. Whereas equation (5) predicts 1.77, the measured value is  $2.15 \pm 0.2$ . Therefore, the appropriate ratio to be used for the application of equation (1) to the V-monitor calibration data of Sazama and Stewart is

$$\frac{C_1}{\bar{C}_1} = 2.15 . \quad (7)$$

\*Many of the calibration measurements described in this and following sections were performed by C. G. Casar of HIFX staff.

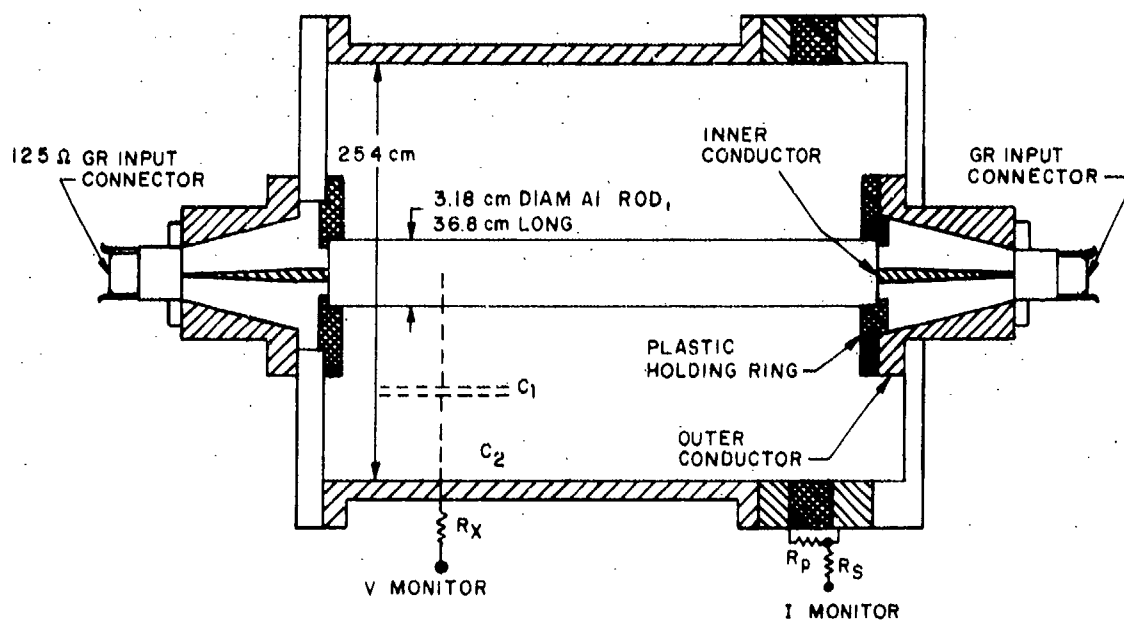


Figure 5. Matched 125-ohm calibration fixture for HDL-built monitors.

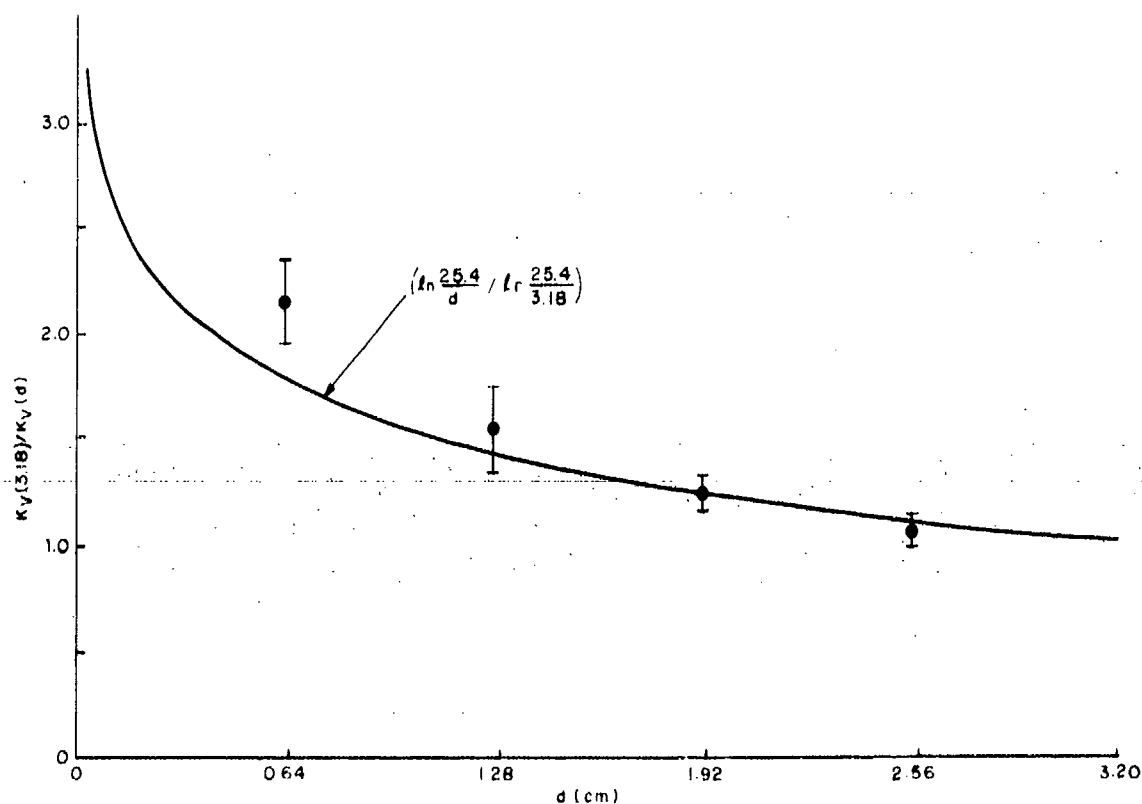


Figure 6. HDL-built V-monitor sensitivity versus shank diameter.

Those data, after being multiplied by the above ratio and also being normalized to  $R_x = 485$  ohms in the manner prescribed by equation (1), are represented by the closed circles of figure 7.

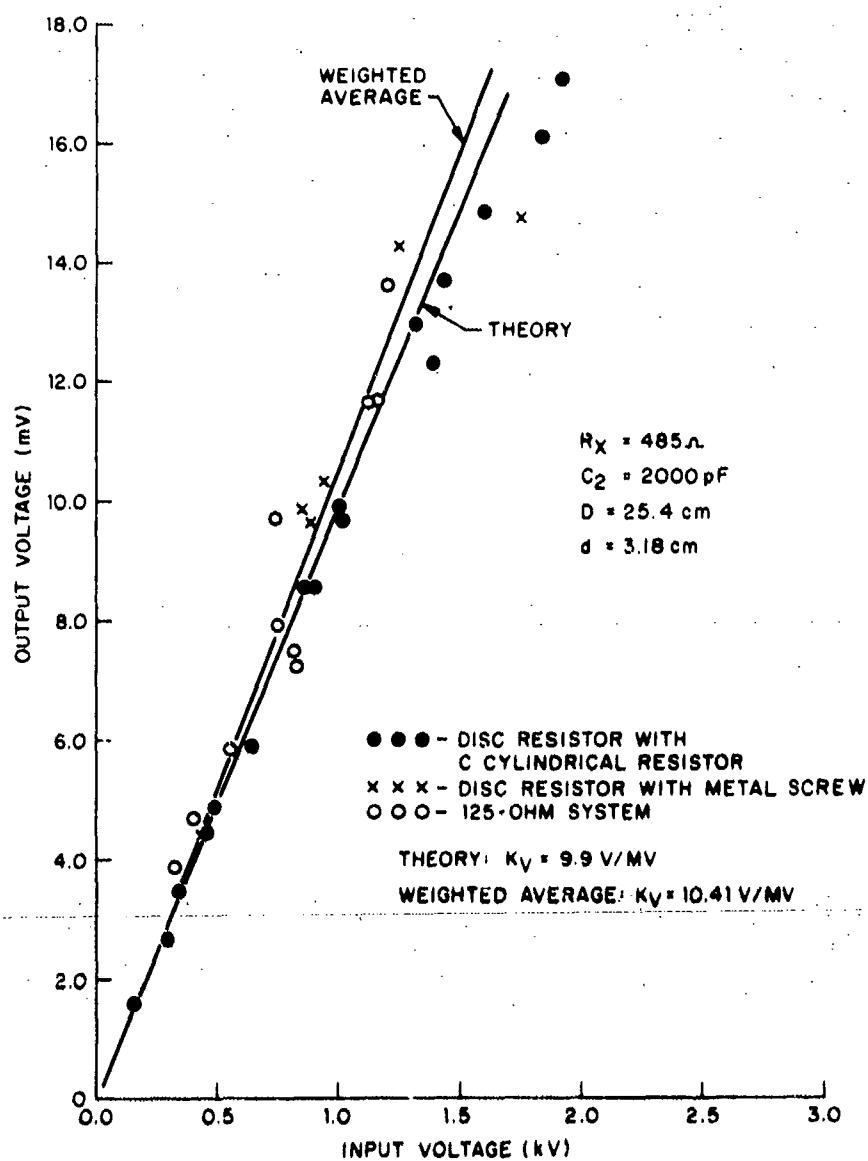


Figure 7. HDL-built V-monitor calibration data.

A design feature of the new calibration fixture (fig. 5) not present in the old fixture (fig. 4) is the impedance matching between the coaxial geometry formed by the shank and FE tube extension i.d. and that of the 125-ohm GR connector. In the old fixture, the transition between the two geometries is abrupt. In the new one, the transition is made by means of approximately tapered inner and outer conductors for each shank. For the 3.18-cm diam shank, the fixture geometry results in a purely "125-ohm system," because for this diameter the coaxial impedance is

$$Z_{\text{coax}} = 60 \ln \frac{25.4}{3.18} \text{ ohms} = 125 \text{ ohms} . \quad (8)$$

Another design feature of the new calibration fixture is the presence of both an input and an output GR connector. This allows the input pulse to be observed simultaneously with the output pulse without the use of a sampling tee. The setup used for obtaining calibration pulses with the new fixture is shown in figure 8. With the 50-ohm pulser matched to the calibration fixture with an N50/N125 matching element, and the output of the fixture coupled directly to the Tektronix 519 scope input connector, the pulse traverses a completely reflection-free path when a 3.18-cm diam shank is used in the fixture. The input pulse amplitude, however, had to be limited to 1500 V to prevent breakdowns at the narrow ends of the tapers in the calibration fixture. In this one respect the new fixture (fig. 5) was inferior to the old one (fig. 4), which could accept input-pulse amplitudes as high as about 2500 V.

All the HDL-built V-monitor calibration data are plotted in figure 7. They have all been normalized to  $d = 3.18$  cm,  $D = 25.4$  cm,  $R_x = 485$  ohms, and  $C_2 = 2000$  pF. The closed circles were derived from the data of Sazama and Stewart, as was already explained. The X's are derived from additional measurements with the old fixture (fig. 4). For

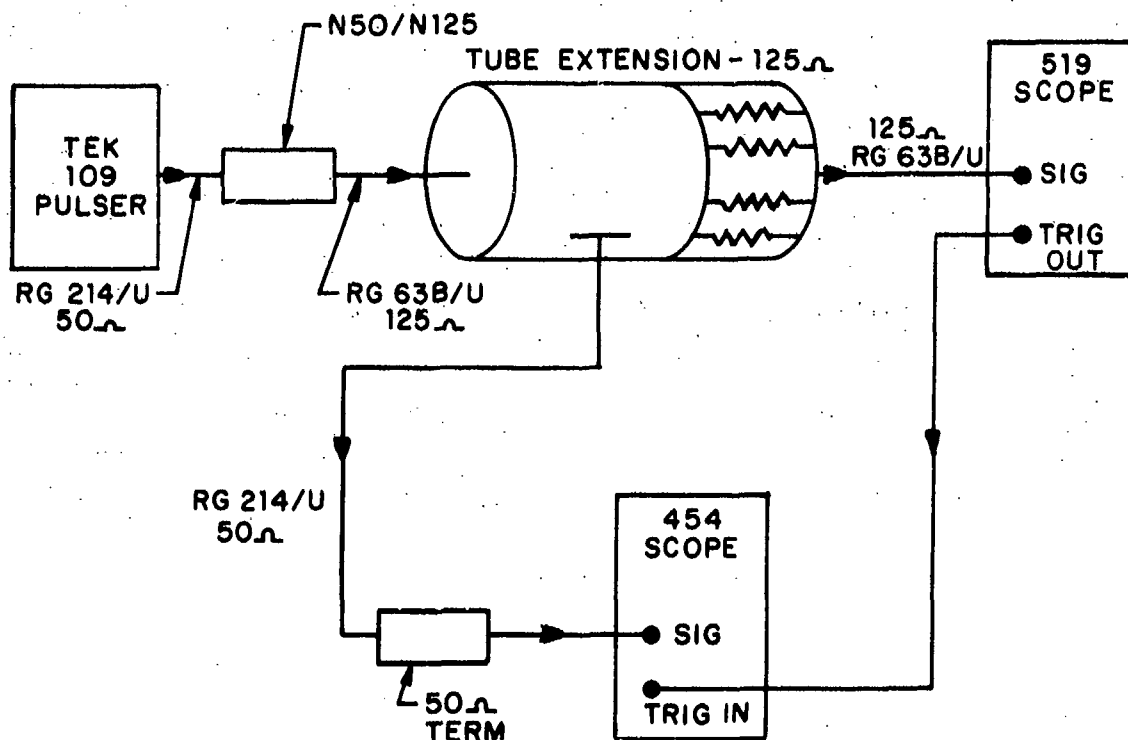


Figure 8. Schematic for calibration of HDL-built monitors with matched 125-ohm system.

these measurements, however, a threaded rod and nut, rather than a cylindrical carbon resistor, were used to make contact with the 222-ohm terminating disc resistor. Normalization for these data was performed using the ratio  $C_1/\bar{C}_1 = 2.15$  just as for the closed circles. The open circles are the results of measurements using the new fixture with the 3.18-cm diameter.

The line labeled "weighted average" in figure 7 was obtained as follows. A weight of 1 was arbitrarily assigned to the 3.18-cm diam data (open circles), since they required only one  $K_V$  measurement,  $K_V(3.18 \text{ cm})$ . A weight of  $1/3\frac{1}{2} = 0.577$  was assigned to the 0.64-cm data (closed circles and X's) since these depended on three independent  $K_V$  measurements: one for  $K_V(0.64 \text{ cm})$  measured in the old fixture, and

two for the empirically determined ratio of 2.15 for  $K_V(3.18 \text{ cm})/K_V(0.64 \text{ cm})$ , measured in the new fixture. The resulting weighted average is

$$K_{V,HDL}^{\text{meas}}(3.18 \text{ cm}) = 10.41 \text{ V/MV} , \quad (9)$$

with weighted average deviation of

$$\overline{\Delta_V} = \pm 0.90 \text{ V/MV} . \quad (10)$$

The theoretical value,

$$K_{V,HDL}^{\text{theory}}(3.18 \text{ cm}) = 9.85 \text{ V/MV} , \quad (11)$$

is derived in appendix A. It is represented in figure 7 by the line labeled "theory." The 0.55 V/MV disagreement with the weighted average of the measured values, 10.41 V/MV, is within the  $\pm 0.90 \text{ V/MV}$  uncertainty of these measurements.

### 2.3 SPI-Built V-Monitor Pulse Calibrations

The V monitor built by SPI is an integral part of the FE tube extension and "pumping tee." Figure 9 displays the V monitor, showing the pumping line and the output GR connector. Figure 10 shows a 2.54-cm wide steel band wrapped around the inside wall of the FE tube extension as well as the buckle by which tension is applied to the band. A 2.54-cm wide strip of 0.05-mm mylar adhesive insulates the band from the FE tube wall, and acts as the dielectric for  $C_2$ . Thus, the SPI-built V monitor employs a purely coaxial geometry rather than the curved-plate geometry of the HDL-built V monitor.

The calibration fixture for the SPI monitors is illustrated in figure 11. In contrast to the 125-ohm system used for the HDL-built monitors (fig. 5), a 50-ohm system, employing conical inner and outer



Figure 9. SPI-built V monitor and pump tee mounted on HIFX machine, showing V-monitor GR connector.

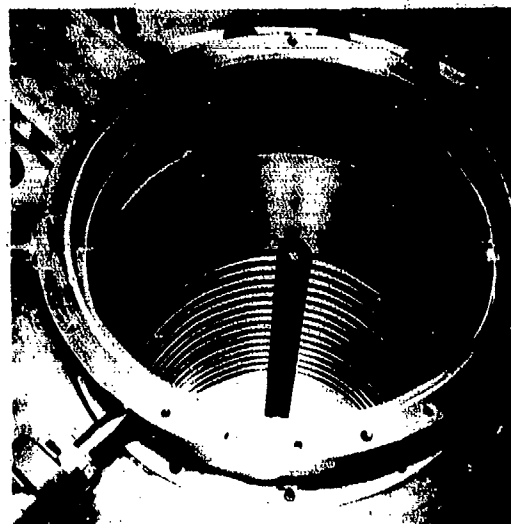


Figure 10. SPI-built V monitor showing capacitor band and buckle.

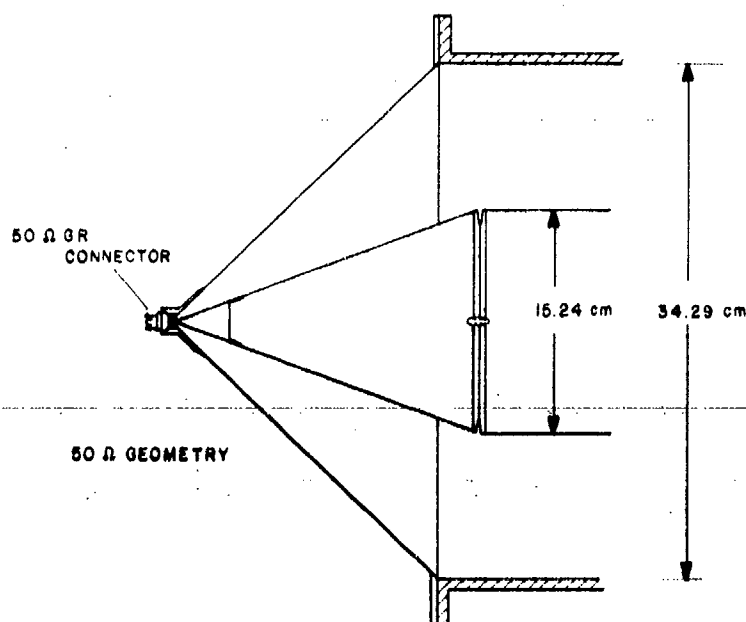


Figure 11. Transmission line cones for bench test of SPI-built monitors.

conductors at each end, is used for the SPI monitors. The cones form a smooth transition from a 50-ohm GR connector to a 50-ohm coaxial section formed by a 34.29-cm outer conductor and a 15.24-cm inner conductor. The latter geometry corresponds exactly to that of the HIFX low-impedance mode.

Figure 12 illustrates the setup for

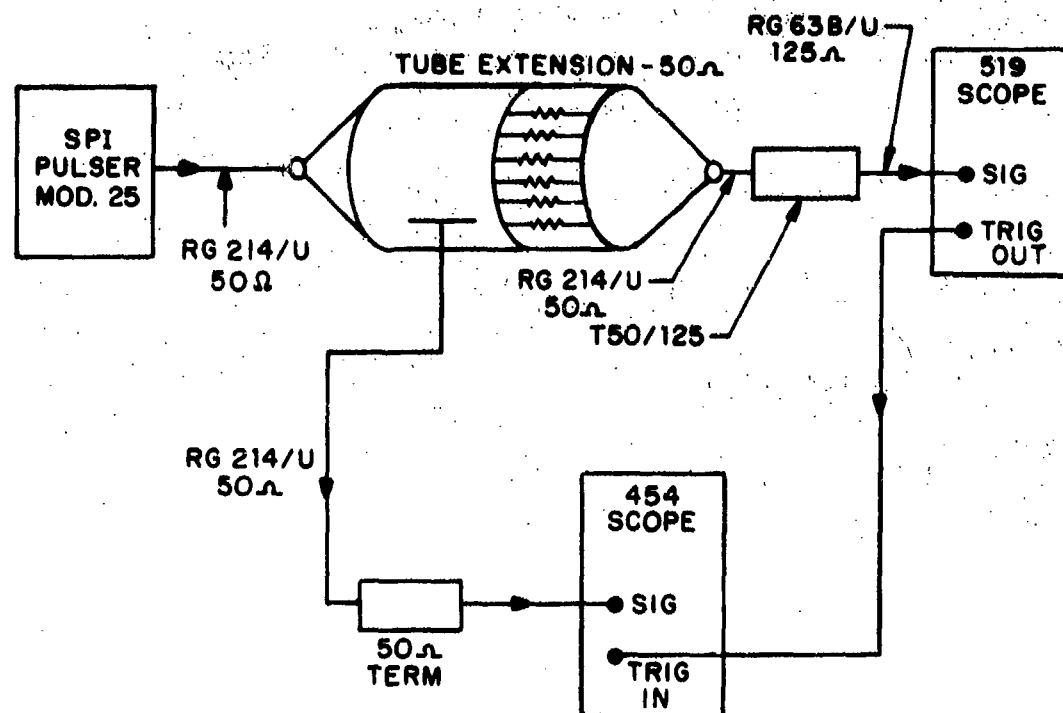


Figure 12. Schematic for bench-test calibration of SPI-built V and I monitors.

obtaining calibration pulses. For these measurements the input pulse amplitude was limited to <1000 V to avoid electrical breakdown in the 50-ohm connectors and the T50/N125 fixture. Figure 13 shows sample input and output pulses.

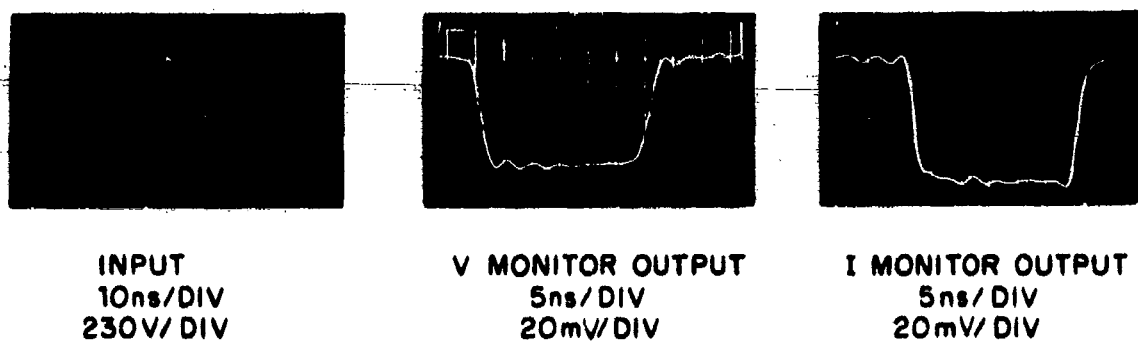


Figure 13. Input and output pulses in SPI-built monitor bench-test calibration.



An in-place calibration method was also used for the V monitor, shown in figure 14. Since the in-place calibration is performed without removing the V-monitor/pumping-tee combination from the machine, it is a more convenient method than the bench-test method just described. The pulse is input to the coaxial cable at the cathode. It then travels to the rear of the tube extension; there, it is reflected nearly 100 percent, since the termination is essentially infinite. It then travels back to the source, where it suffers no further reflections, since the source is terminated in the characteristic 50 ohms. In practice, some reflections lasting for about the first 20 ns of the

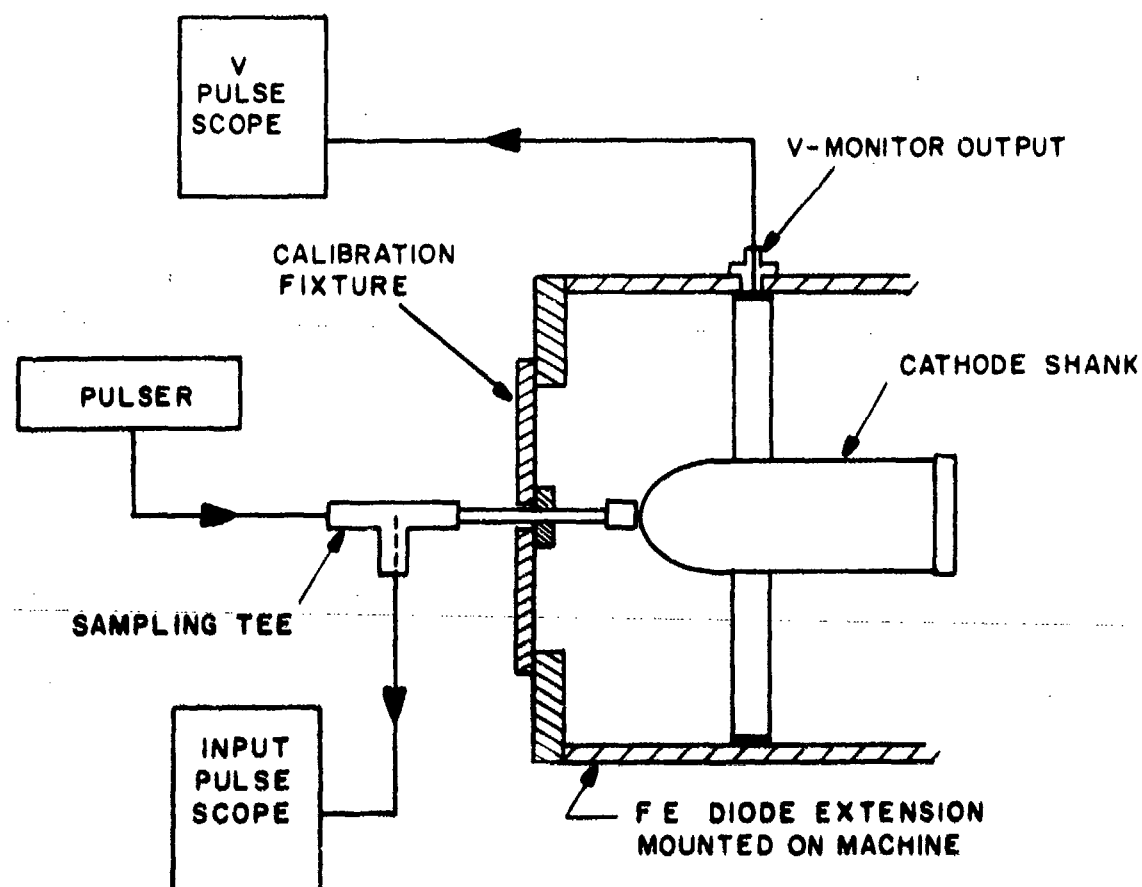


Figure 14. In-place method for SPI-built V-monitor calibration.

pulse do occur, because of imperfect termination, especially in the sampling tee. To exclude pulse-height measurements during these reflections, about 150 m of 50-ohm cable were used for the pulser charge line to greatly lengthen the pulse.

Sample input and output pulses using the in-place method are shown in figure 15. The output pulse, which decays exponentially (app A, eq (A-1)), was plotted on semilog paper, and the value of  $V$  extrapolated to zero time was used to find  $K_V$ .  $K_V$  was measured on three occasions using the in-place method and normalized by means of equation (1) with  $C_2 = 3775$  pF and  $R_x = 97.6$  ohms. The resulting values of  $K_V$  were 190, 194, and 199 V/MV. Their average is

$$K_{V,SPI}^{meas} (15.24 \text{ cm}) = 194 \pm 3 \text{ V/MV} . \quad (12)$$

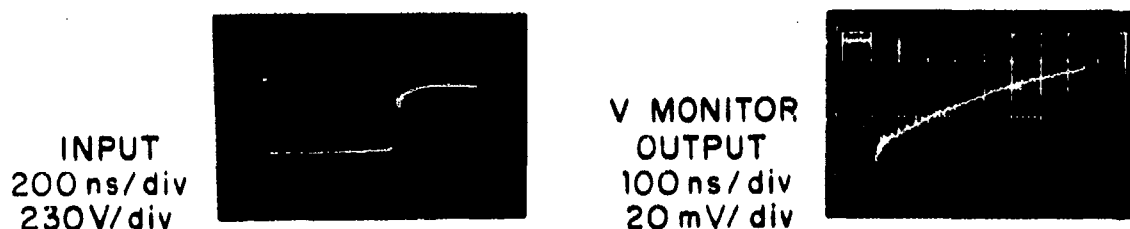


Figure 15. Input and output pulses in SPI-built V-monitor in-place calibration.

Since the shank and steel band may be looked upon as forming a coaxial section, equation (3) should be valid for calculating  $C_1$ . This equation yields

$$C_{1,SPI}^{theory} (15.24 \text{ cm}) = \frac{55.54}{\ln \frac{34.29}{15.24}} \times 0.0254 = 1.740 \text{ pF} . \quad (13)$$

The sensitivity of the V monitor is\*

$$K_V = \frac{V_{out}}{V_{in}} = \left( \frac{C_1}{C_1 + C_2} \right) \left( \frac{R_{term}}{R_{term} + R_x} \right) V/V . \quad (14)$$

where

$V_{out}$  = output voltage,

$V_{in}$  = input voltage, and

$R_{term}$  = 50-ohm termination of the signal cable.

Then, using equation (14),

$$K_{V,SPI}^{theory} (15.24 \text{ cm}) = \frac{1.740}{1.767 + 3775} \times \frac{50}{50 + 97.6} = 156 \text{ V/MV} . \quad (15)$$

Thus, whereas  $K_{V,HDL}^{meas}$  is only 6 percent higher than  $K_{V,HDL}^{theory}$ --equations (9) and (11)-- $K_{V,SPI}^{meas}$  is 25 percent higher than  $K_{V,SPI}^{theory}$ --equations (12) and (15). This result is somewhat surprising since the geometry of the HDL-built V monitor is not a simple coaxial one, and the estimate for  $C_{1,HDL}$  in appendix A should therefore not be as accurate as the above estimate for  $C_{1,SPI}$ . It may be that there are large contributions to  $C_{1,SPI}$  from stray capacitance which are proportionately less than such contributions to  $C_{1,HDL}$ .

The use of long pulses in the in-place calibrations also yields a measure of the RC decay constant. The average of the two measurements was

$$RC_{SPI}^{meas} (15.24 \text{ cm}) = 551.5 \text{ ns} \quad (16)$$

\*See appendix A for derivation of equation (14)--(A-4).

The decay time constant of the circuit ( $\tau$ ) is\*

$$\tau = (R_{\text{term}} + R_x)(C_1 + C_2). \quad (17)$$

The theoretical value, given by equation (17), is

$$RC_{\text{SPI}}^{\text{theory}} (15.24 \text{ cm}) = (97.6 + 50) (3775 + 1.767) \times 10^{-12} = 557.2 \text{ ns} \quad (18)$$

There is thus about a one-percent difference between measured and theoretical RC decay constants. This estimate for RC, in contrast to that of  $K_V$ , is, of course, hardly affected by any inaccuracy in  $C_1$ , as may be readily seen by comparing equations (17) and (14) and noting that  $C_1 \ll C_2$ .

#### 2.4 I-Monitor Pulse Calibrations

Both the HDL-built I monitor, shown in figures 1 and 2, and the SPI-built I monitor, shown in figure 16, consist of a small shunt resistance in the form of a band of resistors in parallel. (Details of construction are given in appendix A.) Whereas the HDL-built monitor is a permanent part of the FE tube extension, the SPI-built monitor is a unit in itself which may be mounted on either side of the anode plate or at the exit end of a drift chamber, when HIFX is operating in the electron mode.  $R_p$  for the HDL-built I monitor was made up of two inner layers of 167 20-ohm, 1-W carbon resistors, and an outer layer of 167 3.0-ohm, 1-W carbon resistors, resulting in a combined resistance of 5.59 milliohms.  $R_p$  for the SPI-built monitor consists of a single layer of 306 3.3-ohm, 0.5-W carbon resistors, resulting in a resistance of 10.78 milliohms.

---

\*See appendix A for derivation of equation (17)--(A-2).



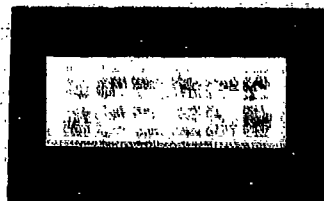
Figure 16. SPI-built I monitor.

Pulse calibration of the HDL-built I monitor was performed with both the 222-ohm fixture of figure 4 and the matched 125-ohm fixture of figure 5. Sample pulses with each of these fixtures are shown in figure 17. Whereas the output pulses with the former were always square like the input pulse, those with the latter seemed to decay exponentially to some equilibrium value, i.e., they could be approximated by

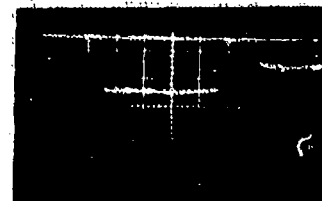
$$V(t) = A + Be^{-t/\tau} \quad (19)$$

with  $\tau \approx 90$  ns. No apparent cause could be found for this behavior. Such a 90-ns characteristic decay would have affected the current monitor pulses from HIFX if the cause were in the monitor itself. However, no such effect was ever observed. The cause was therefore probably in the calibration fixture, although no investigation sufficiently extensive to prove this was undertaken. In all cases of pulses from this fixture the steady state value  $A$  was used as the output voltage for calculating  $K_I$ . The data for all the HDL-built I monitor

INPUT  
50 ns/div  
930 V/div

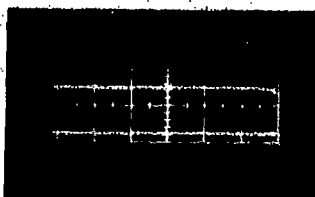


I MONITOR  
OUTPUT  
50 ns/div  
20 mV/div

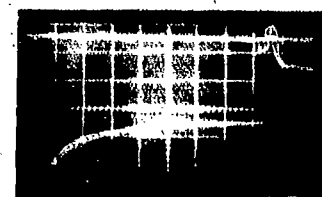


### 222 OHM CALIBRATION FIXTURE

INPUT  
100 ns/div  
912 V/div



I MONITOR  
OUTPUT  
100 ns/div  
20 mV/div



### 125-OHM "MATCHED" SYSTEM

Figure 17. HDL-built I-monitor calibration pulses.

pulse calibrations are shown in figure 18. The closed circles, open circles, and X's have the same meanings as in figure 7, and all data have been normalized to a value  $R_p = 5.73$  milliohms through equation (2). The overall average is

$$K_{I,HDL}^{meas} = 6.36 \text{ V/kA} , \quad (20)$$

whereas the theoretical value is, of course,

$$K_{I,HDL}^{theory} = 5.73 \text{ V/kA} . \quad (21)$$

The 10-percent difference is not unreasonable, considering the five percent or so uncertainty in each of the pulse-height measurements.

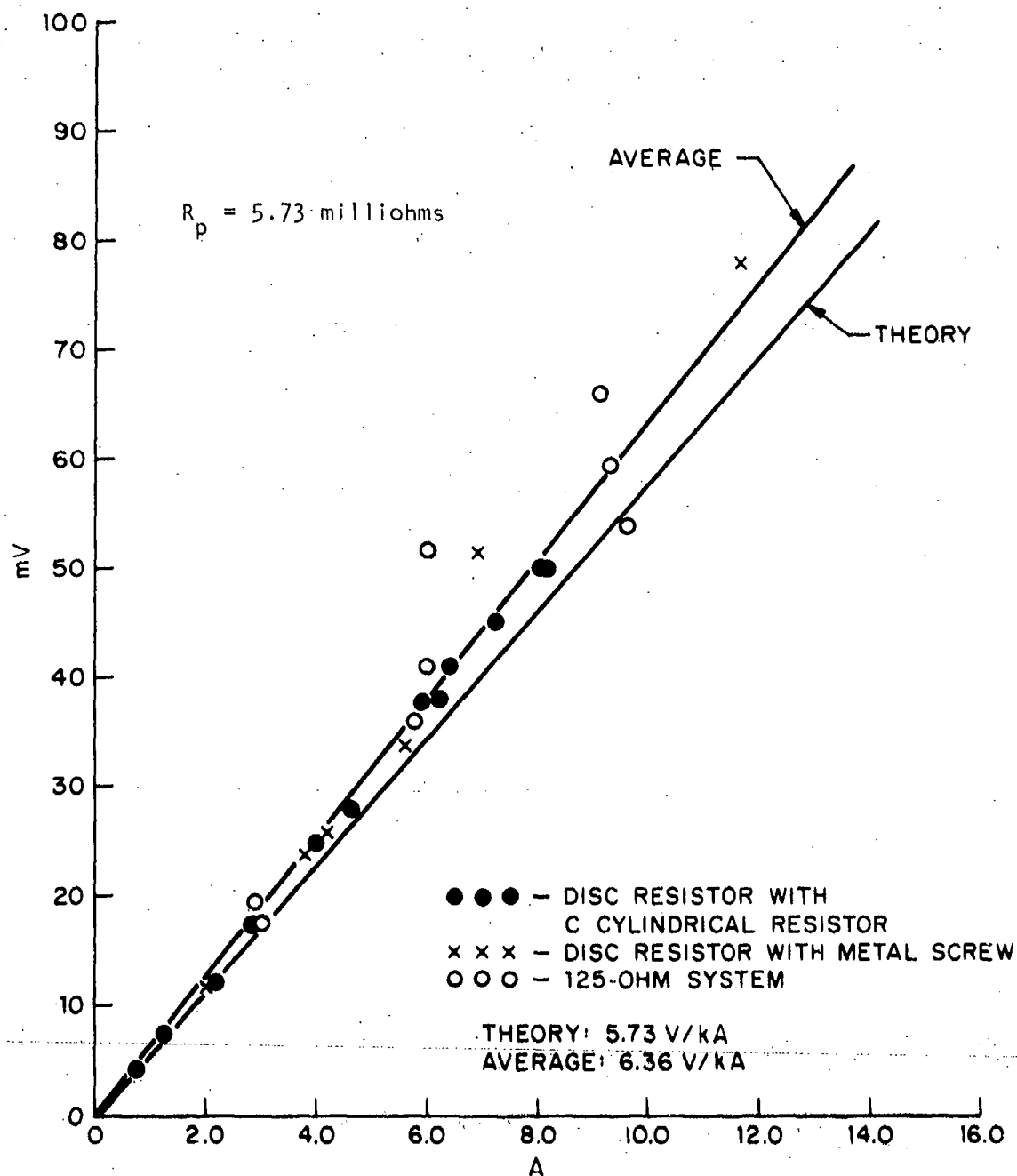


Figure 18. HDL-built I-monitor calibration data.

Pulse calibrations for the SPI-built I monitor were performed with the calibration fixture and setup shown respectively in figures 11

and 12. The in-place method used for the SPI V monitor, shown in figure 14, is not applicable to the I monitor since the coaxial termination is infinite, yielding essentially zero current. The results for  $K_I$  from three bench-test measurements, normalized to  $R_p = 10.63$  milliohms by equation (2) are 11.59, 11.2, and 11.07 V/kA, yielding an average

$$K_{I, SPI}^{meas} = (11.36 \pm .19) \text{ V/kA} . \quad (22)$$

The theoretical value is

$$K_{I, SPI}^{theory} = 10.63 \text{ V/kA} , \quad (23)$$

which agrees with the measured value to within 10 percent.

## 2.5 Circuit Parameter Values

Table 1 shows the values at various times of  $R_x$ ,  $C_2$ , and  $R_p$  for the HDL monitors.  $R_x$  was measured with a Rubicon Wheatstone bridge,  $C_2$  with a GR capacitance bridge, and  $R_p$  with a Leeds and Northrop Kelvin bridge. Also shown are the cumulative number of HIFX pulses to which the monitors were subjected at the time of the measurements and the resultant values of  $K_V$  and  $K_I$  calculated by means of equations (1) and (2), respectively.

Variations in  $R_x$  and  $C_2$  were generally less than two percent. On 7/28/71, a 1000-ohm carbon-film resistor was substituted for the 500-ohm carbon-composition resistor to observe the effect of a larger RC on the voltage pulse. No effect was observed. The unusually small values of  $C_2$  on 7/22/71, 7/28/71 and 8/2/71 were due to specks of dirt that became imbedded in the mylar dielectric film.



TABLE 1. CIRCUIT PARAMETER BRIDGE MEASUREMENTS FOR HDL-BUILT MONITORS

$$K_V = 10.41 \left( \frac{2000}{C_2} \right) \left( \frac{985 + 50}{R_x + 50} \right) \text{V/MV (shank diam} = 3.18 \text{ cm)} \quad K_I = 6.5 \left( \frac{R_p}{5.75} \right) \text{V/kA}$$

Date	Accumulated pulses	$R_x$ (ohms)	$C_2$ (pF)	$R_p$ (mohm)	$K_V$ (V/MV)	$K_I$ (V/kA)	Comments
4/28/70	0			5.650		6.4	
4/28/70	69			5.675		6.4	
5/6/70	69			5.678		6.4	
5/21/70	69			5.705		6.5	
6/8/70	69	486.6	1990	5.730	10.41	6.5	Uncertain of date for $C_2$ and $R_x$ measurements
	88			5.710		6.5	
6/9/70	88			5.710		6.5	
	106			5.745		6.5	
6/12/70	119			5.770		6.5	
7/3/70	119			5.780		6.6	
	144			5.805		6.6	
7/10/70	144			5.823		6.6	
	168			5.845		6.6	
7/21/70	168			5.865		6.7	
7/22/70	185			5.880		6.7	
7/23/70	202			5.840		6.6	
6/18/71	202	518.5		5.900		6.7	
7/24/71	257	529.9		5.883		6.7	
7/21/71	257	528.2		5.935		6.7	
	257	617.3		5.935		6.7	$R_x$ carbon resistor broke
7/22/71	257		1550				
7/28/71	257	998.8	1515	5.460	6.58	6.8	Put in 1000-ohm carbon film resistor for $R_x$
8/2/71	309	996.8	1500		7.09		Found specks in Mylar for $C_2$
	309		1965				New 2-mil Mylar for $C_2$
8/6/71	316	482.0		5.940		6.7	Inserted new C composition resistor for $R_x$
8/24/71	370	478.4	2025	5.960	10.41	6.7	
11/9/71	375	480.5	2000	5.975	10.50	6.8	New Lucite ring in 1 monitor
11/16/71	418	480.4	2000	5.965	10.50	6.8	
12/9/71	464	478.0		6.415		7.3	Made 23 shots with shorted tube 12/7/71
1/17/72	464	478.0	2010	6.375	10.55	7.2	
3/7/72	464	475.4		6.300		7.1	
12/26/72	659	478.2	2129	6.575	10.55	7.5	

$R_p$  generally increased fairly steadily with the number of accumulated pulses, except on 12/9/71, when an abrupt increase occurred. As indicated in the table, this measurement was made shortly after 23 HIFX pulses in the "shorted" mode were made. In this mode the cathode shank is shorted to the anode plate resulting in significantly higher currents (see sect 3.4).

Table II gives the bridge-measured values of the SPI-built monitors' circuit parameters and the resultant  $K_V$  and  $K_I$  calculated according to equations (1) and (2), respectively. The I monitor was almost always removed during operation in the bremsstrahlung mode to avoid radiation damage to its dielectric spacer. It therefore accumulates pulses at a slower rate than the V monitor.

TABLE II. CIRCUIT PARAMETER BRIDGE MEASUREMENTS FOR SPI-BUILT MONITORS

$$K_V = 194 \left( \frac{3775}{C_2} \right) \left( \frac{97.6 + 50}{R_x + 50} \right) \text{V/MV (shank diam} = 15.24 \text{ cm)} \quad K_I = 11.4 \left( \frac{R_p}{10.63} \right) \text{V/kA}$$

Date	V-monitor accumulated pulses	$C_2$ (pF)	$R_x$	$K_V$ (V/MV)	I-monitor accumulated pulses	$R_p$ (ohm)	$K_I$ (V/kA)	Comments
5/14/73	52	3775	97.6	194	52	10.63	11.4	
6/1/73	111	3200	109.1	212	111	10.63	11.4	Capacitor band retensioned
1/23/74	0	3390	103.2	208	117	11.64	12.5	Installed new Mylar ( $C_2$ ) and resistor ( $R_x$ )
1/28/74	25	3390	101.2	211	142	11.06	11.9	Made 16 shots in shorted mode before measurements
2/25/74	426	3390	103.3	208	142	11.48	12.3	
2/27/74	457	3390	103.8	207	173	10.91	11.7	Made 3 shots in shorted mode on 2/26/74
3/22/74	769		103.1		173	10.76	11.5	
4/3/74	843	3910	102.8	181	247	11.19	12.0	$K_I$ measured through $R_x$ and in vacuum
6/24/74	2374	3950	102.3	180	247	11.19	12.0	
7/15/74	2654	3970	102.1	179	524	11.06	11.9	
8/20/74	2928	4000	101.0	179				
11/15/74	4565	4020	99.7	180	524	12.58	13.5	

The value of  $C_2$  is sensitive to the tension applied to the steel band. This sensitivity probably explains the great difference between  $C_2$  on 5/14/73 and on 6/1/73, since the band was removed in the interim and upon reinstallation was doubtless retensioned to a new value. On 4/3/74,  $C_2$  was not measured in the usual way, i.e., in air and directly across  $C_2$ . It was instead measured from the center pin of the GR connector to ground, i.e., through  $R_x$ , with the FE tube under vacuum. Despite this difference in method of measurement, the value of  $C_2$  obtained on 4/3/74 agrees to within 3 percent with those obtained in the next four measurements, which were performed in the usual way. There is, however, no apparent explanation for the sudden change in  $C_2$  between 2/27/74 and 4/3/74.

Abrupt increases in  $R_p$  were observed on 1/23/74 and 11/15/74. Since no pulses in the "shorted" mode were made just before these measurements, the suggestion that unusually high currents may have caused the abrupt increases is not applicable here, as it is in the case of  $R_p$  for the HDL-built I monitors. In fact,  $R_p$  for the SPI-built I monitor was actually observed to decrease by about 5 percent after pulses in the shorted mode, which were made just before the measurements on 1/28/74 and 2/25/74.

### 3. MONITOR PULSES FROM HIFX

#### 3.1 Diode Geometries and Monitors

The diode geometry used for the high-impedance mode measurements is shown in figure 3. The cathode consists of a long 3.18-cm diam stainless steel shank having a hemispherical tip. The gap,  $G$ , separating the cathode tip from the anode plane was set at values between 1.5 and 5.6 cm by means of 3.18-cm diam spacers which could be

added to or removed from the shank. The anode shown in figure 3, which is used in the bremsstrahlung mode, consists of a 0.038-cm thick by 11.43-cm diam tantalum disc mounted on a 0.95-cm thick aluminum plate. The tantalum disc acts as the bremsstrahlung converter. The aluminum plate forms a closure to the evacuated tube and absorbs any electrons that penetrate the tantalum. The anode assembly used for the electron mode consists of a 0.005-cm thick by 8.26-cm diam titanium foil mounted on an aluminum holder. This foil is thin enough to allow the electrons emitted from the cathode to penetrate it with almost no energy degradation. Figure 3 also shows the HDL-built V and I monitors permanently mounted to the tube extension.

The diode geometry used for the low-impedance mode measurements is shown in figure 19. The cathode consists of a 15.24-cm diam shank on whose end is mounted a graphite emitter having a diced surface to enhance emission. Emitters with various diameters between 1.27 and 5.08 cm were used, and G could be continuously varied between 0.4 and 1.4 cm by adjusting the protrusion of the emitter from the shank. The anode consisted of either a 0.0064-mm mylar film having a thin coating of aluminum or a 0.0064-mm titanium foil. As in the case of the high-impedance electron mode anodes, these anodes are designed to allow penetration of the electrons with very little energy degradation. Bremsstrahlung production in this mode is not practical because of the very low doses that would result.

In the low-impedance mode V and I were measured with the SPI-built monitors (see fig. 19). In this case the tube extension consists of the integral V monitor and pumping tee, the I-monitor assembly, and an anode assembly. The construction of these monitors is such that both the V and I monitors are adjacent to the cathode-anode region. This is not the case for the HDL-built V monitor (fig. 3).

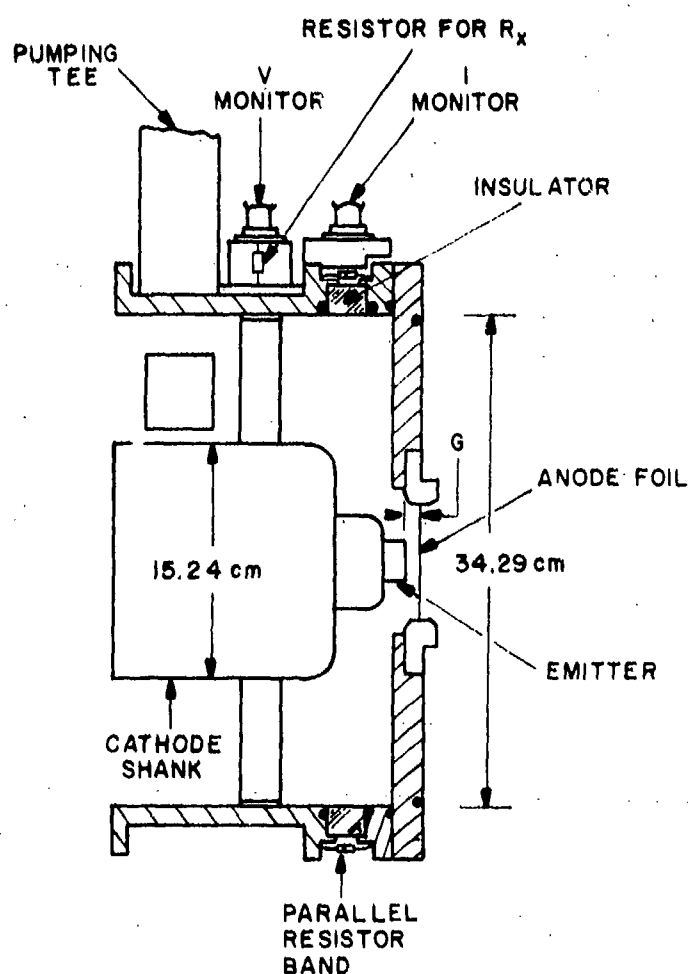


Figure 19. Low-impedance diode geometry.

When operating in the high-impedance bremsstrahlung mode, simultaneous measurements were often also made of the bremsstrahlung dose rate,  $R$ , and integrated dose on axis. These were compared with predictions of these quantities based on the  $V$  and  $I$  pulses (see sect 4.6). Comparisons of  $R$  pulses obtained with a pilot-B scintillator/ITT FW114 photodiode combination and those obtained with a Compton diode revealed that both had comparable decay times, in contrast to the results cited by Sazama and Stewart.<sup>1</sup> The former detector was chosen as

the standard  $R$  monitor at HIFX because of its much greater sensitivity. The integrated doses were measured with  $\text{CaF}_2\text{:Mn}$  TLD's.

<sup>1</sup>F. J. Sazama and A. G. Stewart, *Design and Testing of a Current and Voltage Monitor for HIFX*, Harry Diamond Laboratories TR-1558 (August 1971).

### 3.2 High-Impedance Pulses

Figures 20 through 24 show Tektronix 519 oscilloscope traces obtained from the HDL-built V and I monitors and R detector with HIFX operating in the high-impedance gamma mode.\* Each figure displays three sets of pulses obtained at Van de Graaff charge voltages,  $V_c$ , of 3.0, 4.0, and 5.0 MV. All the V and I pulses in these figures have similar shapes: about a 5-ns rise to a primary maximum followed by a descent

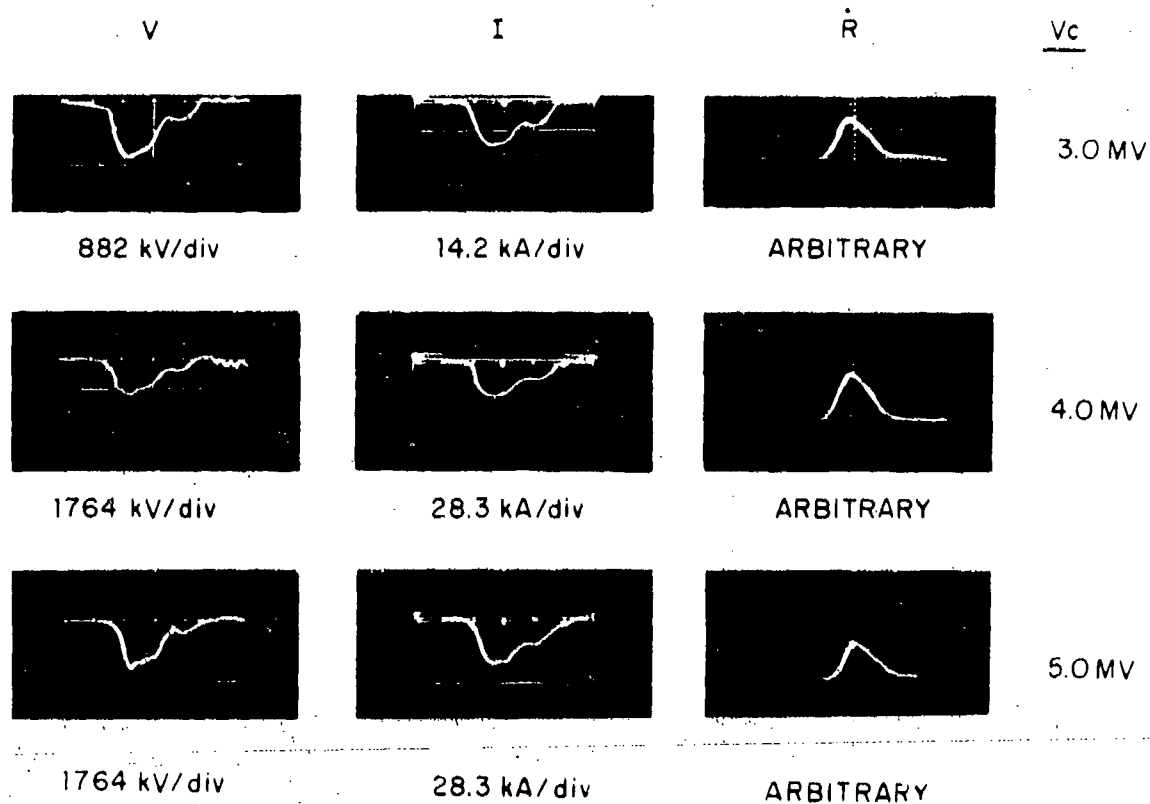


Figure 20. V, I, and R traces from  $G = 1.5$  cm hemi-plane diode; X scale: 20 ns/div.

\*Many of the V and I pulses described in this and following sections were obtained by C. G. Casaer, O. B. Benton, and K. J. Allen.

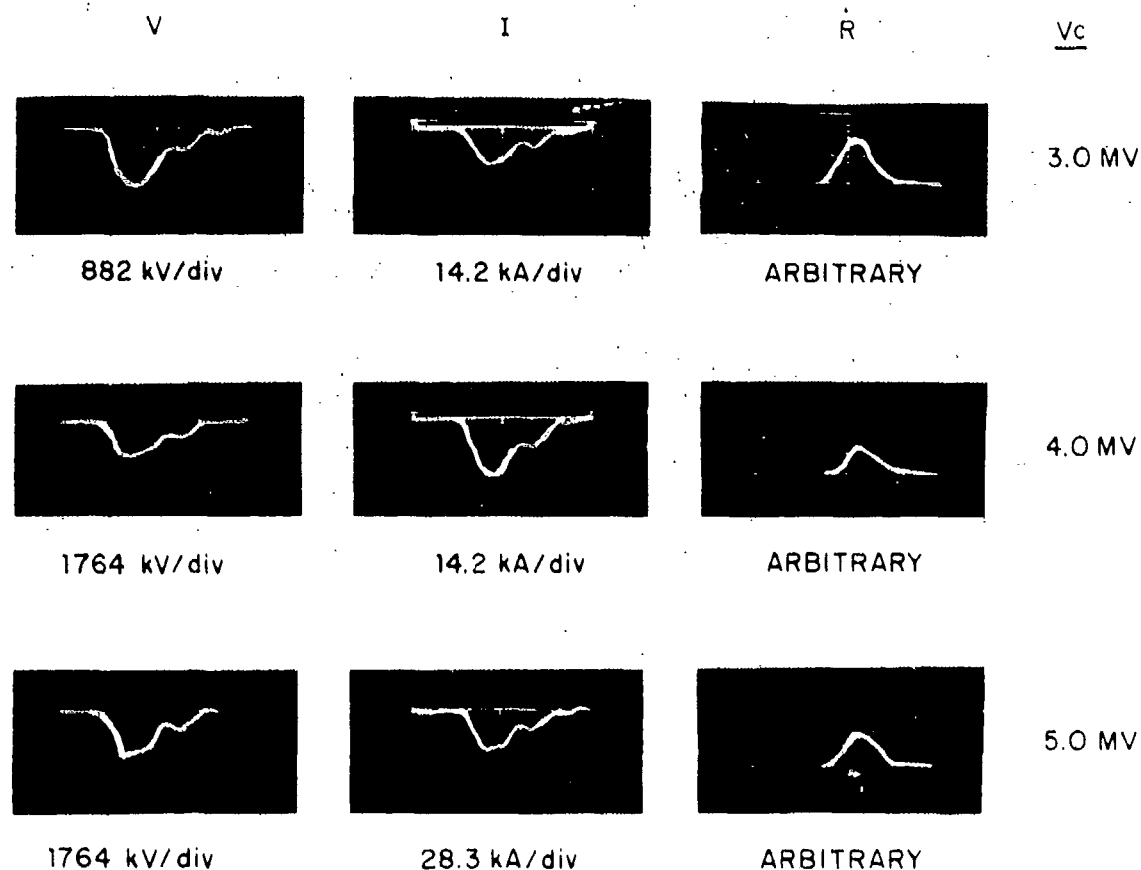


Figure 21. V, I, and R traces from G = 2.1 cm hemi-plane diode; X scale: 20 ns/div.

toward the baseline, with one or sometimes two discernible secondary maxima. The maxima are separated by about 25 ns. A notable exception to the general character of the pulses is seen in the V pulses of figure 24 at  $V_c = 4.0$  and 5.0 MV. These V pulses do not return to the baseline within the 120-ns sweep time as do the others. This late-time behavior of the V-monitor output was found to occur at random and to have durations in the microsecond range. It was sometimes necessary to make a number of machine pulses with the same diode geometry before a "clean" V pulse could be obtained. This phenomenon, which was investigated extensively, is discussed more fully in appendix C.

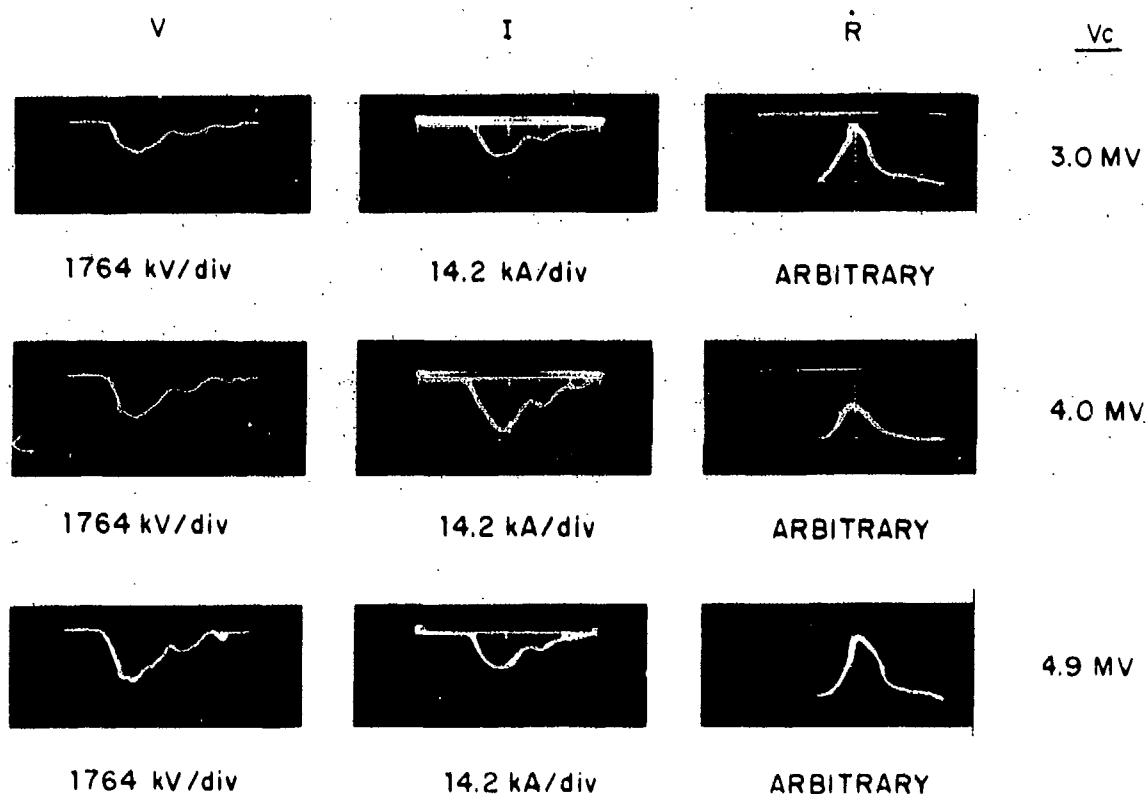


Figure 22. V, I, and  $\dot{R}$  traces from G = 2.8 cm hemi-plane diode; X scale: 20 ns/div.

Sazama and Stewart<sup>1</sup> showed that the V and I pulse shapes can be qualitatively explained in terms of a charged-line model for HIFX. The concentric terminal and pressure tank form a coaxial transmission line having a 59-ohm characteristic impedance and presenting a round-trip travel time of 25 ns to an electromagnetic pulse. This line is charged by high-impedance voltage source representing the Van de Graaff generator, and, upon closing a switch, discharges into a load representing the FE tube and the cathode-anode gap. In the simplest form of this model, the load is purely resistive and the impedance is

<sup>1</sup>F. J. Sazama and A. G. Stewart, *Design and Testing of a Current and Voltage Monitor for HIFX*, Harry Diamond Laboratories TR-1558 (August 1971).



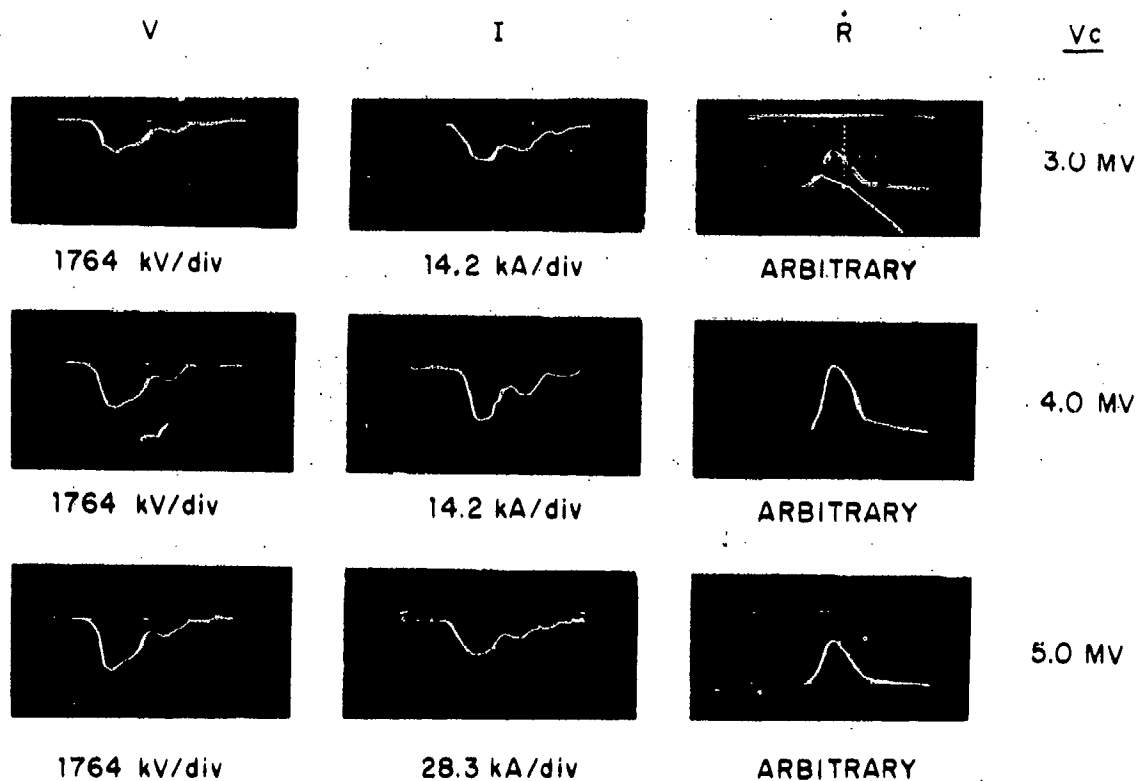


Figure 23. V, I, and  $\dot{R}$  traces from  $G = 3.8$  cm hemi-plane diode;  $\lambda$  scale: 20 ns/div.

simply  $V_{\max}/I_{\max}$  measured at one of the V- and I-pulse maxima (see sect 4.3 and 4.4 for more discussion of diode impedance).

The shapes of the  $\dot{R}$  pulses in figures 20 through 24 can be explained on the basis of a semiempirical formula<sup>1</sup> relating the time dependance of  $\dot{R}$  to that of V and I. This formula does not, however, predict the integrated dose correctly. Both  $\dot{R}$ -pulse shapes and integrated dose will be discussed fully in section 4.6.

<sup>1</sup>F. J. Sazama and A. G. Stewart, Design and Testing of a Current and Voltage Monitor for HIFX, Harry Diamond Laboratories TR-1558 (August 1971).

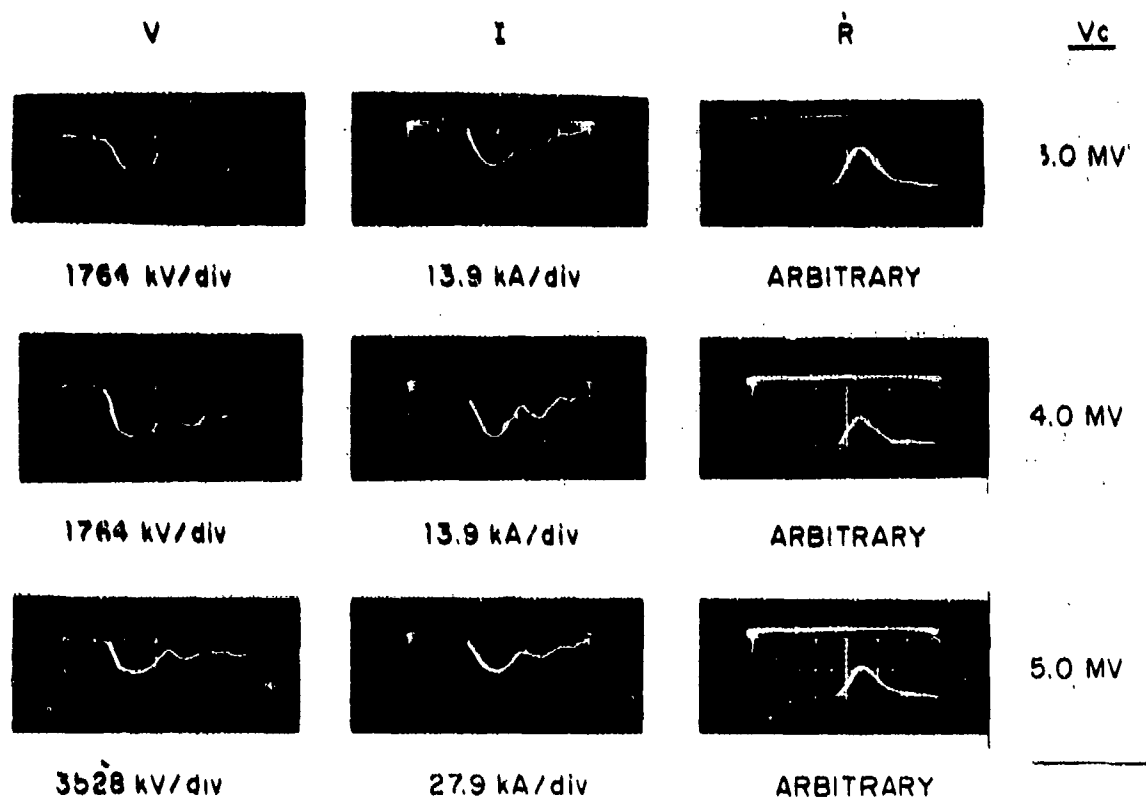


Figure 24. V, I, and R traces from G = 5.8 cm hemi-plane diode; X scale: 20 ns/div.

To use the monitor pulses to calculate diode impedance, electron spectra, energy delivered to load, and dose rate expected, we must record the pulses in proper time synchronization. Appendix B discusses the three different methods employed on different occasions to accomplish this synchronization. The pulses in figures 20 through 24 were obtained using synchronization method 1, since at the time these pulses were made we had not yet discovered that this method sometimes yielded asynchronizations of up to 7 ns (see fig. B-2). After we discovered this asynchronization and experimented with the other two synchronization methods, we obtained more high-impedance pulses using synchronization method 3. Shot-to-shot reproducibility using this method was demonstrated to be as good as 1 ns (see app B).

High-impedance pulses obtained with synchronization method 3 are shown in figures 25 and 26 (pp. 42, 43). They are plotted on a common set of axes to simplify comparisons of their occurrence in real time and of their pulse shapes. The lower set of traces in figure 25 are the pulses recorded in each of the three scopes during a pulse timing check (see app B for discussion of the setup). The time bases are seen to be excellently synchronized. The remaining traces in these figures show pulses from the individual monitors in their observed time relationship. They were obtained at a cathode-anode gap of 2.6 cm and at Van de Graaff charge voltages of 3.0, 3.5, 4.0, 4.5, and 5.0 MV. In each of these the rising portion and maximum of the I pulse occur 5 to 10 ns later than those of the V pulse. As shown in section 3.4, much of the lag of I behind V is eliminated when induction corrections are applied to the V pulse.

Another feature common to the traces in figures 25 and 26 is the great delay between the primary maximum of either V or I and that of R. A similar delay between electron-beam current and bremsstrahlung-pulse leading edges has been observed in other investigations<sup>2</sup> with no apparent explanation.

### 3.3 Low-Impedance Pulses

Figures 27 and 28 show common-axis plots of V and I pulses obtained in the low-impedance mode at a charge voltage of 4.1 MV with a 5.08-cm diam diced graphite cathode. Pulse synchronization was achieved by method 3 (see app B). The lowest trace of figure 27 is a pair of timing check pulses obtained from the I monitor showing excellent time

<sup>2</sup>S. E. Graybill, J. R. Uglum, W. H. McNeill, J. E. Rizzo, R. Lowell, and G. Ames, *Diagnostics and Applications of Pulsed Self-Focussed Relativistic Electron Beams*, Defense Atomic Support Agency Report 24/7 (December 1969).

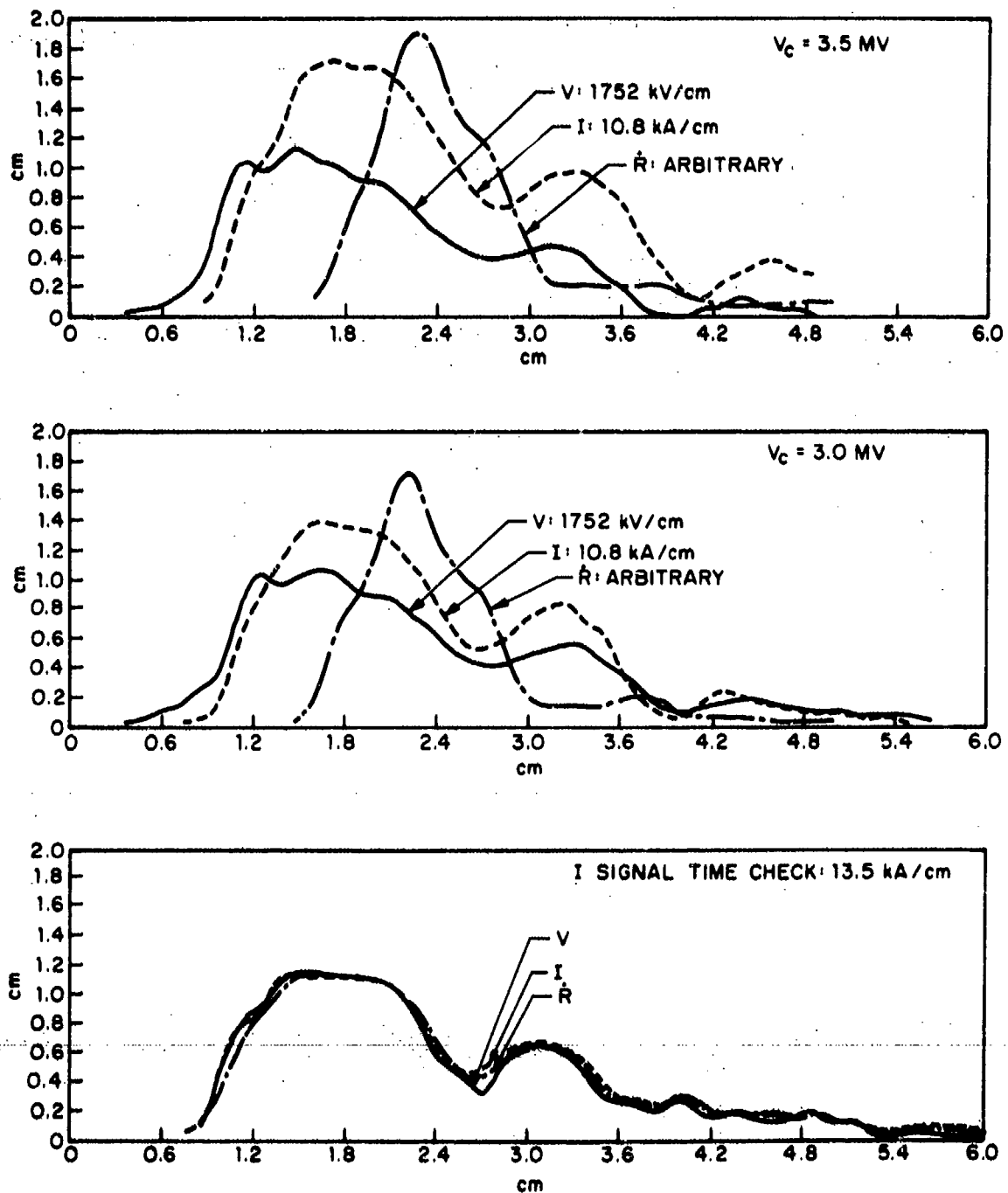


Figure 25. V, I, and R pulses from  $G = 2.6 \text{ cm}$ , hemi-plane diode synchronized by method 3; X scale: 20 ns/cm.

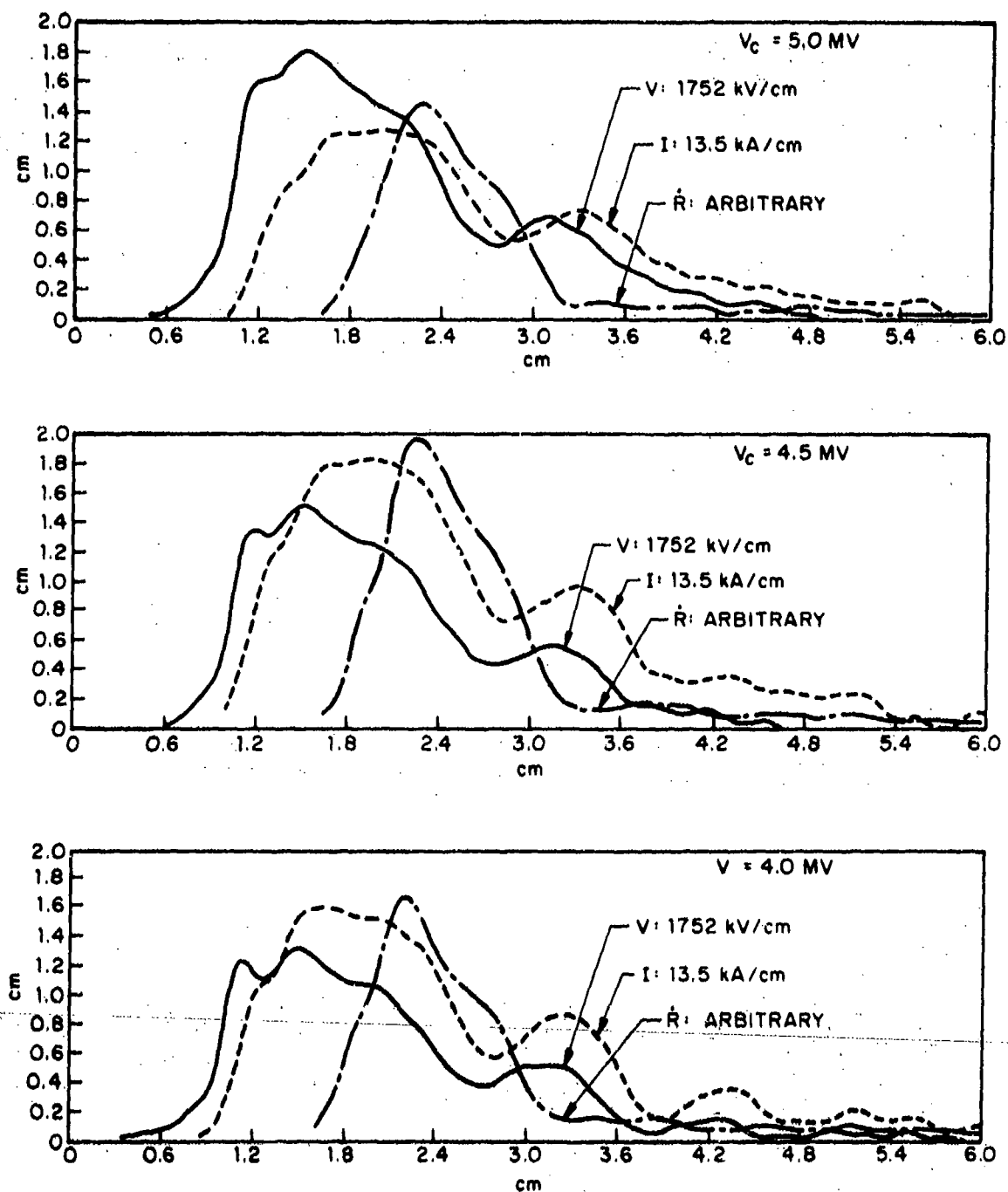


Figure 26.  $V$ ,  $I$ , and  $R$  pulses from  $G = 2.6$  cm, hemi-plane diode synchronized by method 3; X scale: 20 ns/cm.

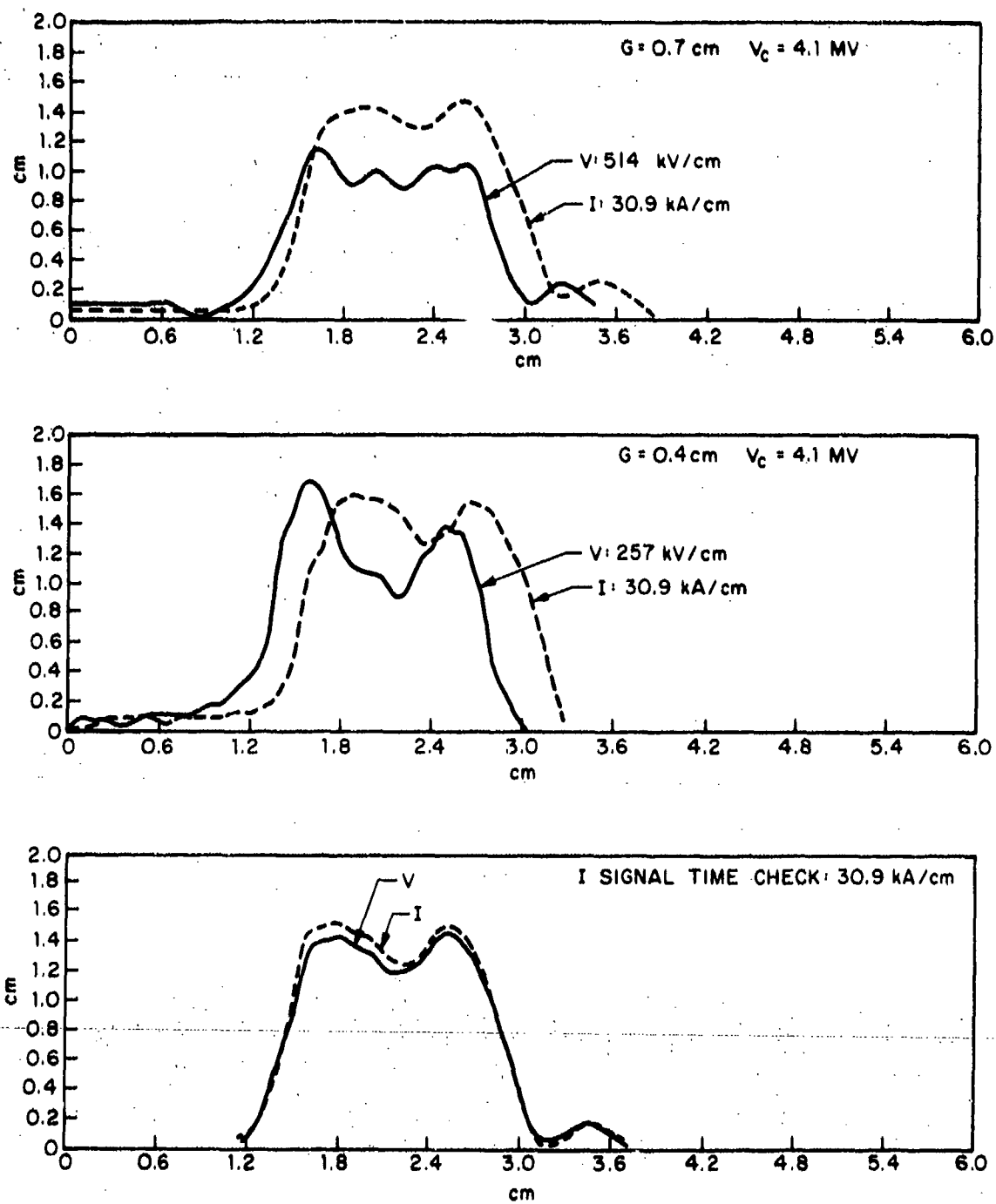


Figure 27. V and I pulses from low-impedance diodes synchronized by method 3; X scale: 20 ns/cm.

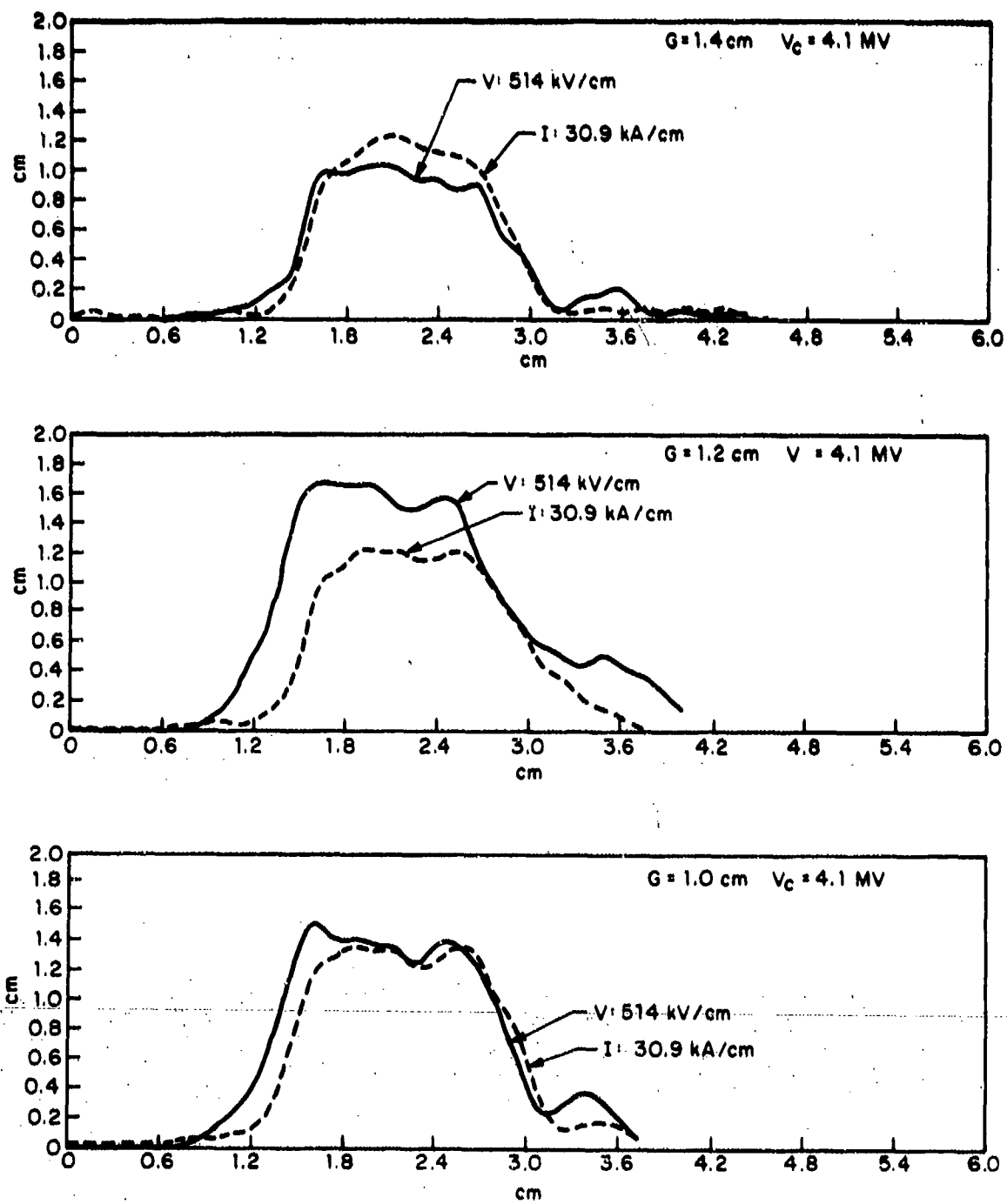


Figure 28. V and I pulses from low-impedance diodes synchronized by method 3; X scale: 20 ns/cm.

coincidence. The remaining traces are the V and I pulses in their observed time relationship obtained with cathode-anode gaps of 0.4, 0.7, 1.0, 1.2, and 1.4 cm. The pulses at the smaller 4 gap settings all exhibit a lag of I behind V similar to that seen in the high-impedance pulses of figures 25 and 26. Those at the 1.4-cm gap, however, are almost exactly coincident.

A distinct difference between the low- and high-impedance pulse shapes is the almost complete absence of secondary maxima in the former. This general trend is qualitatively consistent with the charge-line model, which predicts smaller and smaller secondary pulses as the line impedance of 59 ohms is approached. Although the model predicts negative secondary maxima when the load impedance is below 59 ohms, as it is in the low-impedance mode, only positive ones are observed. This disagreement may be due to the great oversimplification of the FE diode dynamics in this model.

### 3.4 Shorted Diode Pulses

Since the V monitor must of necessity be separated by some distance from the cathode-anode gap, there is a contribution,  $V_L$ , to the V signal due to the finite inductance, L, between the point of measurement and the gap. This contribution is given by

$$V_L = L \frac{dI}{dt} \quad (24)$$

This contribution must be subtracted from the total measured V signal to obtain the actual diode voltage. The value of L is a function only of the tube-extension and shank diameters. There is, therefore, one value to be used for all the high-impedance pulses and one for all the low-impedance pulses.



We measured  $L$  by shorting out the diode and by applying equation (24) to the measured  $V$ -monitor signal and time derivative of the  $I$  signal. The geometries of the shorted diodes in the two modes is shown in figure 29.  $V$  and  $I$  pulses obtained in this manner for both the high- and low-impedance modes are shown in figures 30 and 31, respectively. Also shown in these figures are plots of  $V$  and  $\frac{dI}{dt}$  on common sets of axes, obtained by digitizing the corresponding oscillograms and by applying a 2-ns time delay to the  $V$  trace to bring  $V$  and  $\frac{dI}{dt}$  into synchronization. The agreement between the time dependence of  $V$  and that of  $\frac{dI}{dt}$  predicted by equation (24) is seen to be excellent in the low-impedance mode. The result for  $L$  is

$$L \text{ (low impedance)} = 25 \text{ nH} . \quad (25)$$

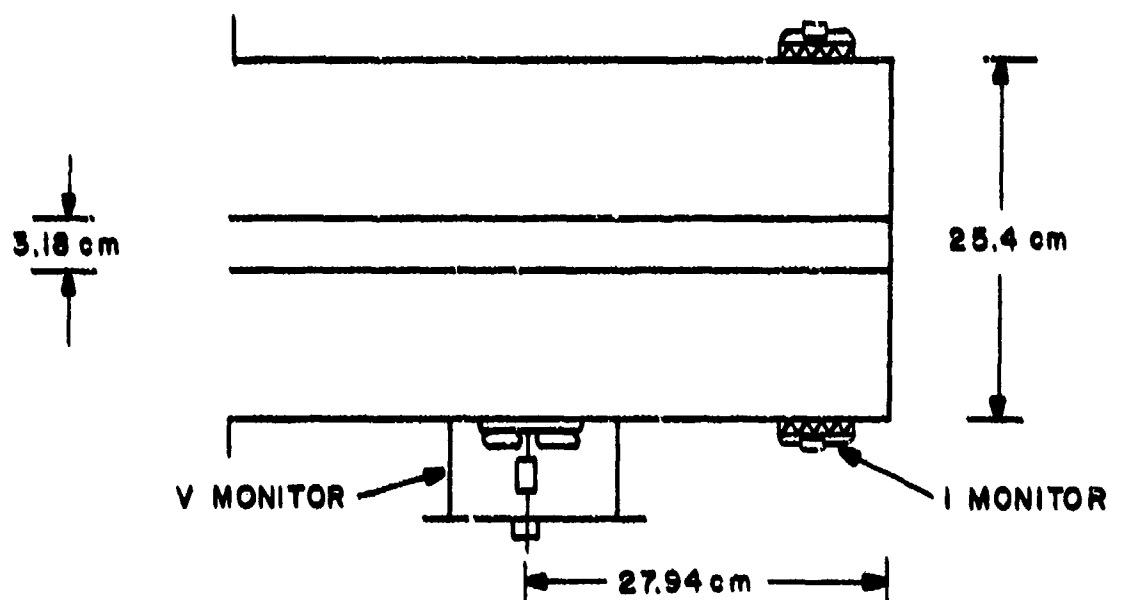
The agreement in the high-impedance mode is, however, quite poor, with most of the maxima and minima in  $V$  occurring out of phase with those of  $\frac{dI}{dt}$ . The best that can be done is to disregard the phase mismatch and individually line up pairs of corresponding peaks. The resulting estimate for  $L$  is

$$L \text{ (high impedance)} = 176 \text{ nH} . \quad (26)$$

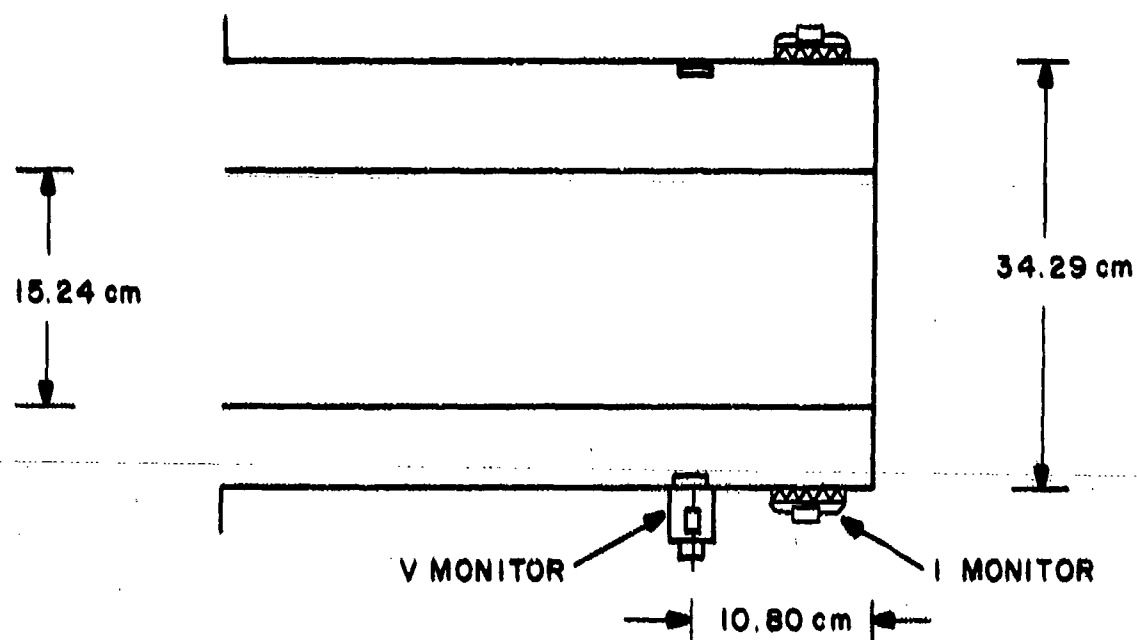
Estimates of  $L$  for the high- and low-impedance modes can be made using the coaxial geometry formula

$$L = 20 \left( \ln \frac{D}{d} \right) s \text{ nH} , \quad (27)$$

where  $s$  is the distance in centimeters from the  $V$  monitor to the anode (fig. 29 shows these dimensions). Substitution of these dimensions into equation (27) yields 116 nH for the high-impedance geometry and 17.5 nH for the low-impedance geometry. Thus, the coaxial inductance accounts for only about 70 percent of the value obtained from the shorted-diode  $V$  and  $I$  pulses.



**SHORTED HIGH-IMPEDANCE DIODE**



**SHORTED LOW-IMPEDANCE DIODE**

Figure 29. Shorted-diode geometries.

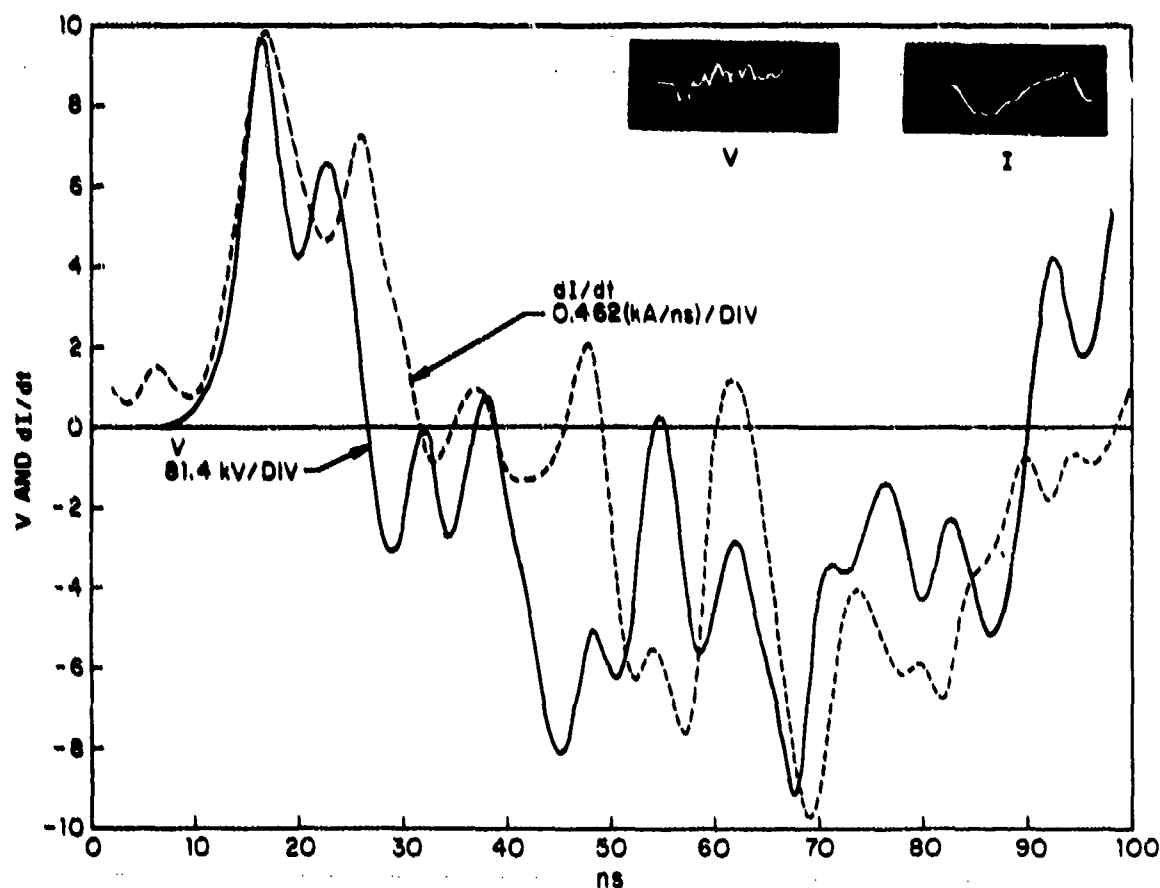


Figure 30. Pulses from shorted high-impedance diode  
 Inset: scope traces, X scale: 20 ns/div.  
 Main:  $V$  and  $\frac{dI}{dt}$ .

Figure 32 illustrates the effect on the time relationship of  $V$  and  $I$  of applying the correction in equation (24) to the  $V$ -monitor data, for the high-impedance diode with  $G = 2.6$  cm and  $V_c = 3.0$  MV. The upper traces are those of uncorrected  $V$  and  $I$ , i.e., the same data as the lower traces of figure 26, but plotted to different scales. In the lower traces of figure 32,  $V$  has been corrected, with  $L = 176$  nH. It can be seen that correcting the data brings the primary peaks of  $V$  and  $I$  closer in time. Figure 32 also shows the variation of diode impedance,  $Z = V/I$ , with time based on the respective  $V$  and  $I$  traces. The

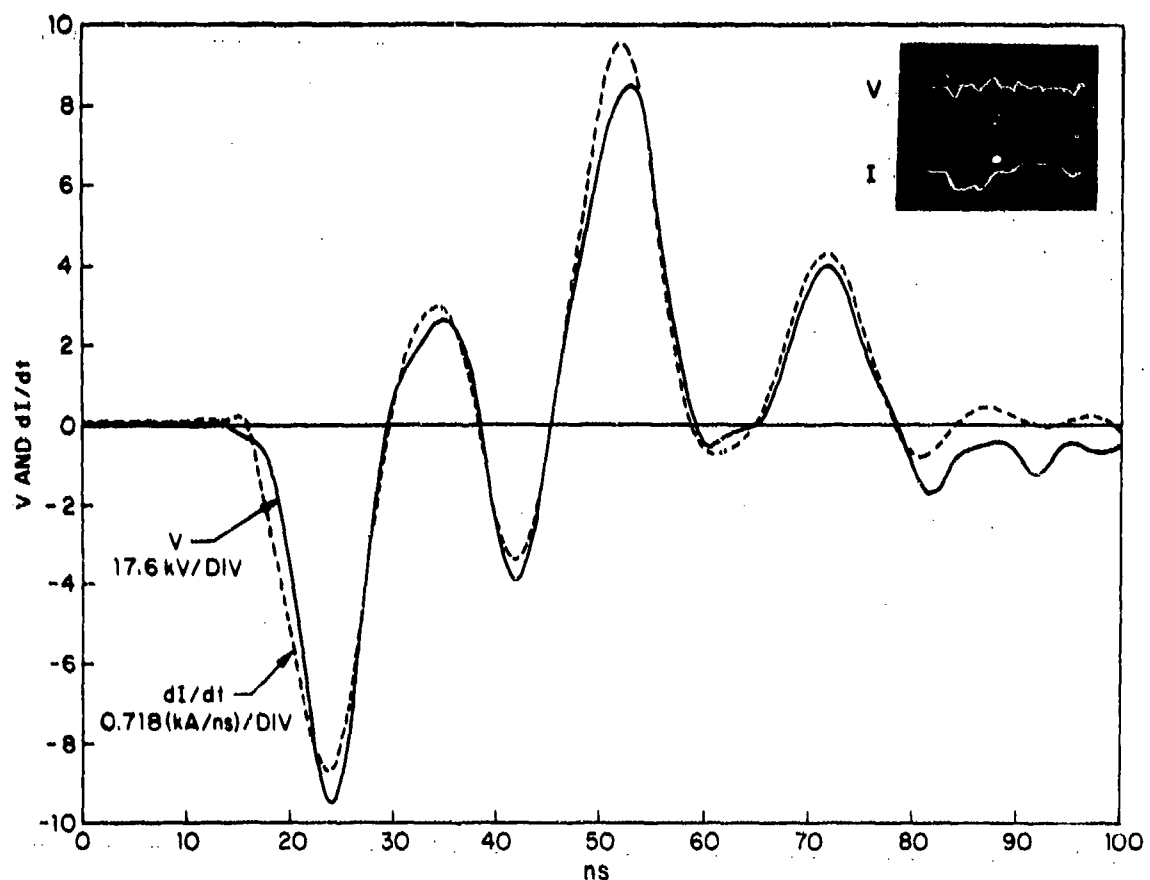


Figure 31. Pulses from shorted low-impedance diode  
 Inset: scope traces, X scale: 20 ns/div.  
 Main:  $V$  and  $\frac{dI}{dt}$ .

correction reduces the amplitude of the oscillation of  $Z$  during the time in which the diode is conducting, but it hardly affects the mean impedance value of 90 ohms during this period.

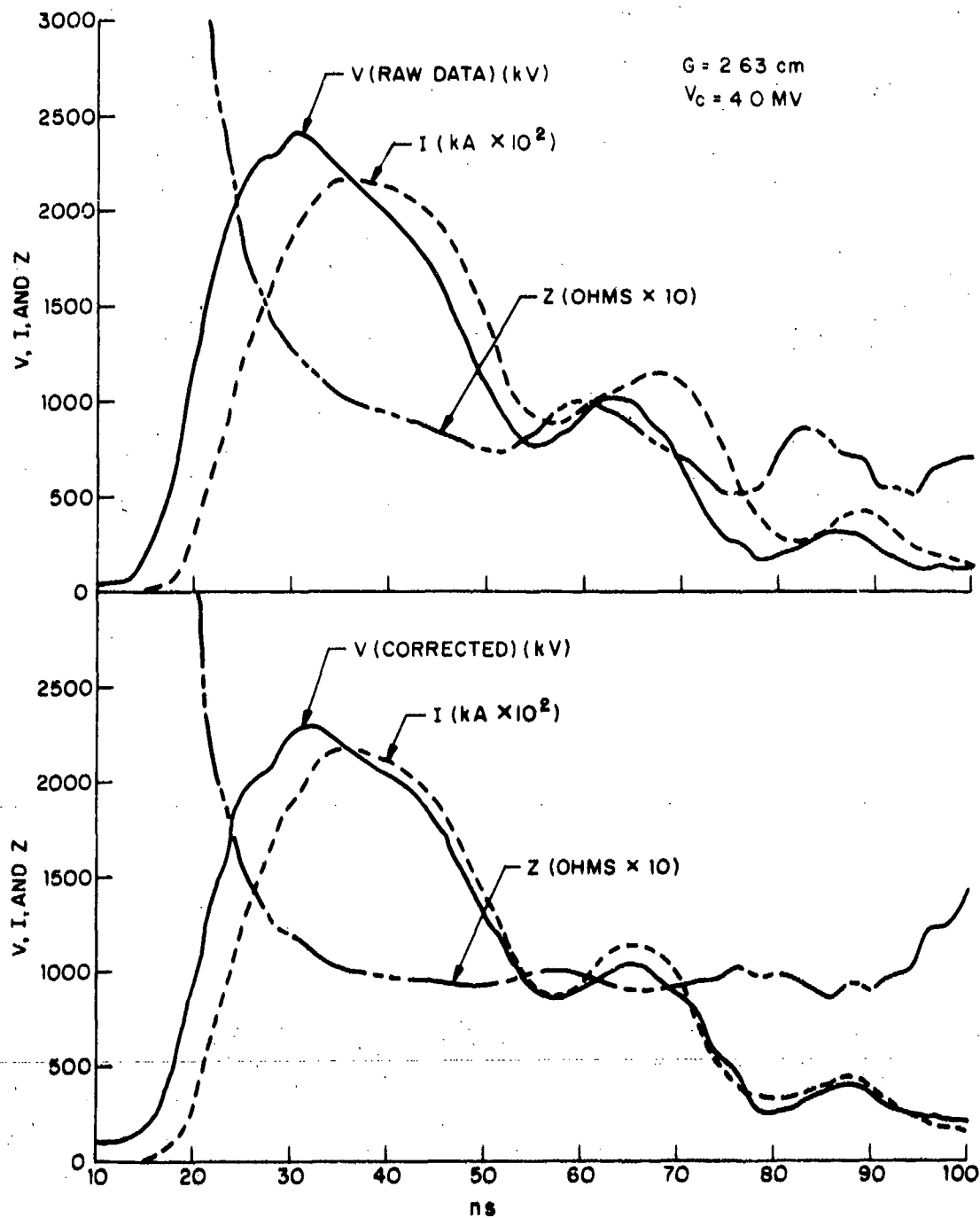


Figure 32. V, I, and Z traces: uncorrected (top) and corrected (bottom) by  $I \frac{dI}{dt}$ .

## 4. ANALYSIS OF MONITOR PULSES

### 4.1 Introduction

The two most important types of information yielded by the V- and I-monitor pulses are the diode impedance (sect. 4.3 and 4.4) and the electron energy spectrum (sect. 4.5). The spectrum was obtained in the form of a histogram in which each ordinate is the sum of integrals of I over time intervals during which the voltage varied within some small range. Other quantities of interest are the instantaneous power,  $VI$ , its time integral over the pulse (the total energy deposited), the theoretical gamma dose rate  $\dot{R}$  (based on V and I), and the integral of  $\dot{R}$  over the pulse. The latter two were compared directly with the scintillator-photodiode pulses and TLD dose measurements (sect. 4.6).\*

### 4.2 Computer Program and Data Input

All the above analyses of the V and I pulses were performed with a modified version of the EBSPEC computer program.<sup>3</sup> The program computes analytic expressions for the V and I pulses from input data points by making least-squares fits of groups of six consecutive data points to a cubic polynomial. The resulting expression is then used to represent V or I in the central time interval. The program also corrects the voltage for the RC decay in the V monitor (see app A) and subtracts the  $L \frac{dI}{dt}$  correction discussed in section 3.4. Further, the program will optionally output  $\frac{dI}{dt}$  for purposes of finding L from the data of a shorted diode pulse (sect. 3.4), and insert an artificial time delay between the V and I pulses.

---

\*Many useful suggestions on the interpretation of the V and I pulses were given by A. G. Stewart and S. E. Graybill.

<sup>3</sup>Program EBSPEC, Simulation Physics Corp. TR-71-05 (August 1971).

21

The discrete data points for input to the computer program were obtained from the oscilloscope traces by projecting either the polaroids themselves (by means of an opaque projector) or negatives made from the polaroids (by means of a Vu-graph projector). The projection screen was a blackboard on which was mounted a sheet of graph paper. The trace was drawn on the graph paper, resulting in a permanent, enlarged record of the pulse from which quantitative information could be easily read. The maximum uncertainty in obtaining digital information in this manner is estimated to be 5 percent, which is no greater than the pulse-height error inherent in the oscilloscope itself for such fast pulses.

On some occasions discrete points were obtained from the oscilloscope traces by an optical enlarging and recording device designed specifically for this purpose.\* This method was generally found to be quite tedious and tiring to the eyes, especially when attempts were made to obtain information from many traces in one long sitting. The one advantage of this device over the projection method was that it was possible to record the ordinates and abscissas directly on punched cards, which could then be converted to the format required for the modified EBSPEC program by means of an auxiliary program.

#### 4.3 Diode Impedance in High-Impedance Mode

Two approaches (approach 1 and approach 2) were used to obtain information on diode impedance in the high-impedance mode. In approach 1, all impedance values were based solely on peak V and I values. Approach 1 thus ignores various complexities in the diode-conduction process which have the effect of delaying the times of peak I relative to peak V, or vice versa. In approach 2, the instantaneous value of  $Z = V/I$  was plotted against time for individual

---

\*H. Dell Foster Co., San Antonio, TX.

pulses. Although approach 2 does not, in general, lead to a unique value of  $Z$  for a particular pulse, it gives a more complete picture of the diode-conduction time history than does approach 1, and usually points to a reasonable characteristic impedance of the diode.

Figures 33 through 36 show the primary and secondary peak  $V$  and  $I$  recorded by the HDL-built monitors as a function of machine charge voltage,  $V_c$ , for four hemisphere-to-plane diode geometries. The  $V$  values have not been corrected for  $L \frac{dI}{dt}$  (sect. 3.4). Some of the measurements for the 2.6- to 2.8- and 3.8-cm geometries, which were made on a number of different occasions, indicate that reproducibility is at times as poor as  $\pm 0.3$  MV and  $\pm 3$  kA. The monotonic increase of both  $V$  and  $I$  with  $V_c$  in all cases is, however, quite clear.

The  $V$ - $I$  characteristics based on the data of figures 33 through 36 are plotted in figures 37 through 44. Also shown on each plot is the least-squares fit of the data to the forms

$$I = V/Z \quad (28)$$

for an Ohm's law conductor, and

$$I = CV^{3/2} \quad (29)$$

The latter equation, in which  $C$  is a constant, is the Langmuir-Childs law for a plane-parallel diode in the space-charge limited regime. The indicated index for each fit relates to the improvement of the fit over a random fit, and approaches unity as a perfect fit is approached. In general, the data based on the primary peaks of  $V$  and  $I$  seem about equally well represented by both forms, except possibly for the  $G = 2.1$ -cm data, which are better represented by the Langmuir-Childs form. The data based on the secondary peaks, on the other hand, are not well represented by either form, suggesting that the conduction mechanism in the diode at later times is quite different from that at earlier times.



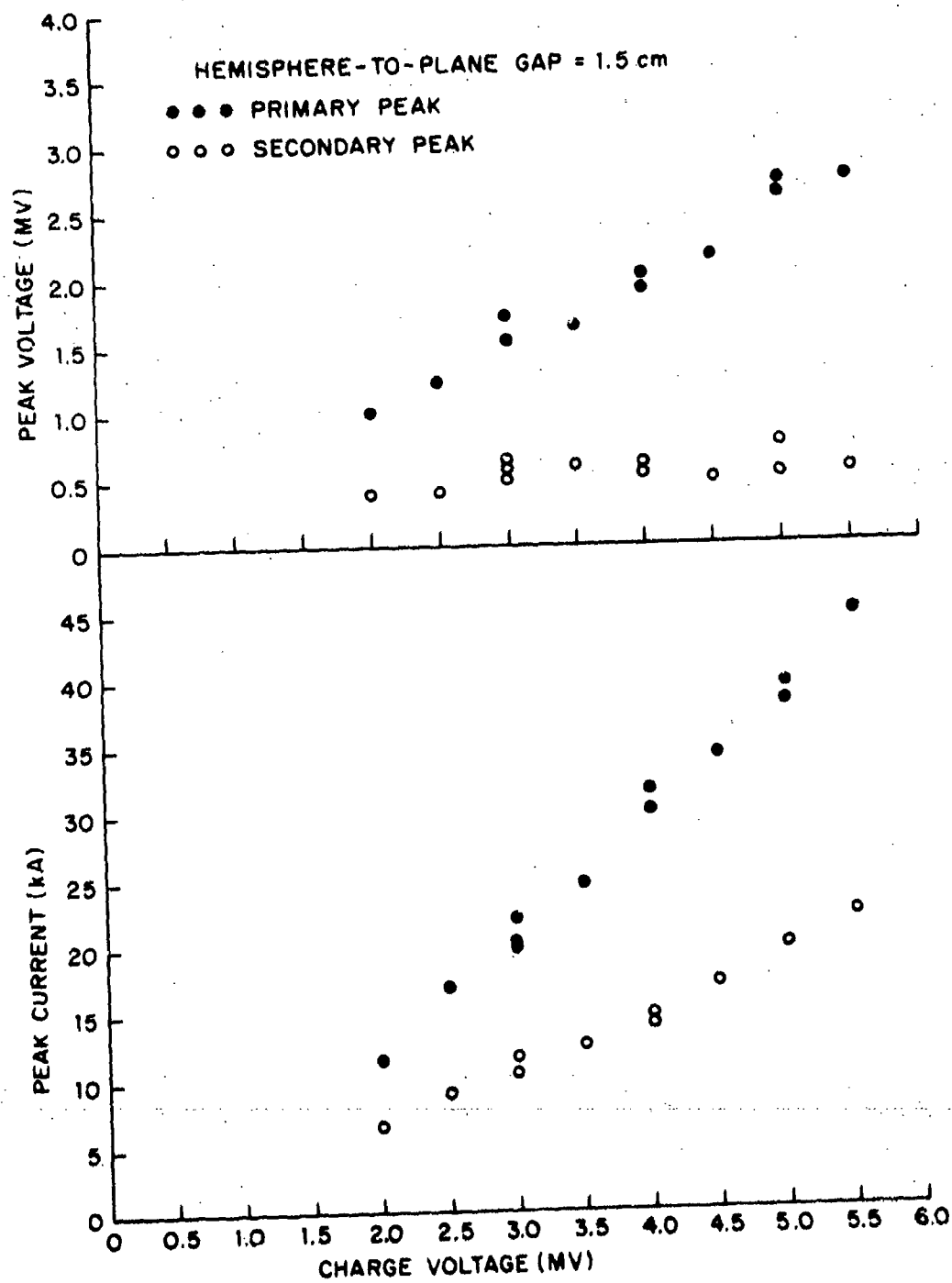


Figure 33. Peak V and I versus charge voltage for  $G = 1.5$  cm hemi-plane diode.

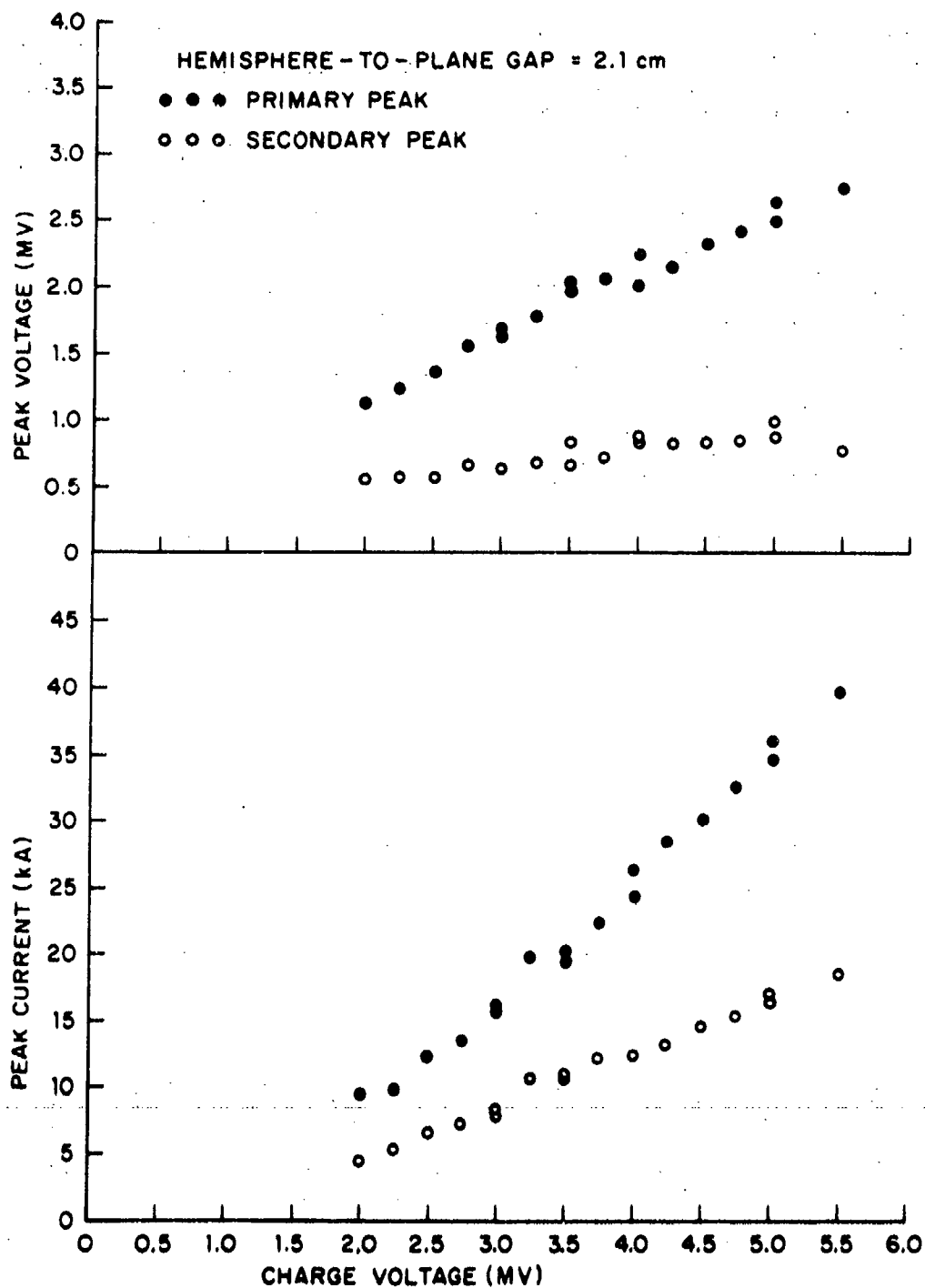


Figure 34. Peak V and I versus charge voltage for  $G = 2.1$  cm hemi-plane diode.

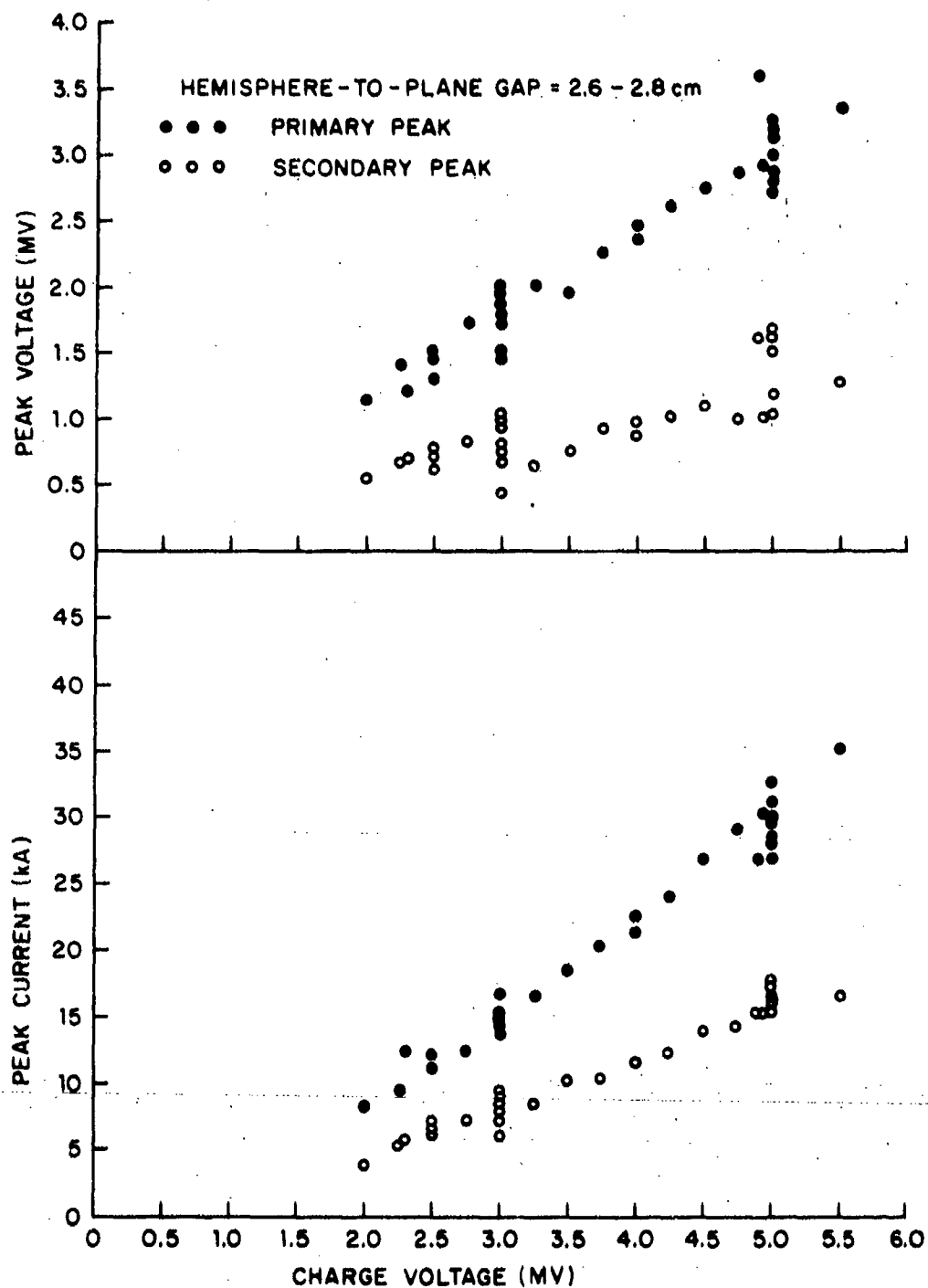


Figure 35. Peak V and I versus charge voltage for G = 2.6 to 2.8 cm hemi-plane diode.

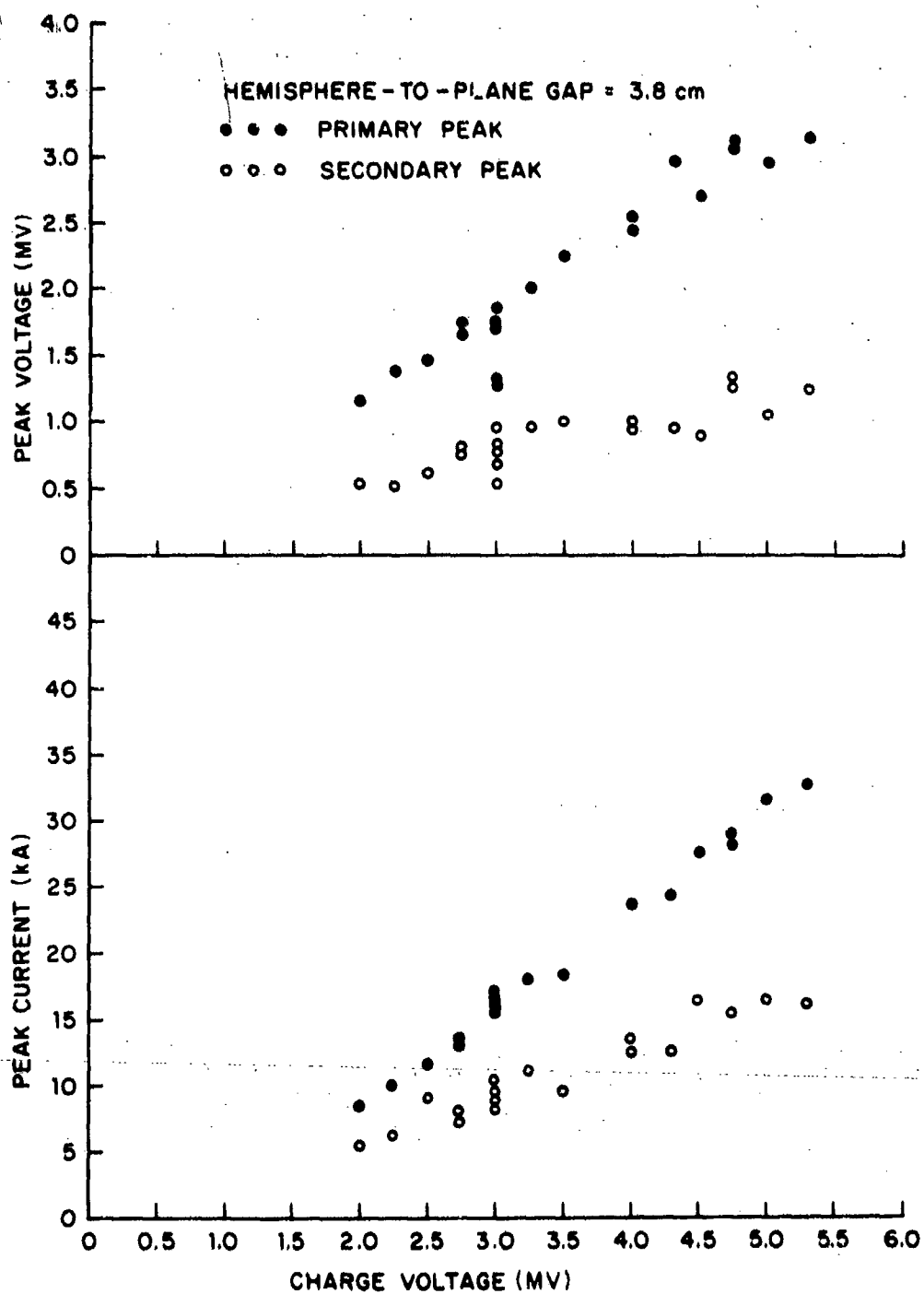


Figure 36. Peak V and I versus charge voltage for  $G = 3.8$  cm hemi-plane diode.

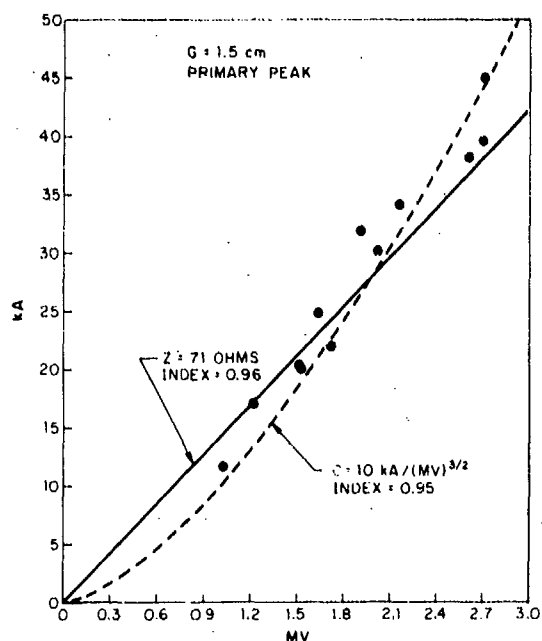


Figure 37. V-I characteristics for  $G = 1.5$  cm hemi-plane diode; primary peak.

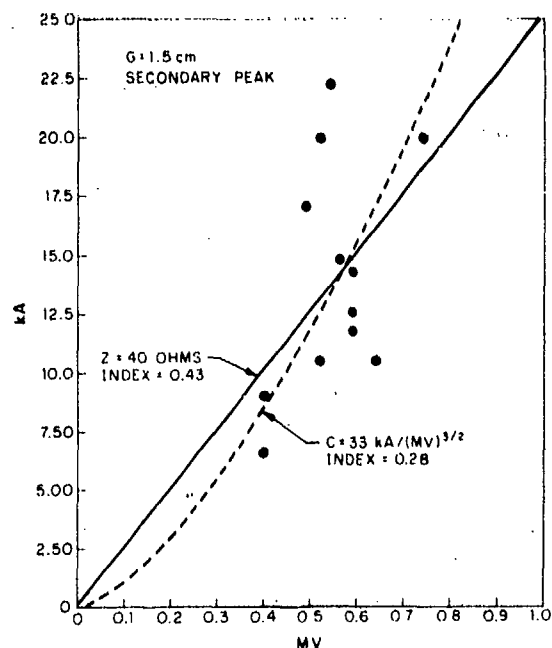


Figure 38. V-I characteristics for  $G = 1.5$  cm hemi-plane diode; secondary peak.

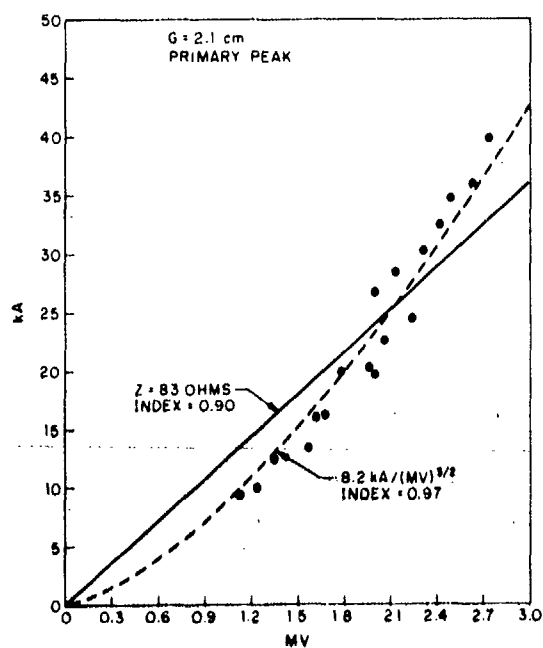


Figure 39. V-I characteristics for  $G = 2.1$  cm hemi-plane diode; primary peak.

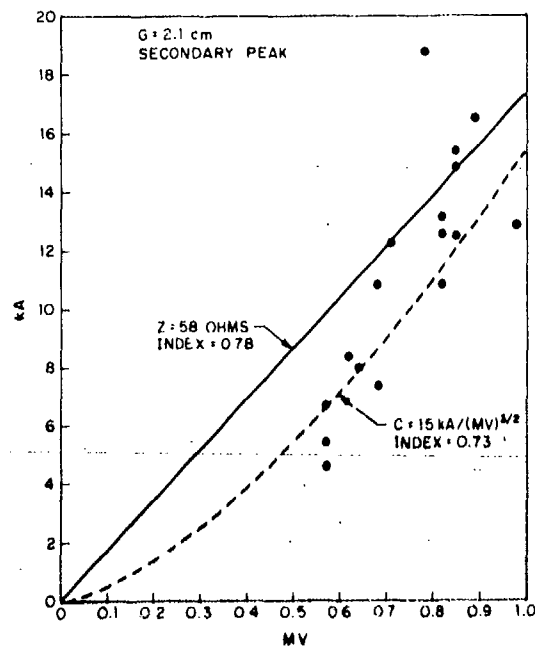


Figure 40. V-I characteristics for  $G = 2.1$  cm hemi-plane diode; secondary peak.

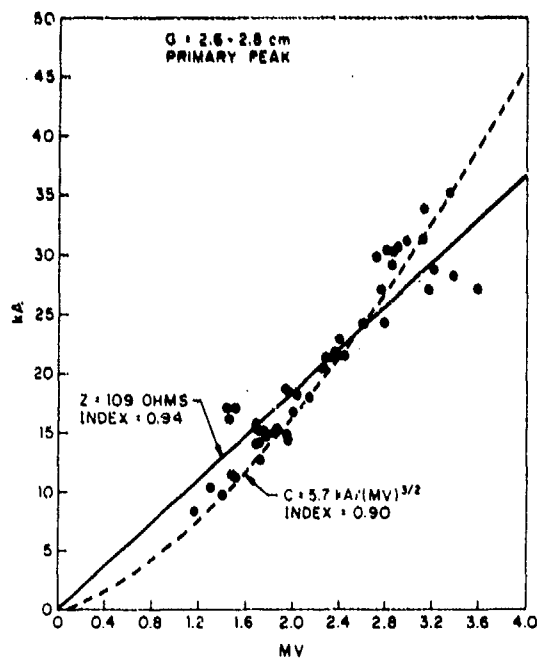


Figure 41. V-I characteristics for  $G = 2.6$  to  $2.8$  cm hemi-plane diode; primary peak.

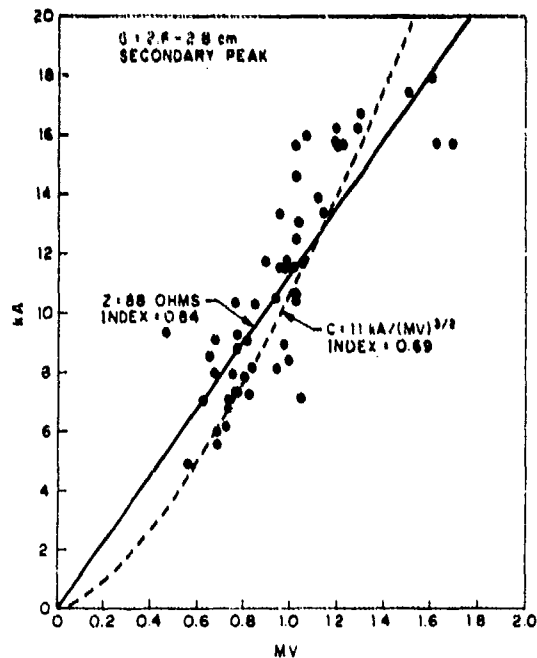


Figure 42. V-I characteristics for  $G = 2.6$  to  $2.8$  cm hemi-plane diode; secondary peak.

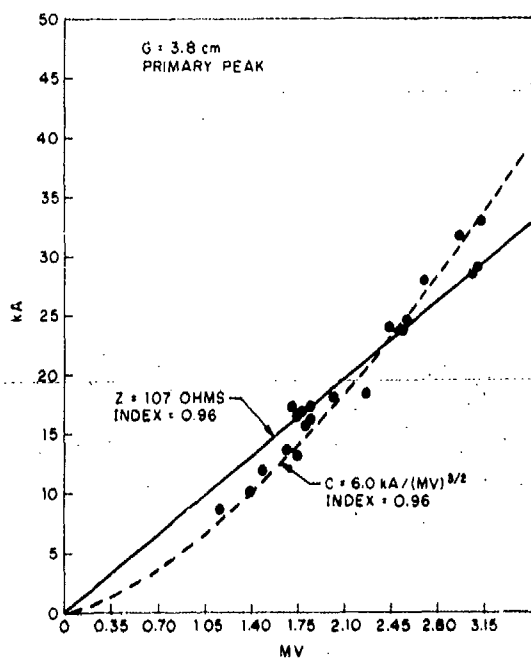


Figure 43. V-I characteristics for  $G = 3.8$  cm hemi-plane diode; primary peak.

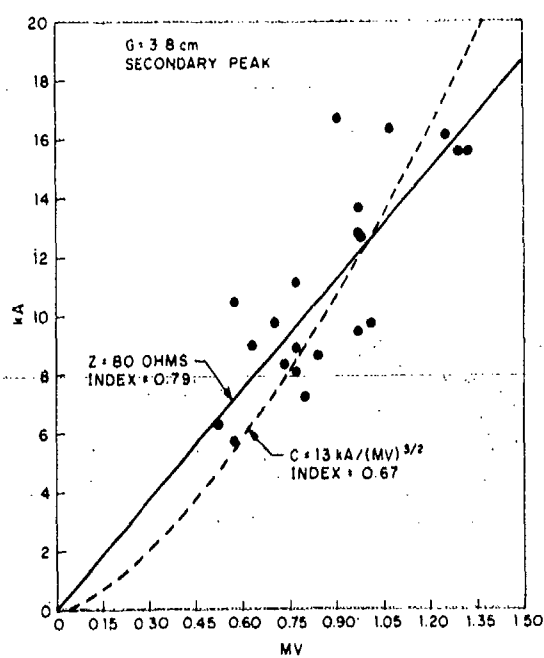


Figure 44. V-I characteristics for  $G = 3.8$  cm hemi-plane diode; secondary peak.

Values of  $Z$  from approach 1, based on the primary peak data are summarized in table III. The  $Z$  value of 107 ohms for the largest value of  $G$  is in disagreement with that found for similar diode geometries at the Hermes machine.<sup>4</sup> At that facility the tube impedance was found to have the value

$$Z_T = 30 \ln(b/a) \quad (30)$$

where

$b$  = diameter of tube extension, and

$a$  = diameter of cathode tip.

This  $Z$  value was obtained independently of  $G$  as long as the latter was approximately  $a$  or greater. In our case this condition is satisfied for  $G \geq 3.0$  cm, and equation (30) would yield 62 ohms.

TABLE III. HIGH-IMPEDANCE CHARACTERISTICS BASED ON PRIMARY PEAKS OF  $V$  AND  $I$

$G$ (cm)	$Z$ (ohms)	$C_{th}$ (kA/MV <sup>3/2</sup> )	$C_{obs}$ (kA/MV <sup>3/2</sup> )	$\frac{C_{obs}}{C_{th}}$	$A_{eff}$ (cm <sup>2</sup> )
1.5	71	16.4	10	0.61	9.6
2.1	83	8.4	8.2	0.98	15.4
2.7	109	5.1	5.7	1.12	17.7
3.8	107	2.6	6.0	2.30	36.5

<sup>4</sup>T. H. Martin, K. R. Prestwich, and D. L. Johnson, Summary of the Hermes Flash X-Ray Program, Sandia Laboratories Report SC-RS-69-421 (October 1969).

Table III also compares observed and theoretical values of  $C$ , labelled  $C_{obs}$  and  $C_{th}$ , respectively.  $C_{obs}$  was obtained from the  $V^{3/2}$  fit of equation (29), and  $C_{th}$ , the Langmuir-Childs constant, is given by

$$C_{th} = \frac{2.34A}{G^2} \text{ kA/MV}^{3/2} \quad (31)$$

Here,  $A$  is the electrode area in  $\text{cm}^2$ , and  $G$  is the cathode-anode gap in cm. For the 3.18-cm diam hemispherical surface,  $A = 2\pi r^2 = 15.8 \text{ cm}^2$ . One interpretation (alluded to by Sazama and Stewart<sup>1</sup>) of the increase of the ratio  $C_{obs}/C_{th}$  from below unity to above unity as  $G$  increases is that emission takes place from larger and larger portions of the hemispherical surface with increase in  $G$  and gradually extends back to the cylindrical portion of the cathode shank. The areas,  $A_{eff}$ , of this emission (derived from equation (31) with  $C_{th}$  replaced by  $C_{obs}$ ) are given in the last column of table III. A detailed field plot at the cathode-anode region for each value of  $G$  might indicate how valid this interpretation is.

To obtain  $Z$  by approach 2, plots of  $Z$  versus  $t$  are needed. Such plots are shown in figures 45 through 49. When the  $V$  and  $I$  pulses were synchronized by methods 1 or 2 (sect. 3.2) involving the HIFX triggering system, an artificial delay between 0 and 6 ns was introduced between  $V$  and  $I$ , and the one chosen was that which yielded the smoothest time variation of  $Z$  during the conduction period of the diode, i.e., the central 30 ns or so of the trace. Figure 50 compares the behavior of  $Z$  during this period for various artificial time delays for the diode with  $G = 2.83 \text{ cm}$  and  $V_c = 4 \text{ MV}$ . The amplitudes of the  $Z$  variations for 2- and 4-ns delays are seen to be smaller than those for 0- and 6-ns delays.

<sup>1</sup>F. J. Sazama and A. G. Stewart, *Design and Testing of a Current and Voltage Monitor for HIFX*, Harry Diamond Laboratories TR-1558 (August 1971).



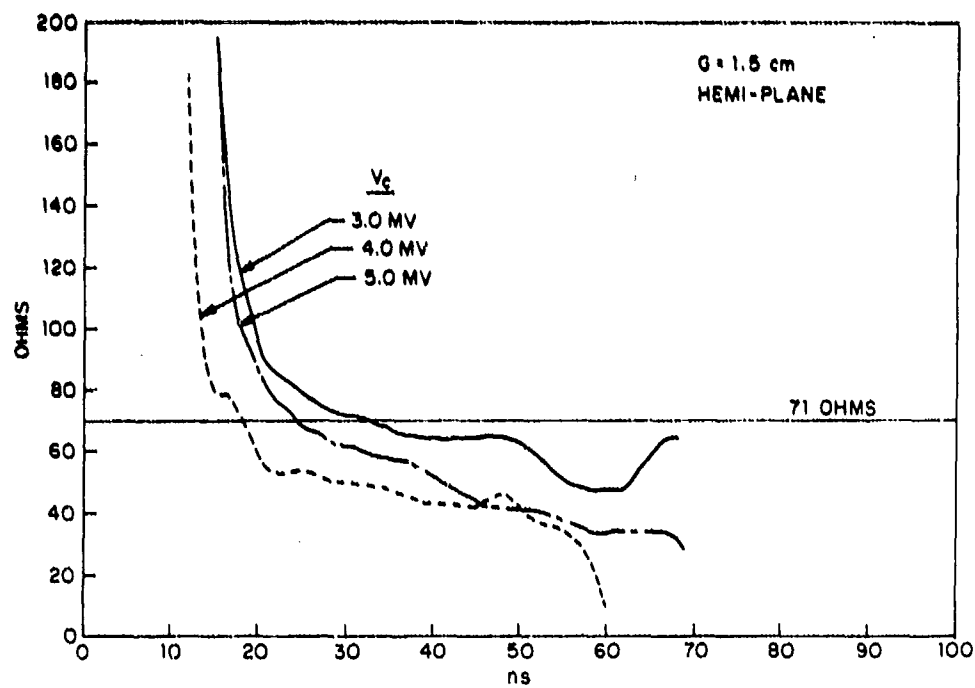


Figure 45. Impedance histories for  $G = 1.51 \text{ cm}$  hemi-plane diode.

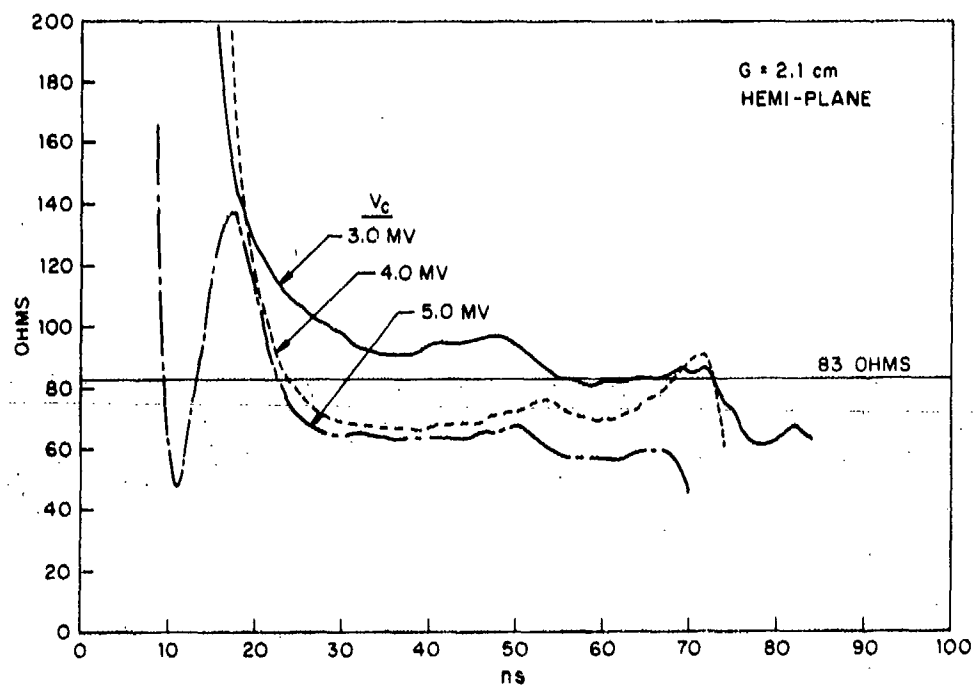


Figure 46. Impedance histories for  $G = 2.1 \text{ cm}$  hemi-plane diode.

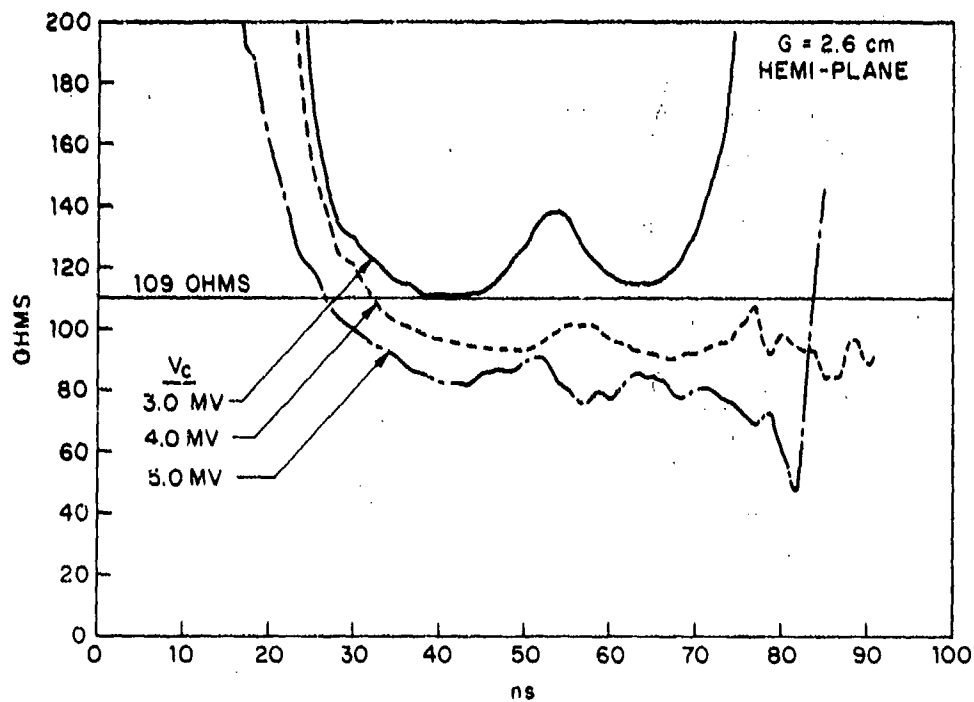


Figure 47. Impedance histories for  $G = 2.6$  cm hemi-plane diode.

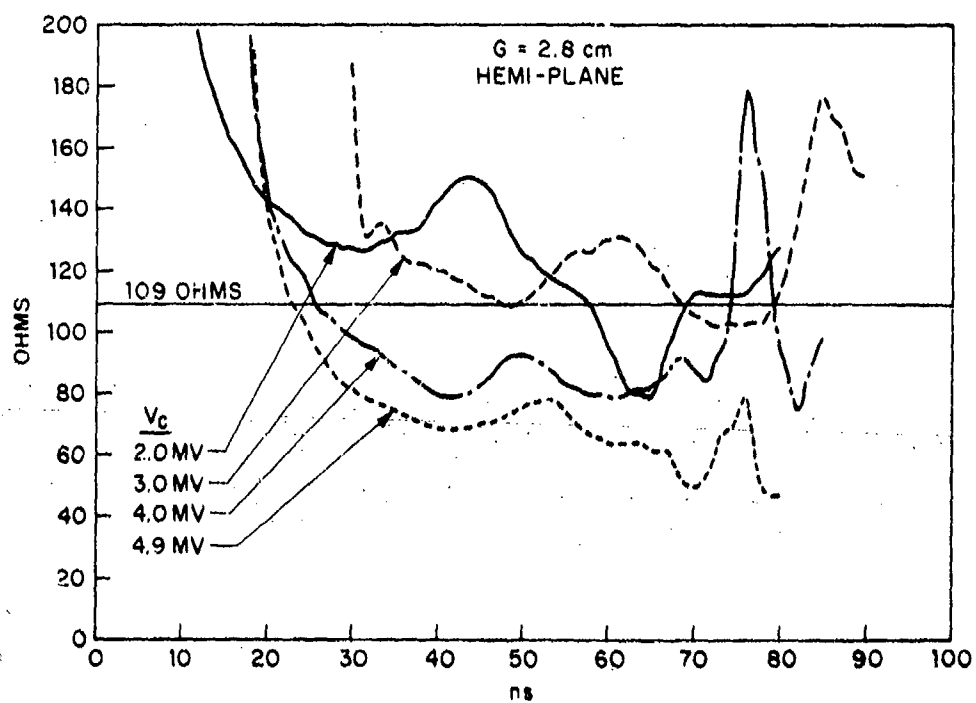


Figure 48. Impedance histories for  $G = 2.8$  cm hemi-plane diode.

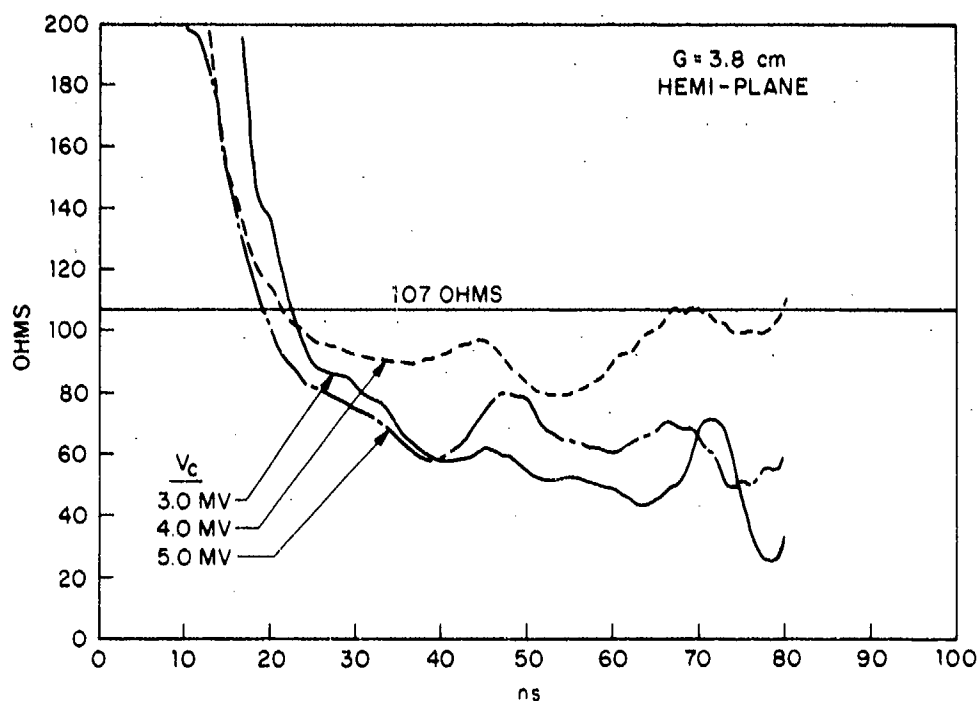


Figure 49. Impedance histories for  $G = 3.8$  cm hemi-plane diode.

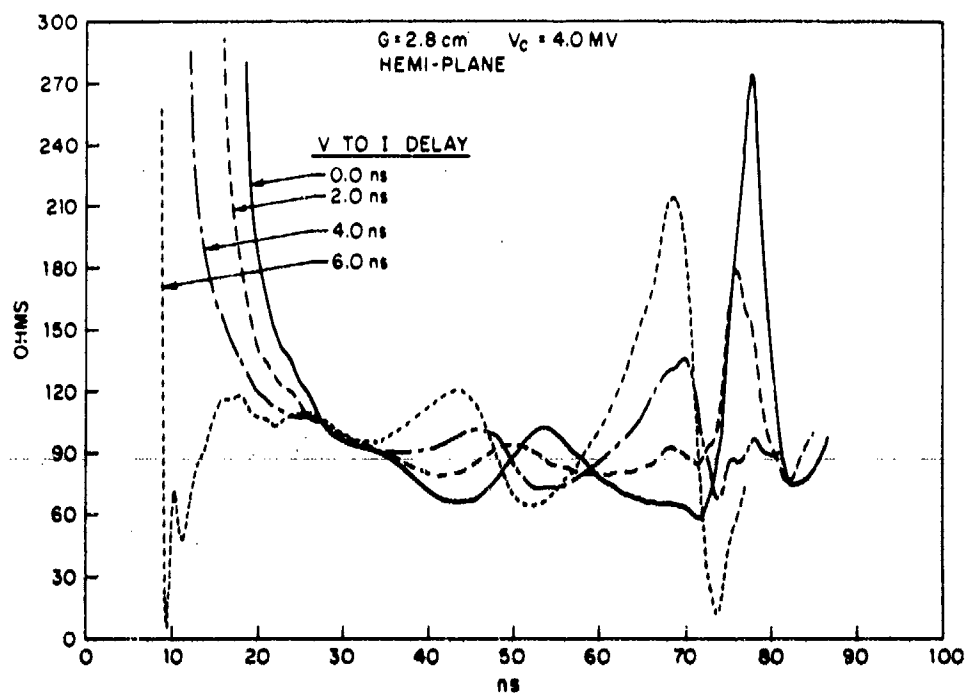


Figure 50. Impedance histories for  $G = 2.8$  cm hemi-plane diode for various delays of  $V$  relative to  $I$ .

Most of the impedance histories in figures 45 through 49 can be reasonably characterized as first going through a turning-on period lasting 10 to 20 ns, during which  $Z$  drops rapidly, and then settling down to a conduction period, lasting about 30 ns, in which  $Z$  is relatively constant. A few of the histories, such as the 3- and 5-MV traces for  $G = 2.6$  cm (fig. 47), also show signs of a turning-off period following the conduction period, during which the impedance increases rapidly. However, other, more complicated features in the  $Z$  versus  $t$  plots also occur. Examples are the large inflections that appear in the turning on-period for the 5-MV  $Z$  where  $G = 2.1$  cm (fig. 46) and during the conduction periods of the 2- and 3-MV  $Z$ 's where  $G = 2.8$  cm (fig. 48) and the 3-MV  $Z$  where  $G = 2.6$  cm (fig. 47). These anomalies are not, in general, reproducible, and thus are probably not results of specific properties of those particular diodes.

Figures 45 through 49 also show the diode impedance values resulting from approach 1, i.e., from peak  $V$  and  $I$  values. For the 2.1-, 2.6-, and 2.8-cm diodes, these values all fall within the range of the conduction period impedances for the various values of  $V_c$ . The close agreement of the  $Z$ 's from both approaches where  $G = 2.6$  cm might have been expected in view of the similarity in shape and near coincidence in time of the  $V$  and  $I$  pulses from this diode even before the  $\frac{dI}{dt}$  correction is applied (see fig. 25 and 26). In addition, the  $\frac{dI}{dt}$  correction usually improves the time coincidence of  $V$  and  $I$ , as demonstrated in figure 32. Where  $G = 1.5$  cm (fig. 45), the value of  $Z$  based on approach 1 agrees fairly well with the average  $Z$  for the three  $V_c$ 's at the beginning of the conduction period, but then  $Z$  seems to decrease during the conduction period rather than remain constant. Only for the 3.8-cm diode (fig. 49) is there gross disagreement between the  $Z$  values based on approach 1 and approach 2 for all three  $V_c$ 's, where the former  $Z$  is considerably larger.

Table IV gives the Z values from approach 2, based on impedance during the conduction period for the cases in figures 45 through 49. At  $V_c = 3.0, 4.0,$  and  $5.0$  MV, Z increases between  $G = 1.5$  and  $G = 2.6$  cm, and either drops off or seems to remain constant at higher values of G. The 70-ohm average conduction period impedance of the 3.8-cm diode is in fair agreement with the 62-ohm value predicted from equation (30).<sup>4</sup> This agreement contrasts with the disagreement of the 107-ohm value based on approach 2, as noted previously.

TABLE IV. HIGH-IMPEDANCE VALUES (OHMS)  
BASED ON IMPEDANCE TIME  
HISTORIES

G (cm)	$V_c$ (MV)			
	2.0	3.0	4.0	5.0
1.5		63	43	50
2.1		85	65	60
2.6		120	95	80
2.8	120	120	90	70
3.8		55	90	70

#### 4.4 Diode Impedance in Low-Impedance Mode

Figure 51 shows the peak I and V recorded by the SPI-built monitors in the low-impedance mode uncorrected for  $L \frac{dI}{dt}$  and plotted as a function of G, all at  $V_c = 4.1$  MV. I is less sensitive than V to variations in G because diode impedance is less than the line impedance of 59 ohms. This behavior has also been observed in the low-impedance diodes of other machines.<sup>5</sup> Figure 52

shows that, for gap spacings of 0.4, 0.7, and 1.4 cm, peak V decreases while peak I remains relatively constant as cathode-emitter diameter is increased. Reproducibility of V and I is similar to that noted for the high-impedance mode.

<sup>4</sup>T. H. Martin, K. R. Prestwich, and D. L. Johnson, Summary of the Hermes Flash X-Ray Program, Sandia Laboratories Report SC-RS-69-421 (October 1969).

<sup>5</sup>G. Yonas and P. Spence, Experimental Investigations of High  $v/v_e$  Electron Beam Transport, Physics International FR-106 (1968).

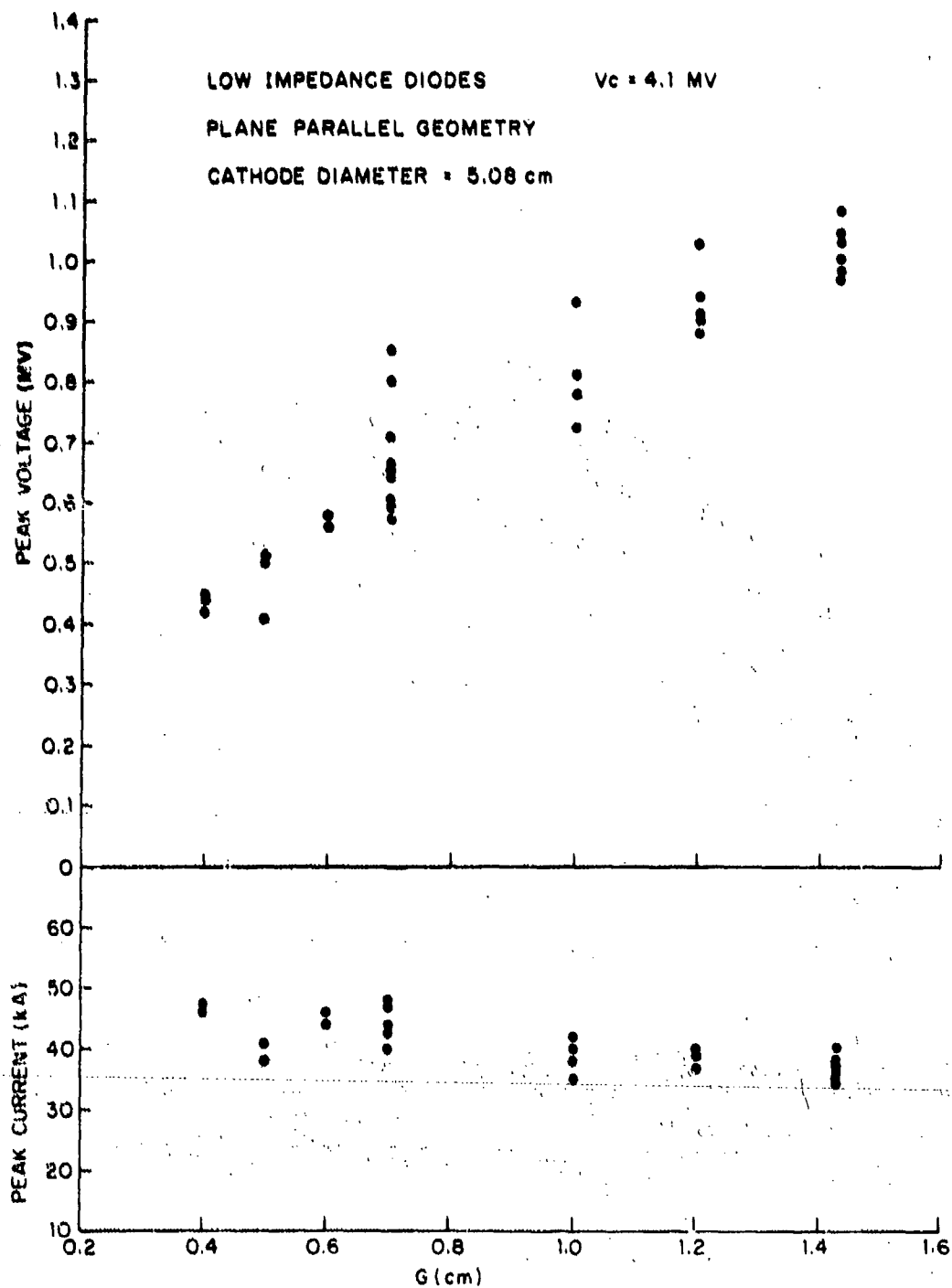


Figure 51. Peak  $V$  and  $I$  versus cathode-anode gap for low-impedance diodes.

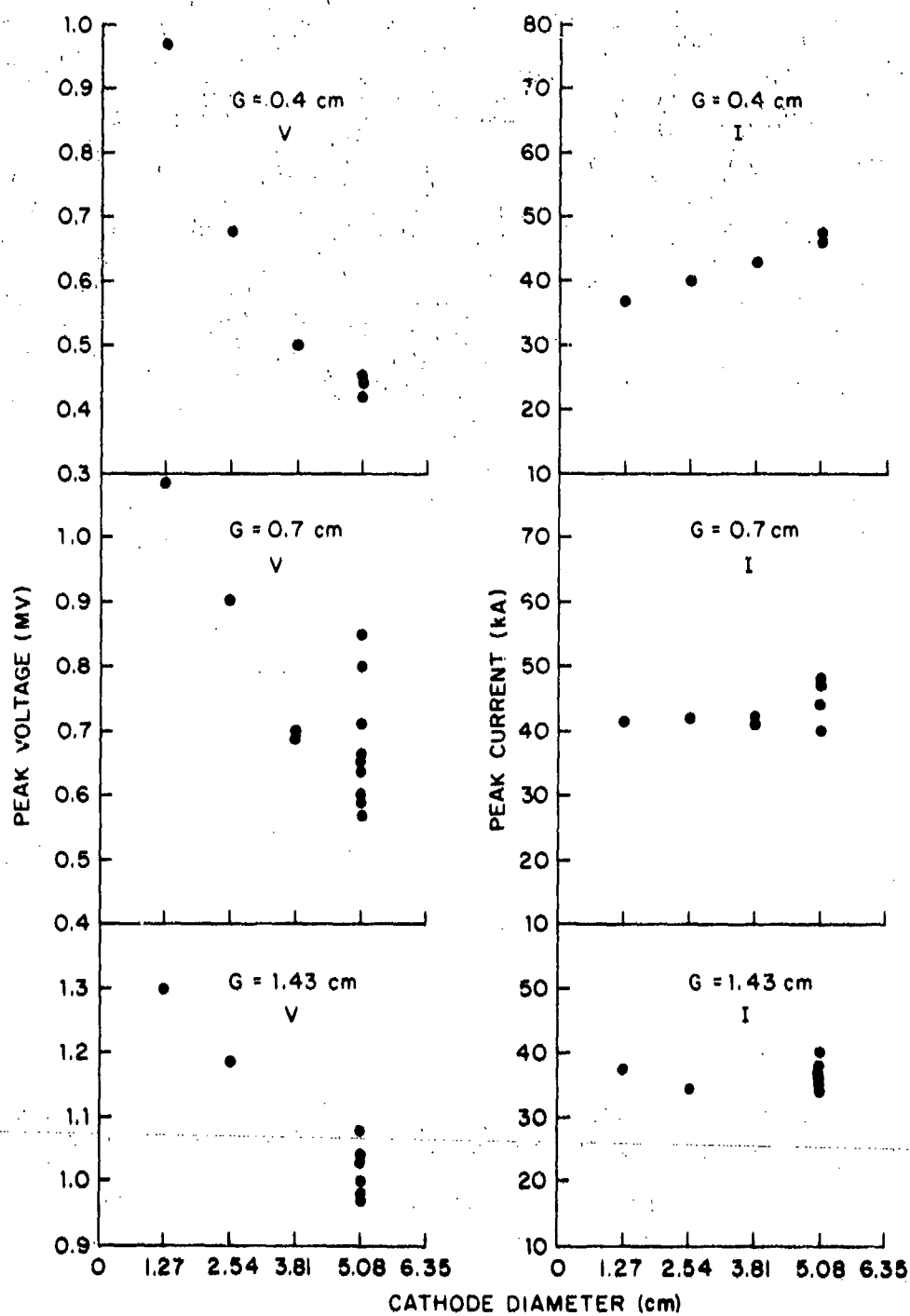


Figure 52. Peak V and I versus cathode emitter diameter for low-impedance diodes.

Because low-impedance data are available at only one charge voltage,  $V_C = 4.1$  MV, it is more practical to seek impedance information by approach 2 than by approach 1. Impedance time histories are shown for the low-impedance diode geometries in figures 53 through 57. One can gain an idea of the reproducibility of these impedance histories from figures 55, 56, and 57. In these figures, two or more histories appear for the 5.08-cm diam emitter with cathode-anode gaps of  $G = 1.0$ , 1.2, and 1.4 cm. In general, the histories are characterized by short turn-on times followed by about a 30-ns conduction period just as in the high-impedance mode. Most of the traces also show the turn-off period following the conduction period. At  $G = 1.4$  cm, however (fig. 57), the conduction period is shorter than the usual 30 ns or so, in three of the traces. Since all these data were obtained by synchronization method 3 (sect. 3.2), which does not depend on the HIFX triggering system, no artificial delays between V and I were applied in the EBSPEC program analysis. In general, relative variations in Z during the conduction period are less than those observed in figures 45 through 49 for the high-impedance mode. However, anomalous inflections, similar to those noted in the high-impedance mode, do sometimes occur.

The values of impedance during the conduction period based on the traces in figures 53 through 57 are shown in table V. Evident in these values is the monotonic increase of Z with G for fixed-emitter diameter as well as the increase in Z with decreasing diameter for fixed G, which would be expected for Langmuir-Childs-like diodes. Sparsity of data at diameters other than 5.08 cm and the absence of data at charge voltages other than  $V_C = 4.1$  MV, however, make a quantitative comparison impractical. Nevertheless, it may be said that the range of diode impedances obtained in this mode are in general agreement with design values.\*

---

\*SPI, private communication.



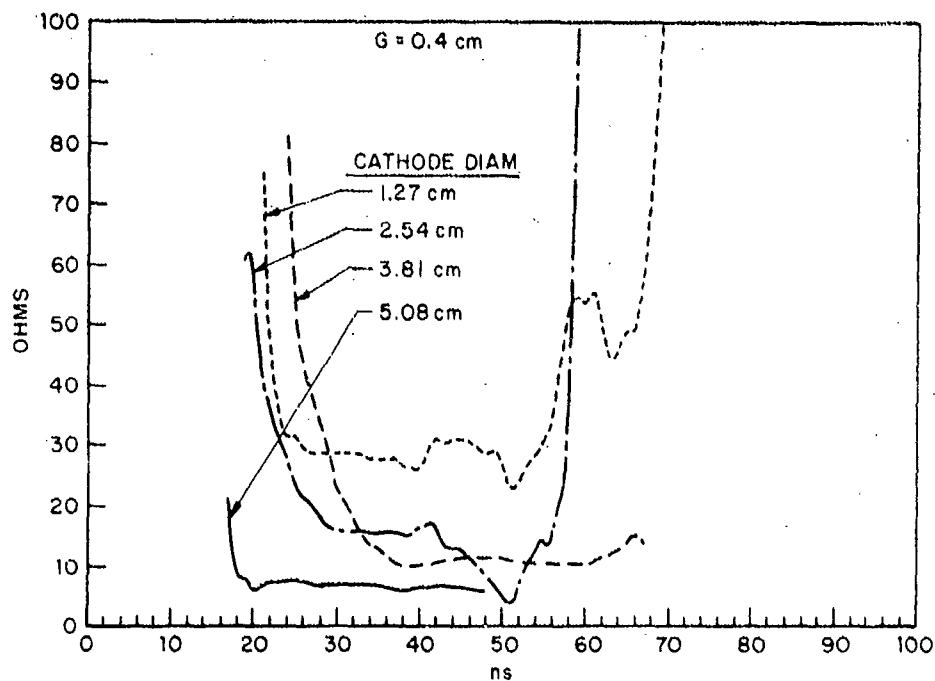


Figure 53. Impedance histories for  $G = 0.4$  cm low-impedance diodes.

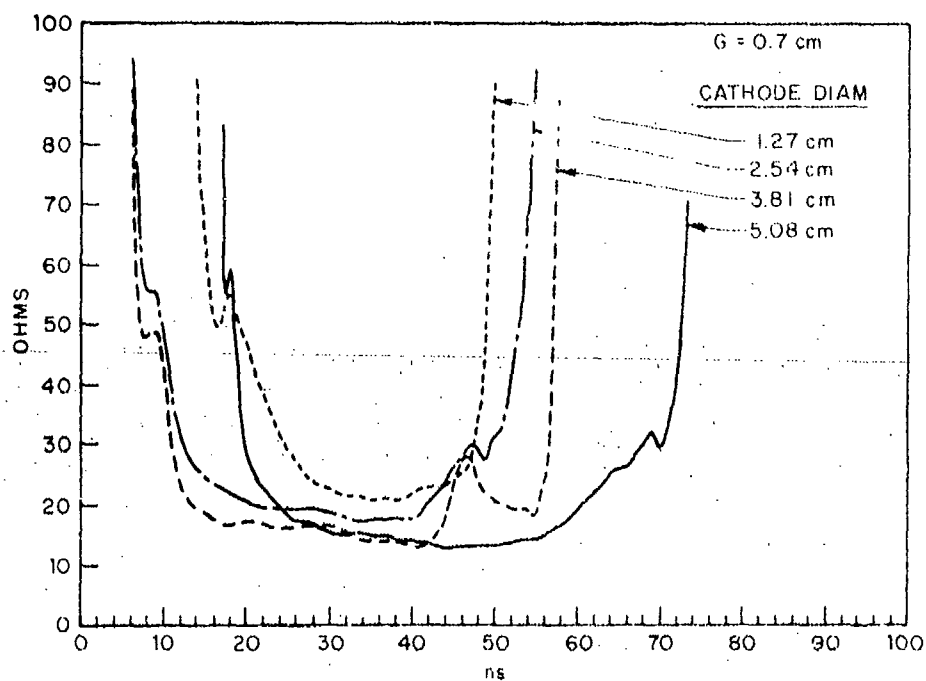


Figure 54. Impedance histories for  $G = 0.7$  cm low-impedance diodes.

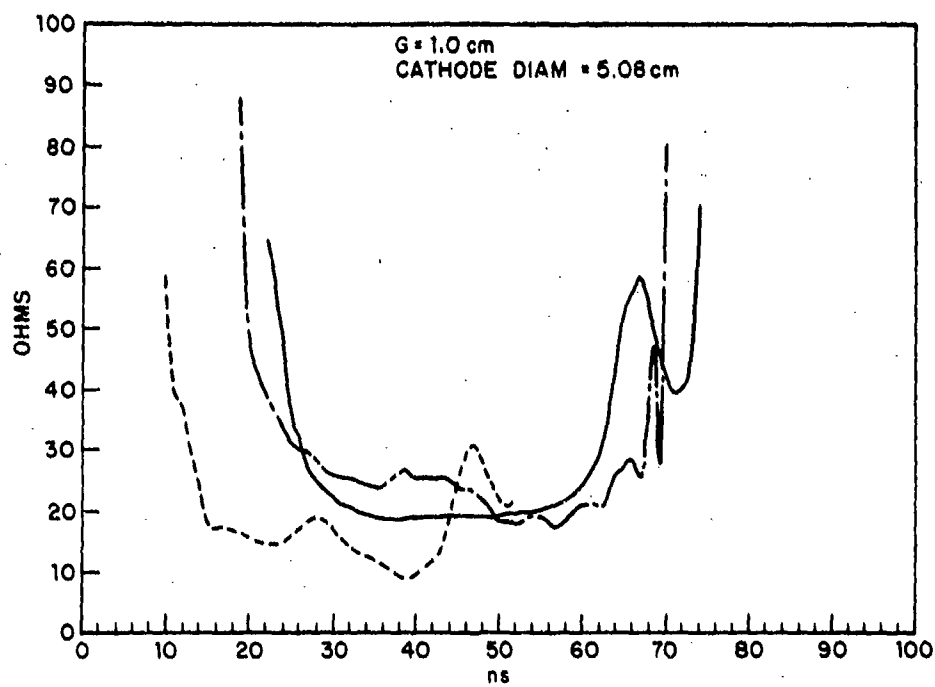


Figure 55. Impedance histories for  $G = 1.0$  cm low-impedance diode.

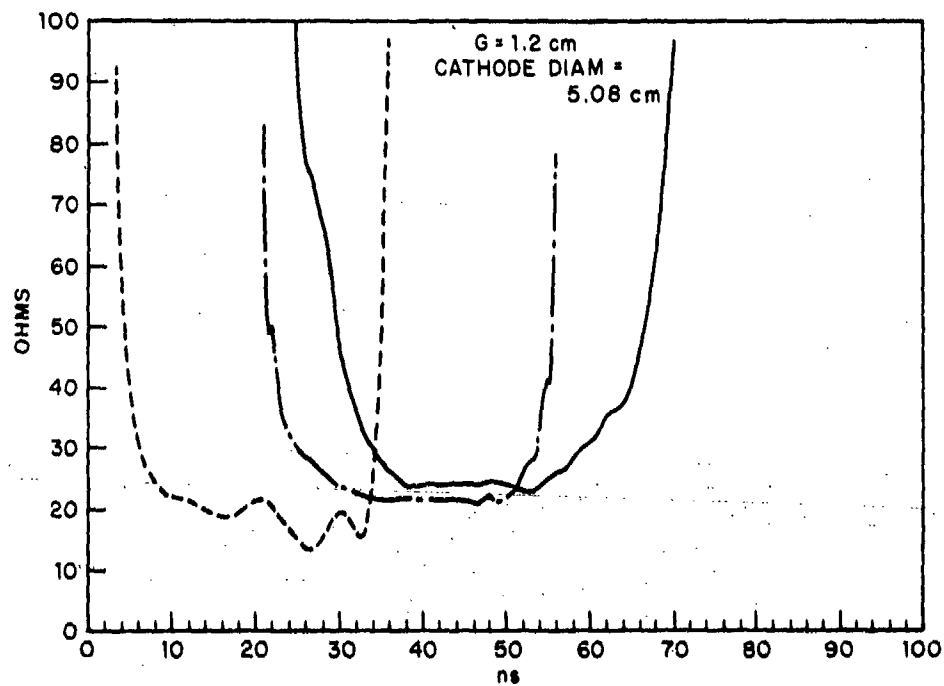


Figure 56. Impedance histories for  $G = 1.2$  cm low-impedance diode.

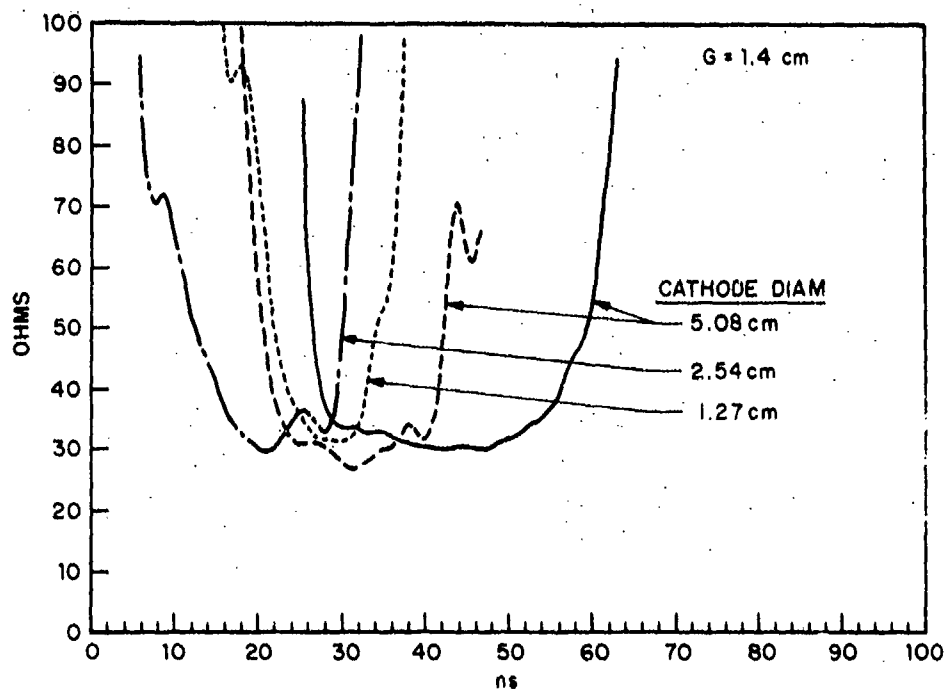


Figure 57. Impedance histories for  $G = 1.4$  cm low-impedance diodes.

#### 4.5 Electron Spectra

Electron spectra calculated for the high-impedance diodes using the modified EBSPEC program are shown in figures 58 through 62. Each of the spectra has at least two well-defined peaks, a broad one with a sharp drop at the spectrum cutoff energy and a low energy tail, and a narrower peak at a lower energy. These peaks correspond to the primary and secondary maxima in the V-monitor pulses (see figs. 20 through 24). As  $V_c$  increases, the energy of these peaks increases just as the voltage peaks do, but for the most part their shapes and relative areas remain unchanged.

TABLE V. LOW-IMPEDANCE VALUES FROM TIME HISTORIES  $V_c = 4.1$  MV

G (cm)	Diam (cm)	Z (ohms)	No. of traces
0.4	5.08	7	3
0.4	3.81	10	1
0.4	2.54	12	1
0.4	1.27	28	1
0.7	5.08	15	4
0.7	3.81	15	1
0.7	2.54	18	1
0.7	1.27	22	1
1.0	5.08	20	3
1.2	5.08	22	3
1.4	5.08	30	2
1.4	2.54	33	1
1.4	1.27	31	1

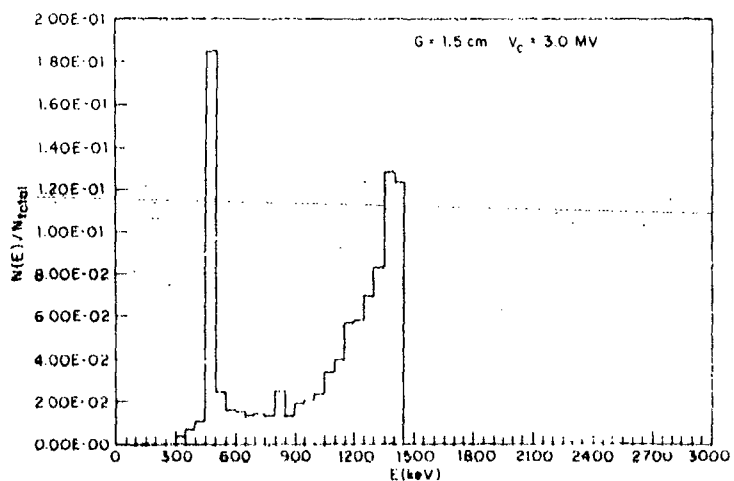
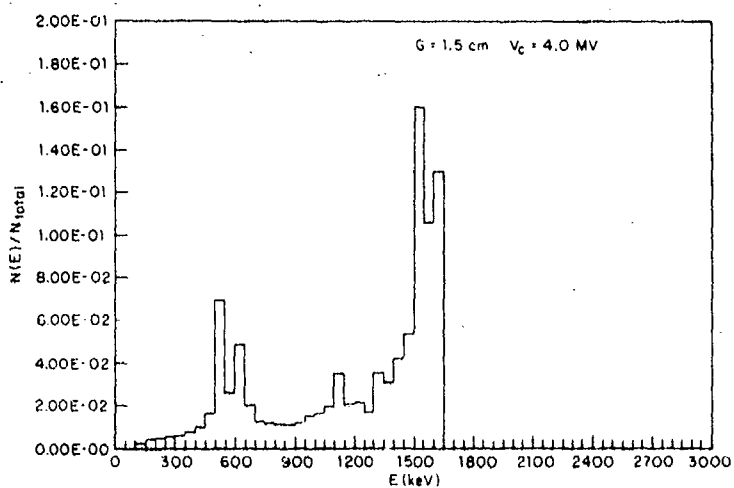
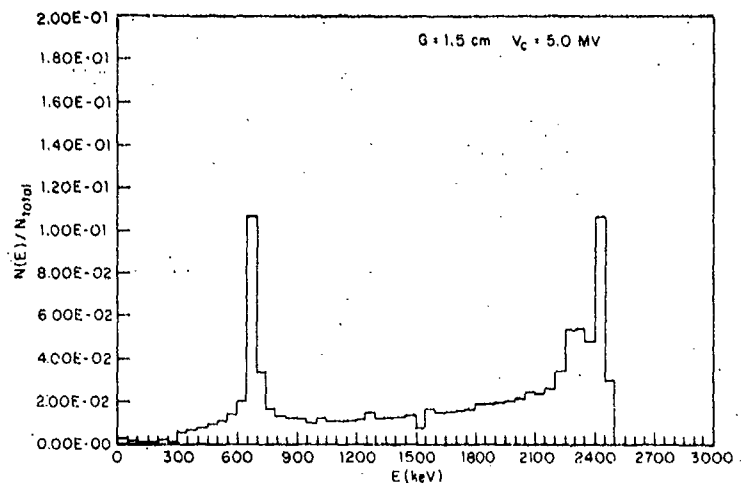


Figure 58. Electron energy spectra for  $G = 1.5 \text{ cm}$  hemi-plane diode.

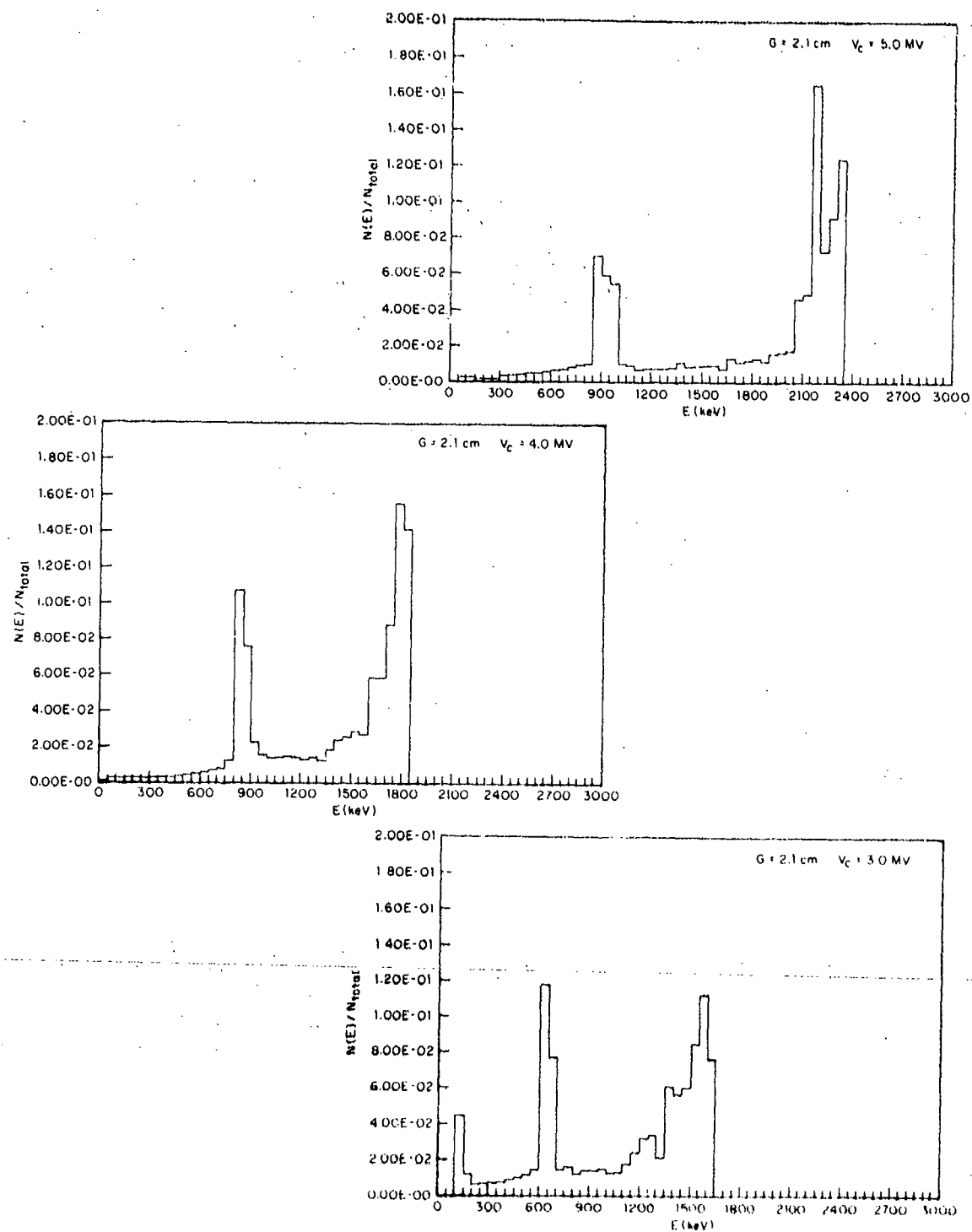


Figure 59. Electron energy spectra for  $G = 2.1$  cm hemi-plane diode.

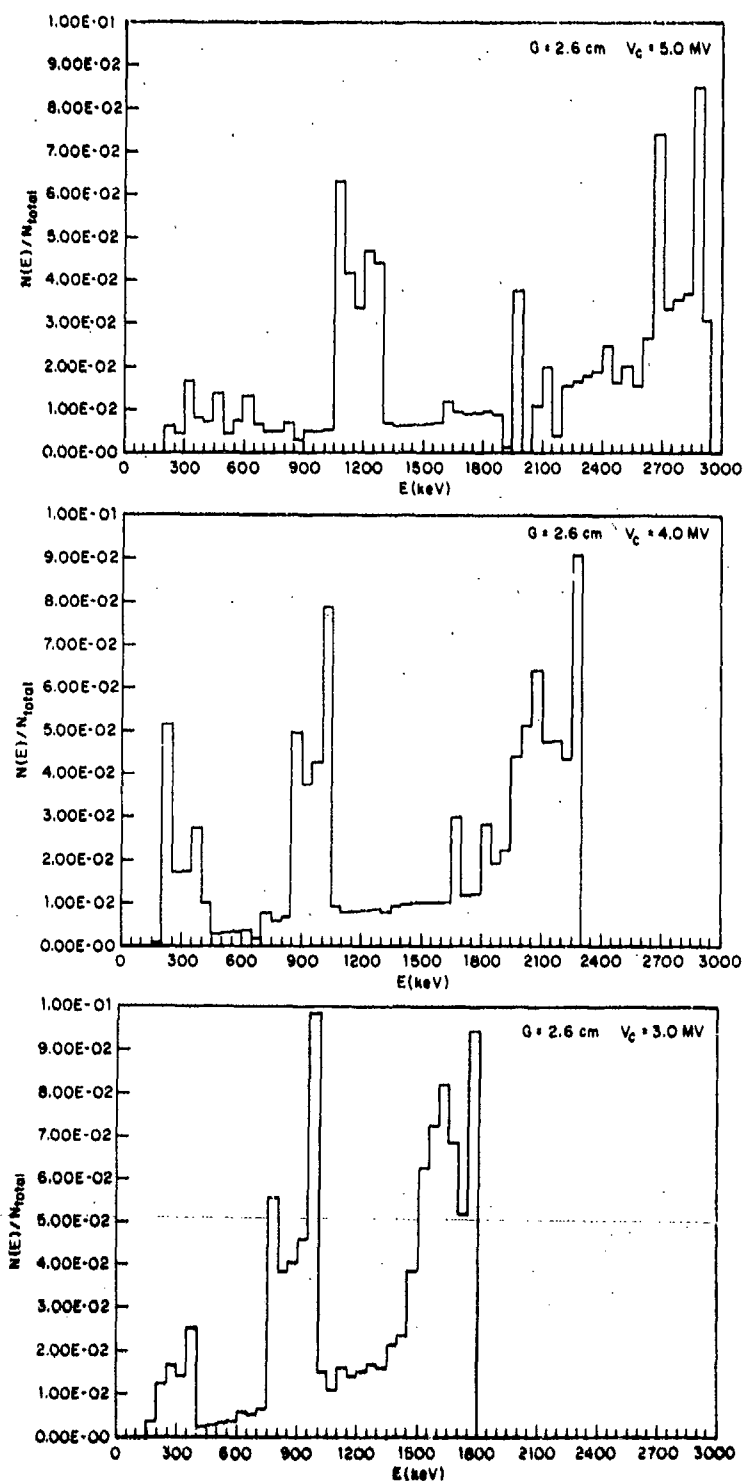


Figure 60. Electron energy spectra for  $G = 2.6$  cm hemi-plane diode.

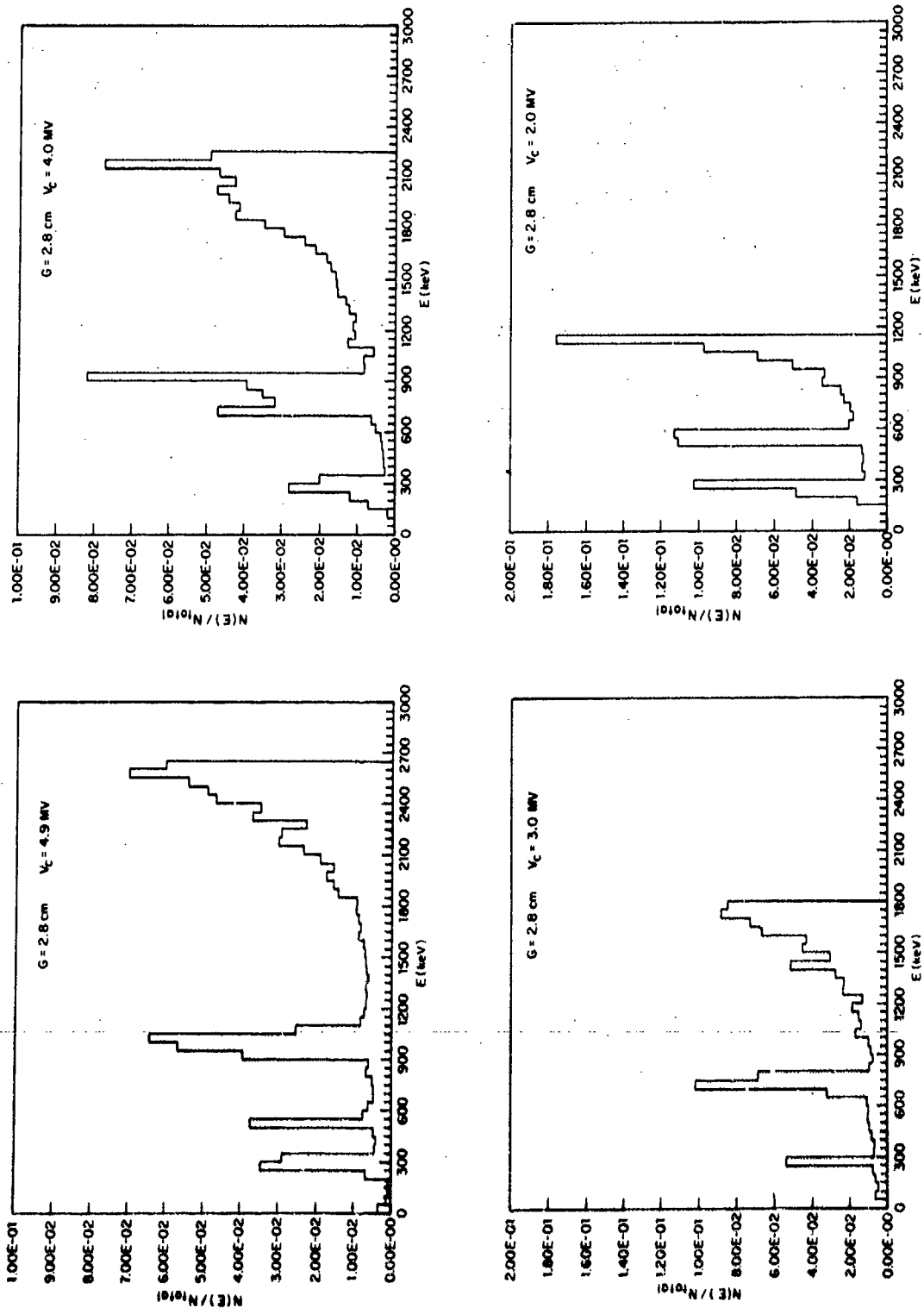


Figure 61. Electron energy spectra for  $G = 2.8$  cm hemi-plane diode.

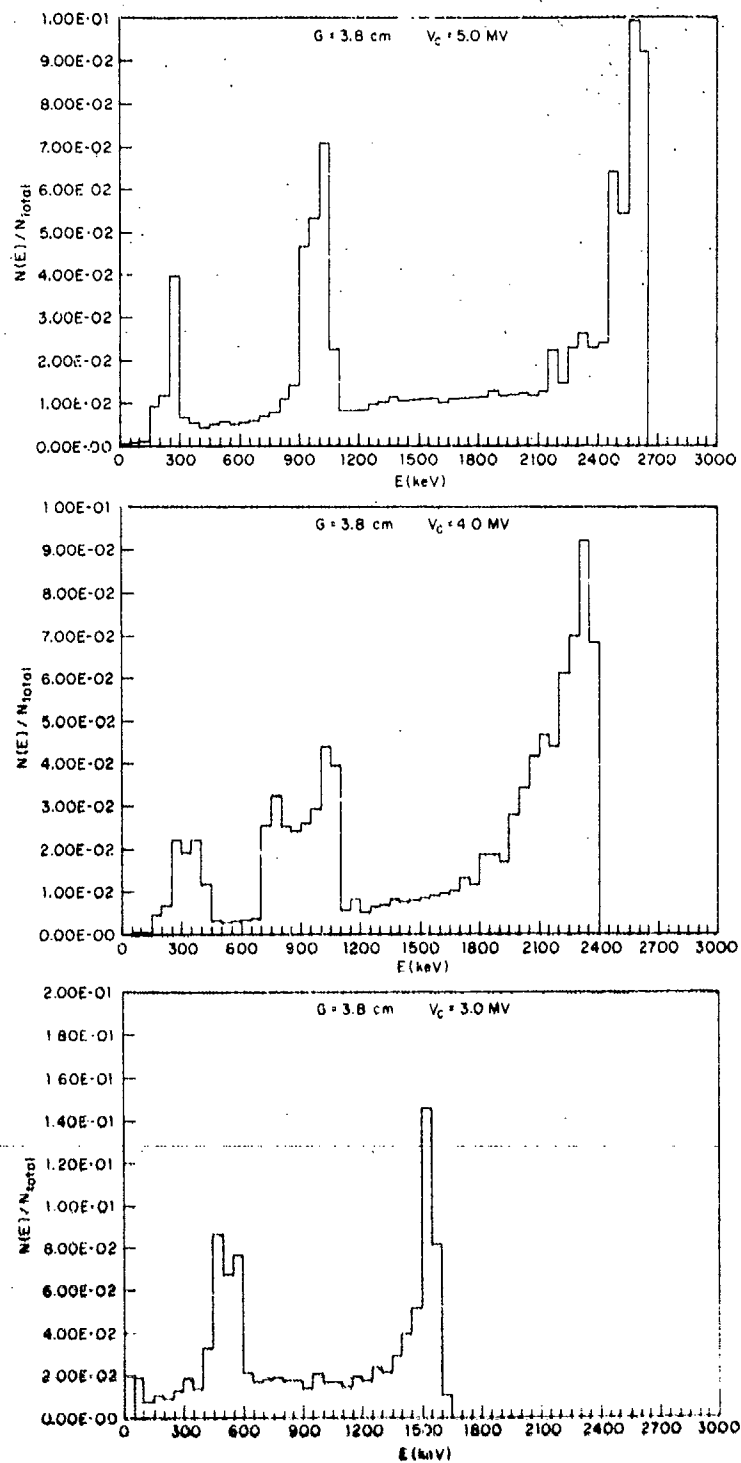


Figure 62. Electron energy spectra for  $G = 3.8$  cm hemi-plane diode.



These peaks often consist of two or more satellites. Some of the spectra also contain a third and lower energy peak. For the 2.8-cm diode, for example, such a peak appears in the spectra at all four charge voltages at practically the same energy. At the highest charge voltage,  $V_c = 4.9$  MV, a fourth peak appears, which might be a satellite of either the lowest energy peak or next higher energy peak.

Figure 63 shows high-impedance electron spectra of the HIFX beam measured by means of a magnetic spectrometer\* at  $V_c = 3.0, 4.1$ , and 5.0 MV. For those measurements, the cathode consisted of a 40-deg cone at the end of a 1.91-cm diam aluminum shank where  $G = 3.2$  cm. Thus, although the diode geometry for these measurements was not exactly the same as for the present high-impedance mode, one would expect not only close agreement between the peak energies but also similarities between the peak shapes of the magnetic spectra and those of the present measurements for  $G = 3.8$  cm in figure 62. Such agreement is found in the high energy peaks of the 4.0- and 4.1-MV spectra, as well as those of the 3.0-MV spectra, although in the latter the peak of the magnetic spectrum is broader. There is, however, an unexplained difference of about 300 keV between the energies of the peaks of the 5.0-MV spectra. The fact that the lower energy peaks do not appear in the magnetic spectra might be explained by the fact that whereas the spectrum calculated from I and V takes the entire beam into account, the magnetic spectrometer measures only the portion of the beam that is paraxial and may thus not measure the lower energy electrons, which can more easily be deflected off axis.<sup>2</sup>

\*S. E. Graybill and G. Ames, unpublished data on measurement of HDL FX-45 electron energy spectrum.

<sup>2</sup>S. E. Graybill, J. R. Uglum, W. H. McNeill, J. E. Rizzo, R. Lowell, and G. Ames, *Diagnostics and Applications of Pulsed Self-Focussed Relativistic Electron Beams*, Defense Atomic Support Agency Report 2477 (December 1969)

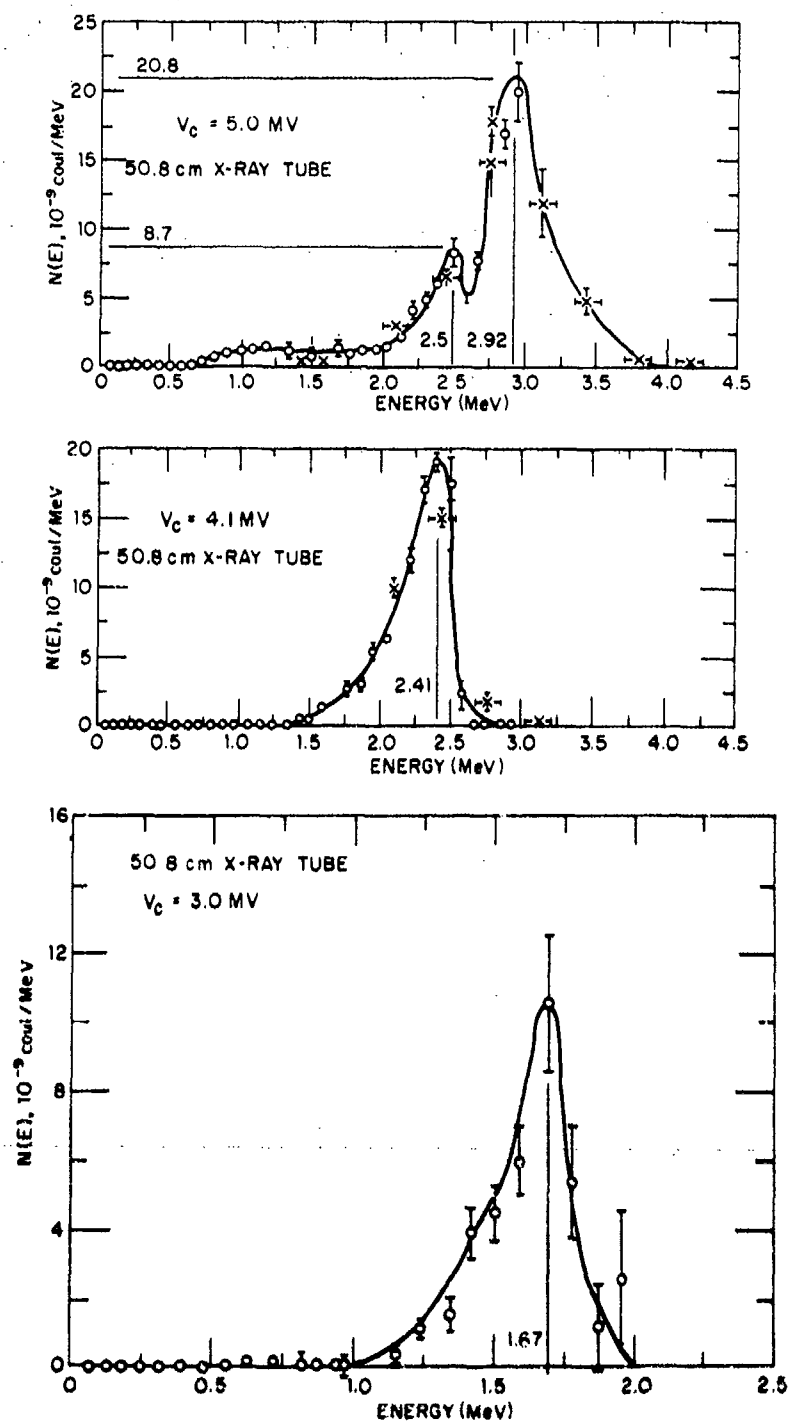


Figure 63. Electron energy spectra measured with magnetic spectrometer for  $G = 3.2 \text{ cm}$ , point-plane diode.

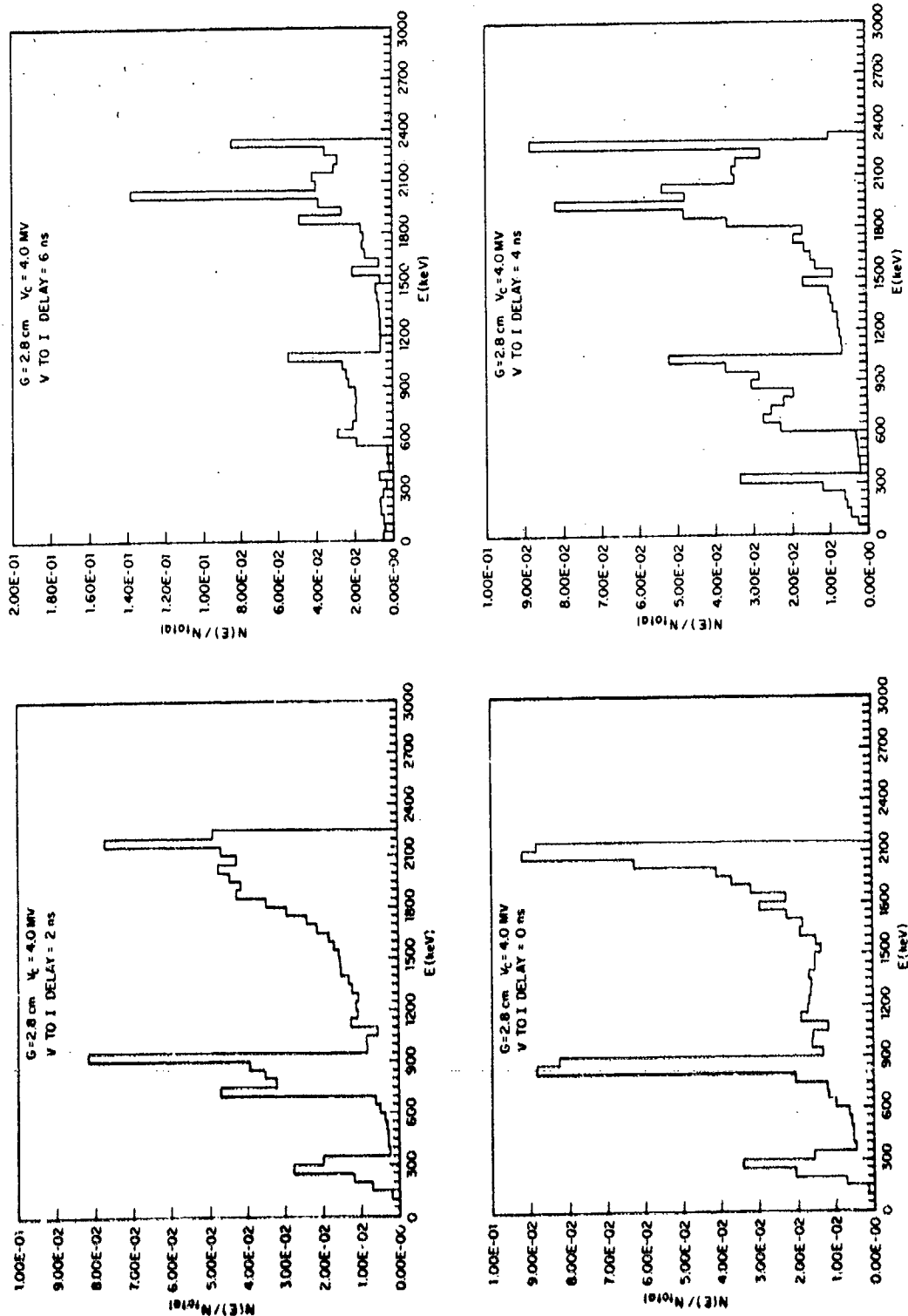


Figure 64. Electron energy spectra for  $G = 2.8 \text{ cm}$  hemi-plane diode for various delays of  $V$  relative to  $I$ .

In calculating the spectra of figures 58 through 62, the artificial delay applied between V and I pulses when pulse synchronization methods 1 and 2 were used (sect. 3.2) is the same as that used for the corresponding impedance time histories of figures 45 through 49. Figure 64 shows the effect on a spectrum of applying 0- to 6-nsec delays to V and I where  $G = 2.8$  cm and  $V_c = 4.0$  MV. The only effect is some changes in the detailed shape of the peaks, but their locations and relative intensities are essentially unchanged for the entire range of delay.

Sample electron spectra for the low-impedance diodes are shown in figures 65 through 69. In this case, most of the spectra have only one high energy peak at the cutoff electron energy. This absence of secondary peaks in the energy spectra corresponds to the near absence of a secondary maximum in the low-impedance V pulses, as noted in connection with figures 27 and 28. Also, as expected, for a given  $G$ , the peak energy increases with decreasing emitter diameter. The spectra in figures 67 and 68, where  $G = 1.0$  and  $1.2$  cm, are all for a 5.08-cm emitter diameter. These spectra illustrate how the detailed shape of the spectral peak may change from pulse to pulse. The 100-keV difference between the peak energy in one of the 1.0-cm spectra and that of the other two is quite anomalous, and could be due to a slight shift in the position of the emitter which went unnoticed.

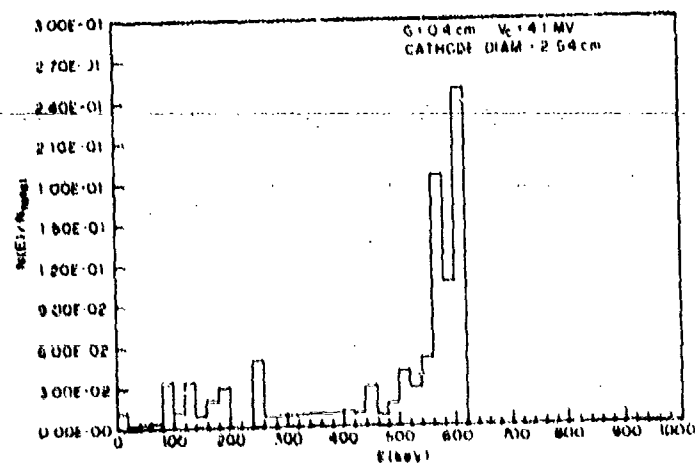
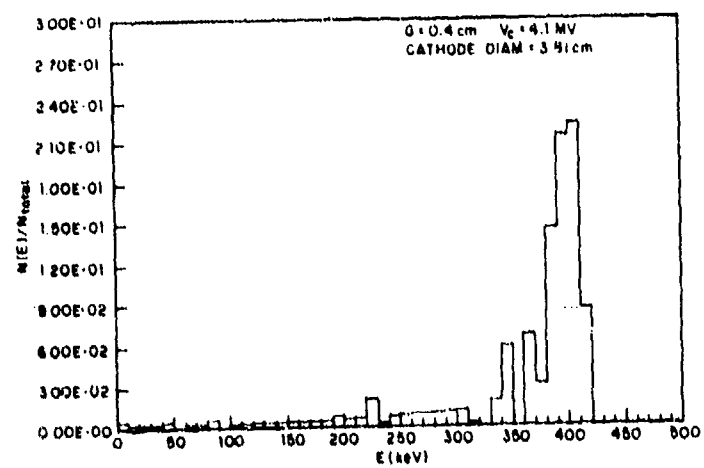
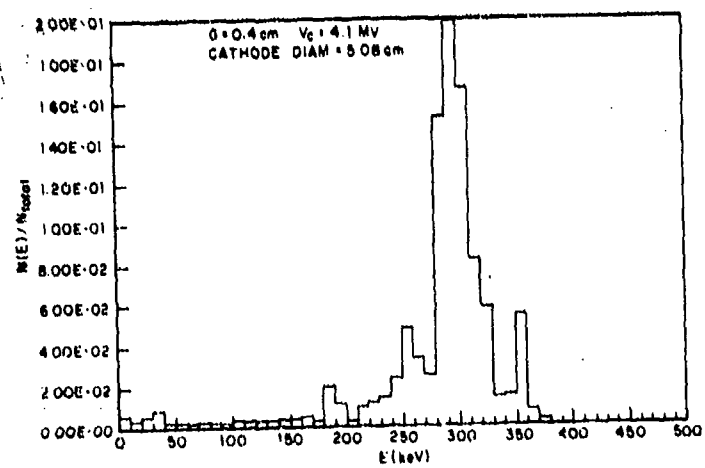


Figure 65. Electron energy spectra for  $G = 0.4 \text{ cm}$  low-impedance diodes.

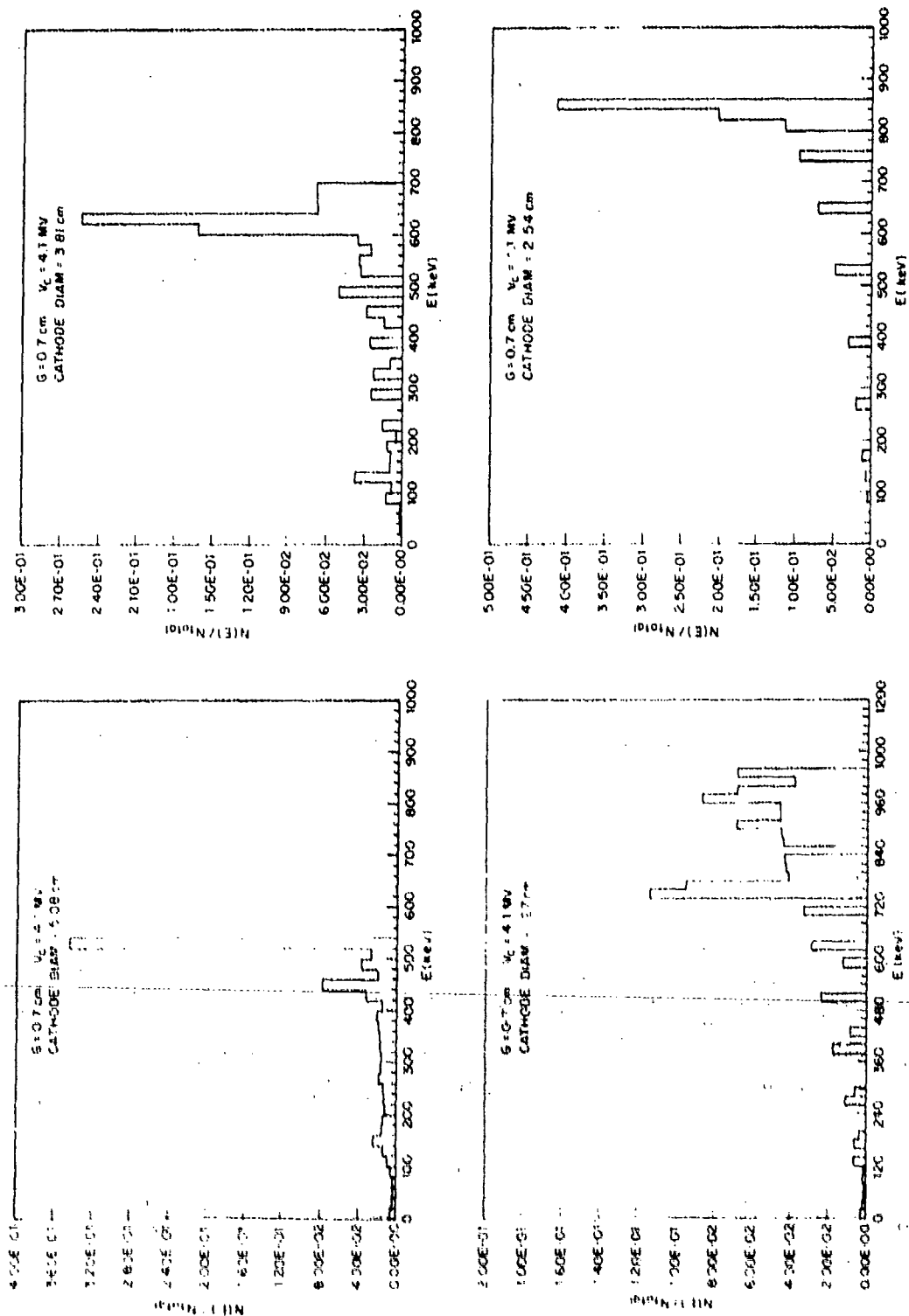


Figure 66. Electron energy spectra for  $G = 0.7$  cm low-impedance diodes.

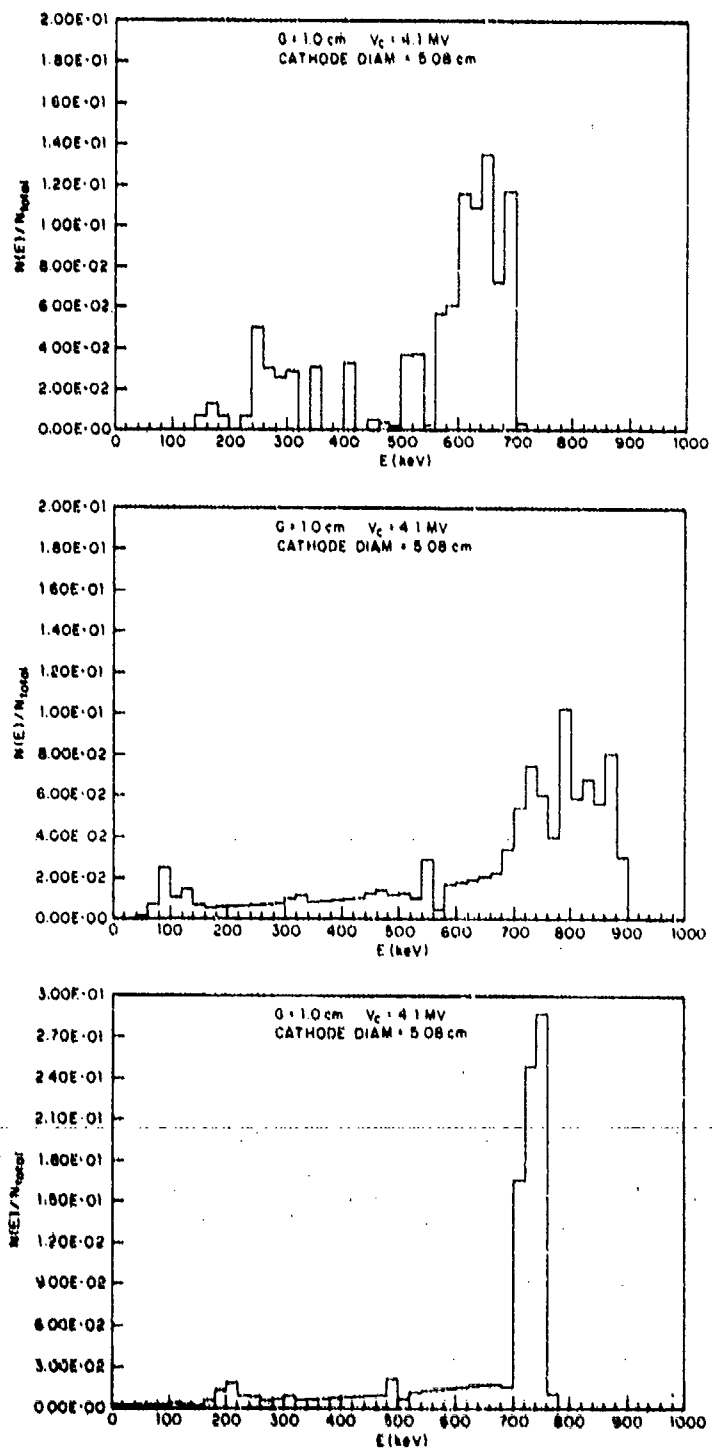


Figure 67. Electron energy spectra for  $G = 1.0$  cm low-impedance diode.

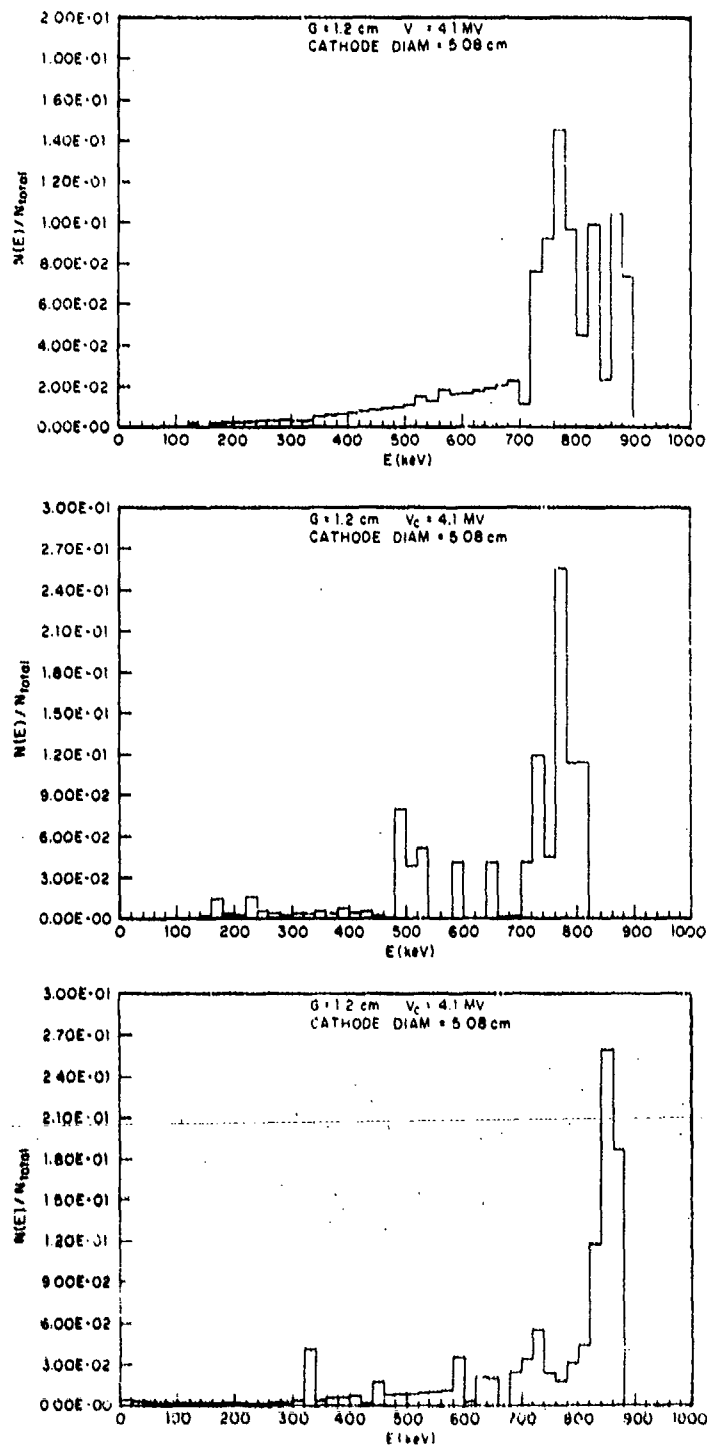


Figure 68. Electron energy spectra for  $G = 1.2$  cm low-impedance diode.



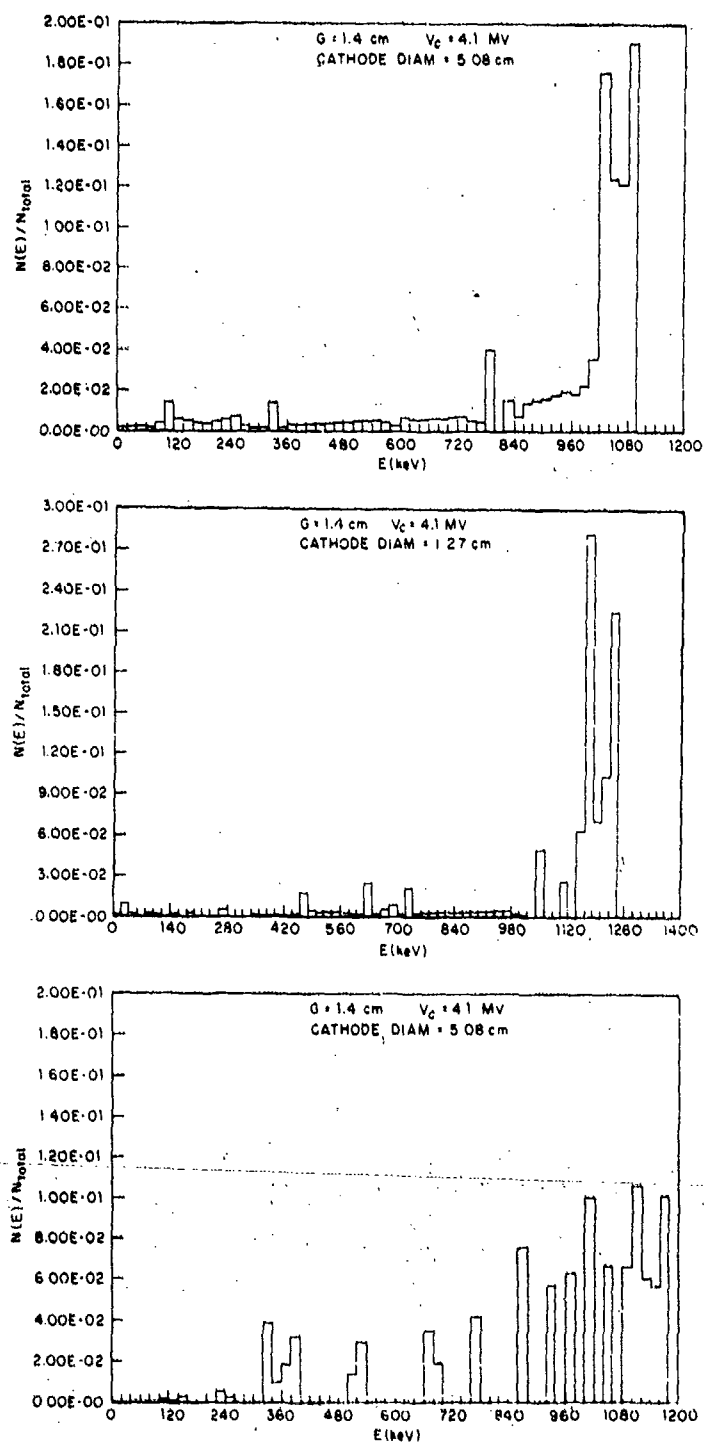


Figure 69. Electron energy spectra for G = 1.4 cm low-impedance diode.

#### 4.6 Gamma Dose Rate and Dose

The chief interest in the scintillator/photodiode measurements of  $\dot{R}$  and in TLD dose measurements in these studies is that they afford an indirect check on the validity of the measured V and I pulse shapes as well as on their time synchronizations. The check is based on the semiempirical formula<sup>1</sup>

$$\dot{R} = 0.00815 I(\text{kA}) V^{2.9}(\text{MV}) \quad \text{R/s} \quad (32)$$

for the dose rate 30.48 cm from the anode on axis. This formula is based on bremsstrahlung produced by constant-V, constant-I electron beams, such as those from Van de Graaff generators and linear accelerators. We assume that it also correctly predicts the instantaneous value of  $\dot{R}$  for beams from pulsed machines, such as HIFX. Furthermore, integration of equation (32) over the pulse should yield the total gamma dose. It is seen that both the  $\dot{R}$  pulse shape and the integrated dose predicted by equation (32) are sensitive to the individual I and V pulse shapes as well as to their correlation in time.

Figure 70 compares the observed gamma pulse shape with those predicted by equation 32 from the V- and I-monitor pulses. The V, I, and  $\dot{R}$  pulses were obtained from the diode with  $G = 2.8$  cm and  $V_c = 4.0$  MV (see fig. 22). As stated in section 3.2, there is about a 6-ns uncertainty in the synchronization of these pulses since their time bases were synchronized by method 1. The comparison between predicted and observed  $\dot{R}$  pulse shapes was therefore made for cases in which V is artificially delayed relative to I by 0, 2, 4, and 6 ns. The photodiode  $\dot{R}$  trace was normalized and shifted in time so that it coincides with the calculated trace at its peak value. Figure 70 shows that artificial

---

<sup>1</sup>F. J. Sazama and A. G. Stewart, *Design and Testing of a Current and Voltage Monitor for HIFX*, Harry Diamond Laboratories TR-1558 (August 1971).

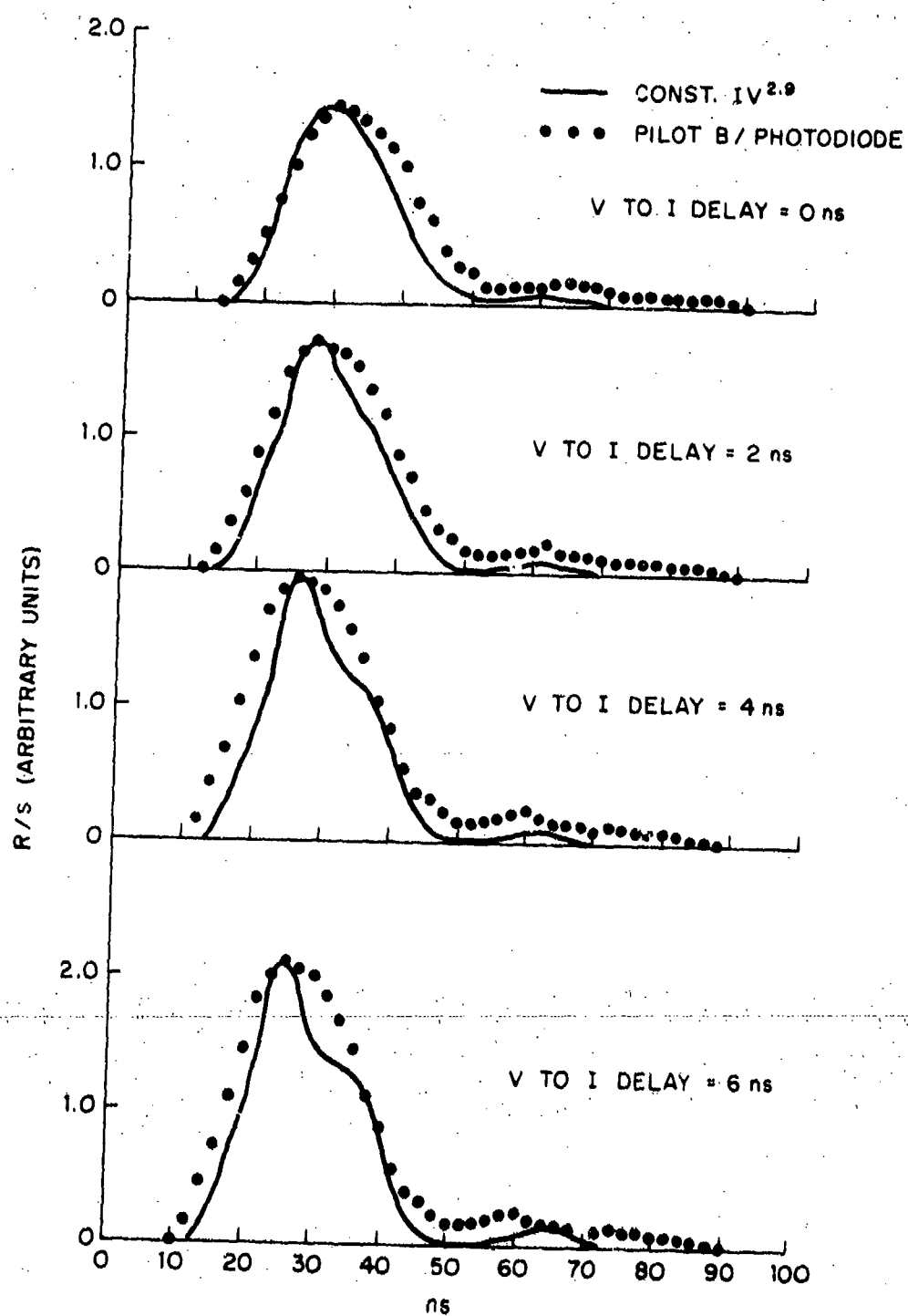


Figure 70. Measured and calculated gamma dose rate pulses.

V-to-I delays of 4 and 6 ns introduce distortions not present in the photodiode pulse, whereas delays 2 and 0 ns or less result in decay times shorter than that observed in the photodiode pulse. Thus, the optimum artificial V-to-I delay for this case, based on the R comparisons, is between 2 and 4 ns. This V-to-I delay compares reasonably well with that required to obtain the smoothest variation of impedance during the conduction period for this diode (sect. 4.3), which was 4 ns.

Table VI compares TLD dose measurements and those predicted by integrating equation (32) for the high-impedance pulses. The measured doses are, on the average, higher than the calculated ones by 70 percent. The calculated doses for each pair of V and I pulses increases monotonically by a maximum of 30 percent as the delay of V relative to I is increased from 0 to 6 ns. Therefore, most of the 70-percent discrepancy between measured and calculated dose must be due to systematic errors in measurements of the absolute value of V and/or I and/or dose. As is seen from equation (32), some relative error in the I-monitor calibration results in the same relative error in the calculated dose, whereas some relative error in the V-monitor calibration results in a relative error in the calculated dose 2.9 times as great. Thus, for example, decreasing the V and I monitor sensitivities,  $K_V$  and  $K_I$ , by 10 percent would increase the average calculated dose by about 40 percent.

TABLE VI. GAMMA DOSES AT 30.5 CM FROM HEMISPHERE-PLANE DIODES

G (cm)	V <sub>c</sub> (MV)	Y at 30.5 cm Theory (R)	Y at 30.5 cm Measured (R)
1.5	3.0	8	14
1.5	4.0	19	36
1.5	5.0	71	75
2.1	3.0	10	19
2.1	4.0	24	44
2.1	5.0	67	124
2.6	3.0	11	16
2.6	4.0	31	50
2.6	5.0	39	133
2.7	3.0	8	15
2.8	3.0	11	19
2.8	4.0	30	52
2.8	4.9	75	140
3.8	3.0	8	16
3.8	4.0	43	64
3.8	5.0	78	148
5.6	3.0	10	11

The calibration of the  $\text{CaF}_2\text{:Mn}$  TLD's, performed with doses of the order of 10 R, is known to be valid for doses many orders of magnitude higher.<sup>6</sup> In the case of the V and I measurements, however, it is conceivable that systematic errors might have arisen in extrapolating the calibrations performed with pulses in the kilovolt and 10-ampere ranges over three orders of magnitude to the megavolt and 10-kiloampere regions. On the other hand, the agreement noted in section 4.5 between calculated electron spectra and those measured with a magnetic spectrometer imply the general validity of the V-monitor calibrations in the megavolt region. A further check on the V-monitor calibration might be made using other techniques, such as measuring the value of V at which the onset of a gamma-induced nuclear reaction takes place having a known threshold in the megavolt region.<sup>2</sup> Checks on the validity of the I-monitor calibration could be made by measuring the total charge in a suitably designed Faraday Cup.<sup>5</sup> Finally, another independent measurement which would afford a check on both V and I weighted equally, as well as their time correlation, would be that of the energy deposited in a calorimeter.<sup>2,5</sup>

## 5. CONCLUSIONS

The V and I monitors described here have been shown to be extremely convenient and yield reliable measurements in HIFX FE diodes. Although their calibrations generally remain constant to within a few percent

---

<sup>2</sup>S. E. Graybill, J. R. Uglum, W. H. McNeill, J. E. Rizzo, R. Lowell, and G. Ames, *Diagnostics and Applications of Pulsed Self-Focussed Relativistic Electron Beams*, Defense Atomic Support Agency Report 2477 (December 1969).

<sup>5</sup>G. Yonas and P. Spence, *Experimental Investigations of High v/y Electron Beam Transport*, Physics International FR-106 (1968).

<sup>6</sup>J. H. Schulman, F. H. Attix, E. J. West, and R. J. Ginther, *New Thermoluminescent Dosimeter*, Rev. Sci. Instrum. 31 (1960), 1263.

over a period of months, they warrant periodic checks. These checks are necessary in the case of the SPI-built V monitor, because of possible tensile changes in the thin-film capacitor,  $C_1$ , and, in the case of the I monitors, because of abrupt changes in  $R_p$  that might have been caused by an unusually large current pulse, such as that resulting from a shorted diode. The off-line pulse calibration techniques described for the monitors are simple to perform, although they require proper impedance-matching hardware to obtain unambiguous results. Such hardware is not needed, however, in the in-place pulse technique for the V monitor. Once the calibration of the monitors has been established, their calibrations at later times may be checked and corrected, if necessary, by making bridge measurements of  $C_2$ ,  $R_x$ , and  $R_p$  and using equations (1) and (2). These measurements may, of course, be performed with the monitors mounted on the machine.

It has been shown that the V and I monitors yield pulses containing much electrical information relevant to the dynamic properties of the diode through impedance versus time, time relationship of V and I, and number and amplitude of secondary V and I maxima. In addition, the V and I monitors may be used in the same way for both the high- and low-impedance modes of the machine, even though these modes involve greatly different diode configurations. This versatility of the monitors greatly simplifies the task of investigating other diode configurations proposed to further reduce the impedance and make possible the production of more intense electron beams and greater doses in materials of interest.



#### LITERATURE CITED

- (1) F. J. Sazama and A. G. Stewart, Design and Testing of a Current and Voltage Monitor for HIFX, Harry Diamond Laboratories TR-1558 (August 1971).
- (2) S. E. Graybill, J. R. Uglum, W. H. McNeill, J. E. Rizzo, R. Lowell, and G. Ames, Diagnostics and Applications of Pulsed Self-Focussed Relativistic Electron Beams, Defense Atomic Support Agency Report 2477 (December 1969).
- (3) Program EBSPEC, Simulation Physics Corp. TR-71-05 (August 1971).
- (4) T. H. Martin, K. R. Prestwich, and D. L. Johnson, Summary of the Hermes Flash X-Ray Program, Sandia Laboratories Report SC-RS-69-421 (October 1969).
- (5) G. Yonas and P. Spence, Experimental Investigations of High  $v/\gamma$  Electron Beam Transport, Physics International FR-106 (1968).
- (6) J. H. Schulman, F. H. Attix, E. J. West, and R. J. Ginther, New Thermoluminescent Dosimeter, Rev. Sci. Instrum. 31 (1960), 1263.

APPENDIX A.--VOLTAGE AND CURRENT MONITORS:  
THEORIES OF OPERATION AND SENSITIVITY

	<u>Page</u>
A-1 DESCRIPTION AND THEORY OF MONITORS . . . . .	97
A-1.1 Voltage (V) Monitors . . . . .	97
A-1.2 Current (I) Monitors . . . . .	99
A-2 APPROXIMATION FOR SENSITIVITY OF HDL-BUILT V MONITOR . . . . .	100

FIGURES

A-1 Voltage monitor circuit . . . . .	97
A-2 Current monitor circuit . . . . .	99
A-3 Volumes $v_1$ and $v_2$ . . . . .	102
A-4 Plots of functions $F(\rho)$ and $G(\rho)$ . . . . .	105



APPENDIX A.--VOLTAGE AND CURRENT MONITORS:  
THEORIES OF OPERATION AND SENSITIVITY

A-1 DESCRIPTION AND THEORY OF MONITORS

A-1.1 Voltage (V) Monitors

Both the HDL-built and SPI-built V monitors are of the capacitor divider type, whose equivalent circuit is illustrated in figure A-1.  $C_1$  is a small capacitance, of the order of a picofarad, formed by the field emission (FE) tube cathode shank and a metallic plate near the inner wall of the FE-tube extension.  $C_2$  is a capacitance, a few thousand times as large as  $C_1$ , formed by the metallic plate and FE-tube extension wall separated by a thin Mylar dielectric. The entire radiation pulse voltage appears across  $C_1$  and  $C_2$  in series, and the voltage across  $C_2$  is impressed across the voltage divider formed by a resistor  $R_x$  in series with the 50-ohm termination,  $R_{term}$ , of the signal cable. The signal across the termination is applied directly to the input of an oscilloscope.

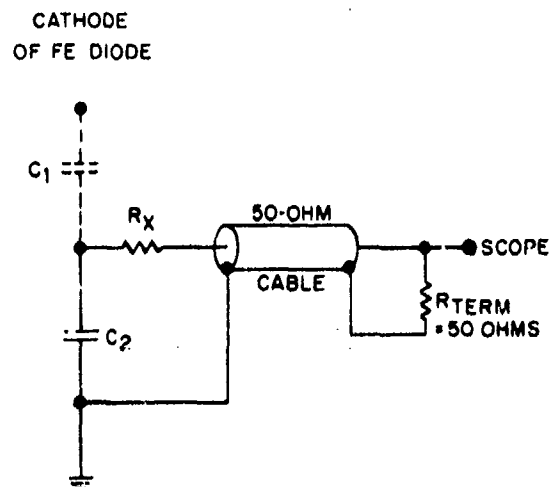


Figure A-1. Voltage monitor circuit.

The response of the voltage monitor to a step voltage  $V_{step}$  is

$$V_{out}(t) = V_{step} \left( \frac{C_1}{C_1 + C_2} \right) \left( \frac{R_{term}}{R_{term} + R_x} \right) \exp \left[ \frac{-t}{(R_{term} + R_x)(C_1 + C_2)} \right], \quad (A-1.)$$

## APPENDIX A

where  $t$  is time. The decay time constant,  $\tau$ , of the circuit is thus

$$\tau = (R_{\text{term}} + R_x)(C_1 + C_2) \quad (\text{A-2})$$

The sensitivity of the V monitor ( $K_V$ ) to the step pulse, or for that matter, any input voltage  $V_{\text{in}}$ , at early times  $t$  such that

$$t \gg \tau = (R_{\text{term}} + R_x)(C_1 + C_2) \quad (\text{A-3})$$

is seen from equation (A-1) to be

$$K_V = \frac{V_{\text{out}}}{V_{\text{in}}} = \left( \frac{C_1}{C_1 + C_2} \right) \left( \frac{R_{\text{term}}}{R_{\text{term}} + R_x} \right) \text{volts per volt} . \quad (\text{A-4})$$

Since for these voltage monitors,  $t$  is of the order of a microsecond and the HIFX pulse width is about 25 ns, the  $K_V$  of equation (A-4) is directly applicable. In principle, then, a measurement of  $C_1$ ,  $C_2$ , and  $R_x$  at the time the V monitor is actually being used yields the calibration through equation (A-4). However, because of its small value,  $C_1$  cannot be measured directly with a capacitance bridge so that  $K_V$  cannot be calculated from equation (A-4). It is therefore necessary to measure  $K_V$ . This is done by impressing known pulses on the monitor and measuring the output (described in sect. 2 of the main body of the report). If at the time of the pulse calibration, the circuit parameters have values  $\bar{R}_x$ ,  $\bar{C}_1$ , and  $\bar{C}_2$ , then at any other time at which the values change to  $R_x$ ,  $C_1$ , and  $C_2$ ,  $K_V$  is (in view of equation (A-4))

$$K_V = \bar{K}_V \left( \frac{C_1}{\bar{C}_1} \right) \left( \frac{\bar{C}_2}{C_2} \right) \left( \frac{\bar{R}_x + 50}{R_x + 50} \right). \quad (\text{A-5})$$

Here  $\bar{K}_V$  is the sensitivity measured directly from the known pulses and the approximation  $C_1 \ll C_2$  has been used in equation (A-4).

## APPENDIX A

### A-1.2 Current (I) Monitors

The equivalent circuit for both the HDL-built and the SPI-built I monitors is shown in figure A-2.  $R_p$  is a small resistance (about 10 milliohms) made up of a large number of resistors, each of which is soldered to two parallel copper strips. These strips are then clamped to two metallic rings that are electrically insulated from each other by means of a lucite or other

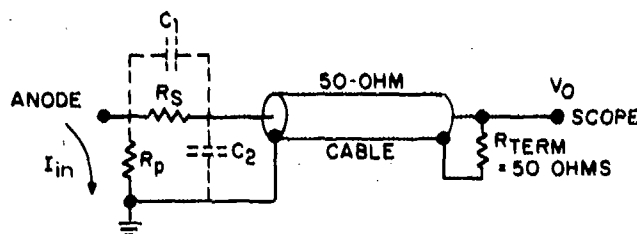


Figure A-2. Current monitor circuit showing stray capacitances  $C_1$  and  $C_2$ .

dielectric spacer. One of the rings makes electrical contact with the exit end of the FE tube extension, which is at ground potential, and the other makes electrical contact with the anode plate. Thus, if all the electrons in the beam are stopped in the anode plate, all the beam current passes through  $R_p$  on its way to ground. The voltage across  $R_p$  appears across the resistive voltage divider formed by  $R_s$  in series with the 50-ohm termination,  $R_{term}$ , of the signal cable.  $C_1$  and  $C_2$  are stray capacitances across  $R_s$  and the 50-ohm cable.

As discussed by Sazama and Stewart,<sup>1</sup>  $C_1$ ,  $C_2$ ,  $R_s$ , and  $R_{term}$  form a compensated attenuator, which, when balanced, will transmit an ideal step of voltage,  $V_O$ , for an ideal step of current,  $I_{in}$ . The current sensitivity ( $K_I$ ) would then be

$$K_I = \frac{V_O}{I_{in}} = \frac{R_{term}}{R_s + R_{term}} R_p \text{ V/kA} \quad (\text{A-6})$$

where  $R_p$  is in milliohms.

<sup>1</sup>F. J. Sazama and A. G. Stewart, *Design and Testing of a Current and Voltage Monitor for HIFX*, Harry Diamond Laboratories TR-1558 (August 1971).

## APPENDIX A

For both the HDL-built and SPI-built I monitors, balance is obtained by using a copper strip or wire for  $R_s$ , making  $R_s = 0$ .

Under these conditions, equation (A-6) becomes

$$K_I = \frac{V_o}{I_{in}} = R_p V/kA \quad (A-7)$$

Since  $K_I$  as measured by pulse techniques does not, in general, agree with  $R_p$  as measured with a bridge, a normalization corresponding to that in equation (A-5) for the V-monitor calibration is employed for the I-monitor calibration:

$$K_I = \bar{K}_I \left( \frac{R_p}{\bar{R}_p} \right) V/kA \quad (A-8)$$

The barred and unbarred notation in equation (A-8) corresponds to that used in equation (A-5).

### A-2 APPROXIMATION FOR SENSITIVITY OF HDL-BUILT V MONITOR

With the approximation  $C_1 \ll C_2$ , equation (A-4) for the V-monitor sensitivity becomes

$$K_V = \left( \frac{C_1}{C_2} \right) \left( \frac{R_{cable}}{R_{cable} + R_x} \right) \quad (A-9)$$

For the HDL-built V monitor, the calibration data\* have been normalized to  $R_x = 485$  ohms,  $R_{cable} = 50$  ohms, and  $C_2 = 2000$  pF. Substituting these values into equation (A-9) yields

$$K_V = 46.7 C_1 V/MV \quad (A-10)$$

\*See figure 8 of the main body of the report.

# APPENDIX A

with  $C_1$  expressed in picofarads. The outer plate making up  $C_1$  fits into an opening in the wall of the field emission (FE) tube extension. This opening was made by drilling a hole of radius  $R = 8.89$  cm radially into the wall of the extension. It is thus reasonable to express  $C_1$  as

$$C_1 = (2R)\alpha C_{\text{coax}} \quad (\text{A-11})$$

where  $C_{\text{coax}}$  is the appropriate coaxial capacitance calculated from

$$C_{\text{coax}} = \frac{55.54}{\ln \frac{D}{d}} \text{ pF/m} \quad (\text{A-12})$$

where

$D$  = FE tube extension i.d. and

$d$  = FE tube shank diameter; and

$\alpha$  is the ratio of two volumes:

$$\alpha = \frac{v_1}{v_2} \quad (\text{A-13})$$

The volumes  $v_1$  and  $v_2$  are each represented by the shaded portions of a set of three orthogonal views in figure A-3. In this figure,  $R_2$ ,  $R_1$ , and  $R$  are respectively the radii of the FE tube extension, cathode shank, and hole in the wall of the FE tube extension. Illustrated in the lower set of views,  $v_2$  is simply the volume bounded by two concentric cylinders of radii  $R_1$  and  $R_2$ , each of height  $2R$ . Thus

$$v_2 = 2\pi R_2^2 - R_1^2 R \quad (\text{A-14})$$

The upper set of views illustrates the same two concentric cylinders with a curve,  $m$ , on the wall of the outer cylinder formed by its intersection with a cylinder of radius  $R$  at right angles to it. Volume  $v_1$  is then the portion of the volume bounded by the inner and outer cylinders and the surface generated by the radii which cut the outer cylinder along  $m$ .

APPENDIX A

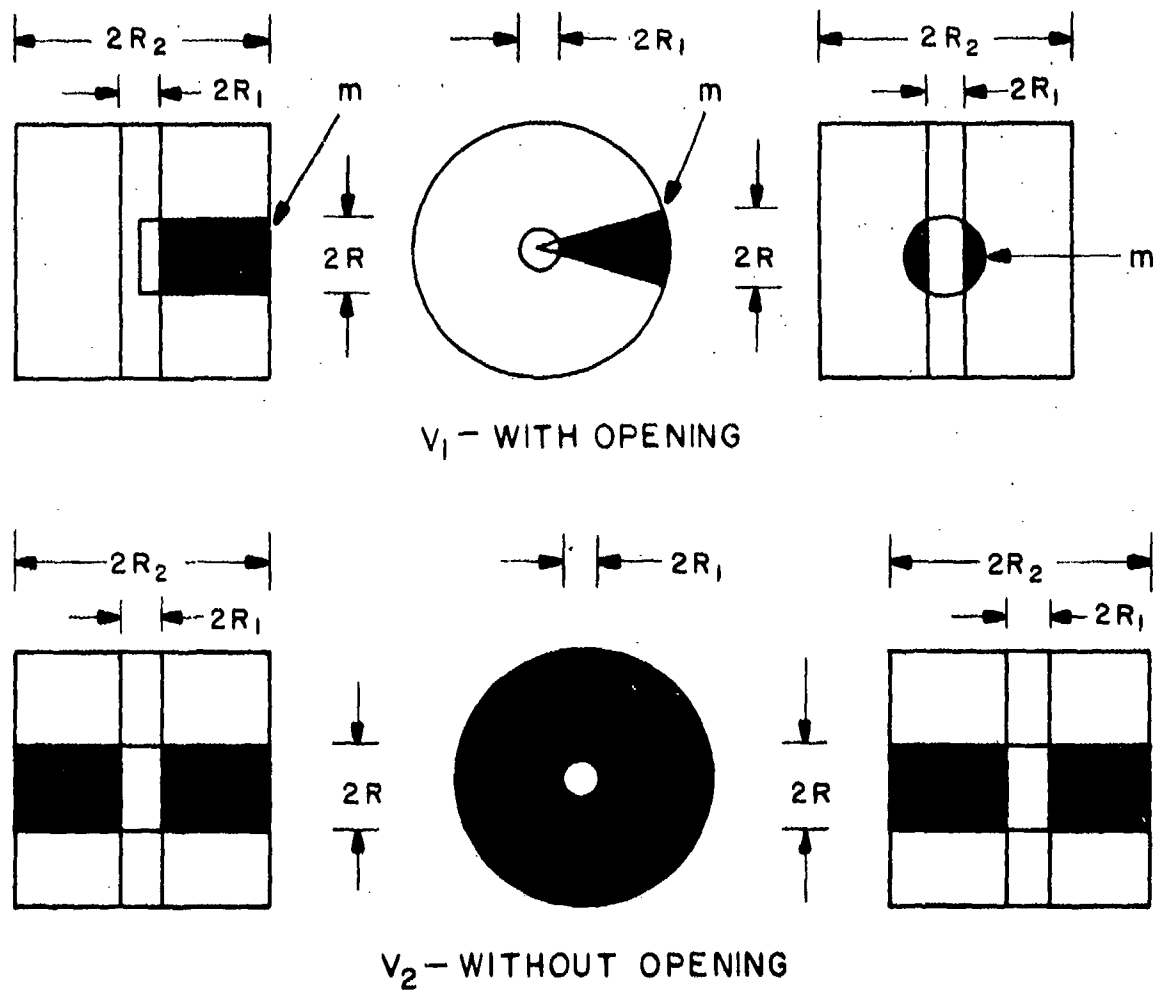


Figure A-3. Volumes  $v_1$  and  $v_2$ .

Consider a cylindrical coordinate system whose  $z$  axis coincides with that of the FE tube, and whose origin is at the intersection of that  $z$  axis with the axis of the cylindrical hole cut in the wall of the FE tube. In terms of the  $z$  and  $\theta$  coordinates of this system, the equation of the curve  $m$  is

$$\sin\theta = \left( \frac{R^2 - z^2}{R_2^2} \right)^{1/2} \quad (A-15)$$

# APPENDIX A

The volume  $v_1$  is then calculated from

$$v_1 = 4 \int_{R_1}^{R_2} r dr \int_0^R dz \int_0^{\theta(z)} d\theta, \quad (\text{A-16})$$

where  $r$  is the radial coordinate of the cylindrical system described above.

Substituting (A-15) into (A-16) and evaluating the radial and angular integrals then yields

$$v_1 = 2 \left( R_2^2 - R_1^2 \right) R F(\rho), \quad (\text{A-17})$$

where

$$F(\rho) = \int_0^1 \sin^{-1} \left( \frac{1 - \chi^2}{\rho^2} \right)^{1/2} d\chi \quad (\text{A-18})$$

with

$$\rho = \frac{R_2}{R} > 1. \quad (\text{A-19})$$

An integral closely related to  $F(\rho)$  yields the radiation dose,  $N$ , on a disc of radius  $R$  a distance  $d$  from a line source of uniform strength  $\lambda$  per unit length. The solution is

$$N = \frac{2\lambda R}{\pi} G(\rho), \quad (\text{A-20})$$

where

$$G(\rho) = \int_0^1 \tan^{-1} \left( \frac{1 - \chi^2}{\rho^2} \right)^{1/2} d\chi \quad (\text{A-21})$$

with

$$\rho = \frac{d}{R}. \quad (\text{A-22})$$

## APPENDIX A

Both  $F(\rho)$  and  $G(\rho)$  are plotted in figure (A-4). The final expression for  $C$ , given by equation (A-11), may now be written by combining equations (A-12), (A-13), (A-14) and (A-17). The result is

$$C_1 = \frac{2RF(\rho)}{\pi} \cdot \frac{16.93}{\ln \frac{R_2}{R_1}} \frac{1}{12} \text{ pF} . \quad (\text{A-23})$$

With the values

$$R = 4.45 \text{ cm},$$

$$R_2 = 12.7 \text{ cm, and}$$

$$R_1 = 1.588 \text{ cm},$$

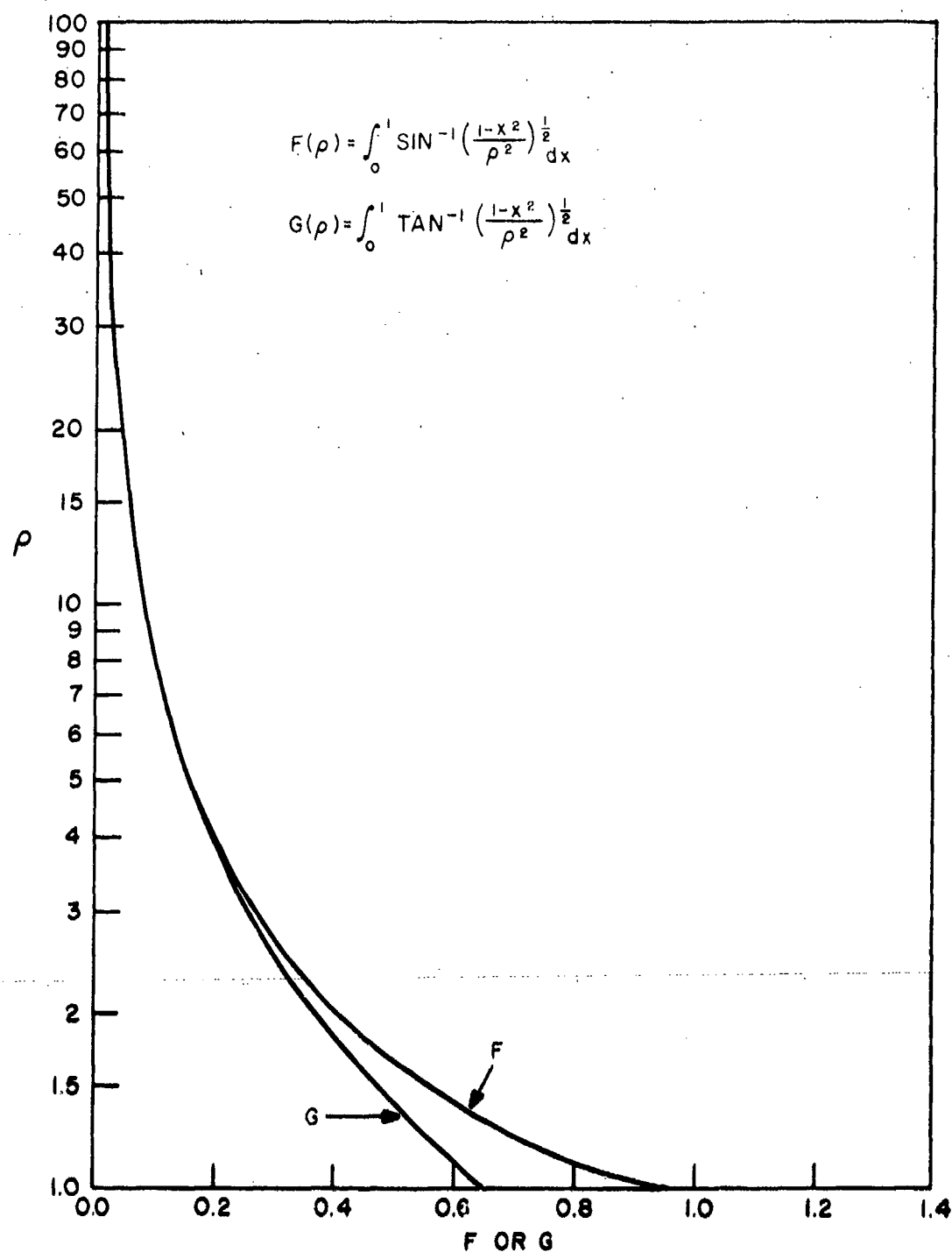
equation (A-23) yields

$$C_1 = 0.211 \text{ pF} . \quad (\text{A-24})$$

Substituting into equation (A-10) then yields

$$K_V = 9.85 \text{ V/MV} . \quad (\text{A-25})$$



Figure A-4. Plots of functions  $F(\rho)$  and  $G(\rho)$ .

## APPENDIX B.--PULSE SYNCHRONIZATION

### FIGURES

	<u>Page</u>
B-1 Setup for pulse synchronization method 1 . . . . .	109
B-2 Timing pulses obtained by synchronization method 1 . . . . .	110
B-3 Setup for pulse synchronization method 2. . . . .	111
B-4 Timing pulses obtained by synchronization method 2 . . . . .	112
B-5 Setup for pulse synchronization method 3 . . . . .	113
B-6 Timing pulses obtained by synchronization method 3 . . . . .	114

## APPENDIX B.--PULSE SYNCHRONIZATION

The three different methods employed on different occasions to accomplish synchronization of V, I, and R scope time sweeps are shown in figures B-1, B-3, and B-5. In method 1, depicted in figure B-1, each of the three Tektronix 519 oscilloscopes being used for V, I, and R is triggered separately by the High Intensity Flash X Ray (HIFX) Triggering System routinely used to trigger all the oscilloscopes in the HIFX instrument room.

It was first necessary to compensate for small differences in signal- and triggering-cable lengths between the three systems by introducing appropriate delays between arrival of triggering pulse and

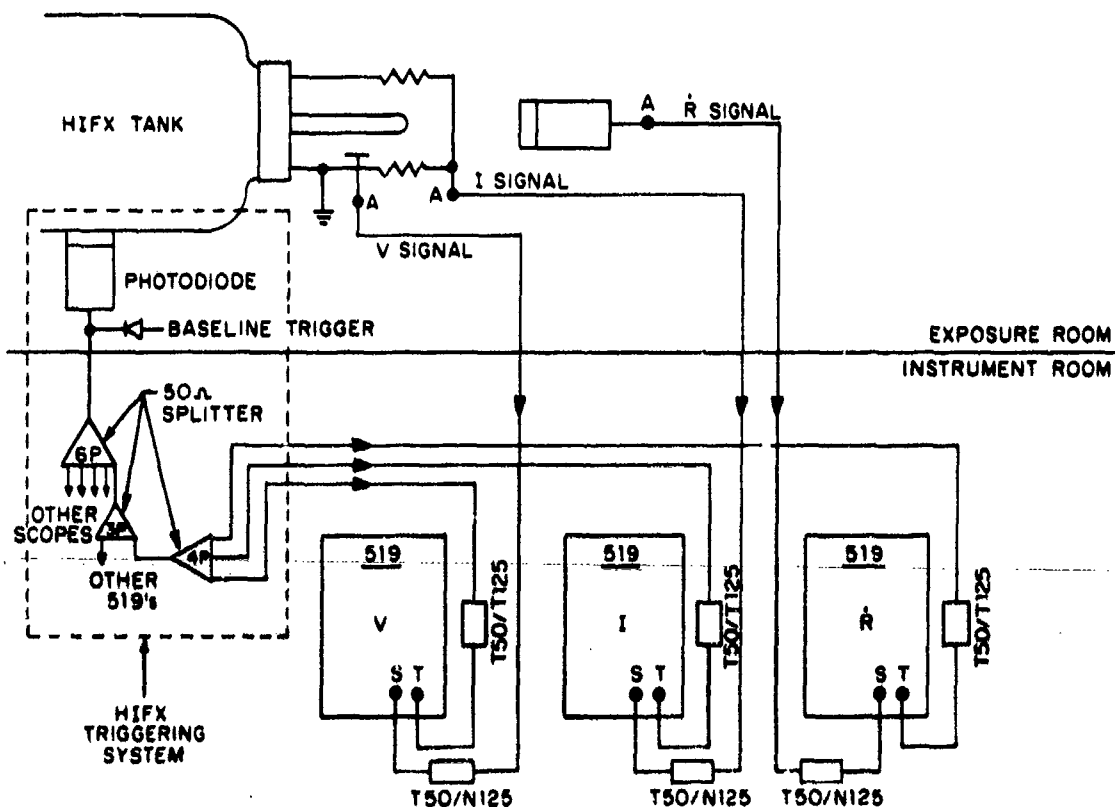


Figure B-1. Setup for pulse synchronization method 1.

# APPENDIX B

start of time-base sweep. This "tweaking" process was accomplished by observing the traces of a single pulser pulse split three ways and input to each of the systems through their respective input connectors, represented by points A in figure B-1. The setting of the time-base delay knob on each of the three oscilloscopes was varied until the three pulses were exactly time synchronized. Figure B-2 (top) shows an

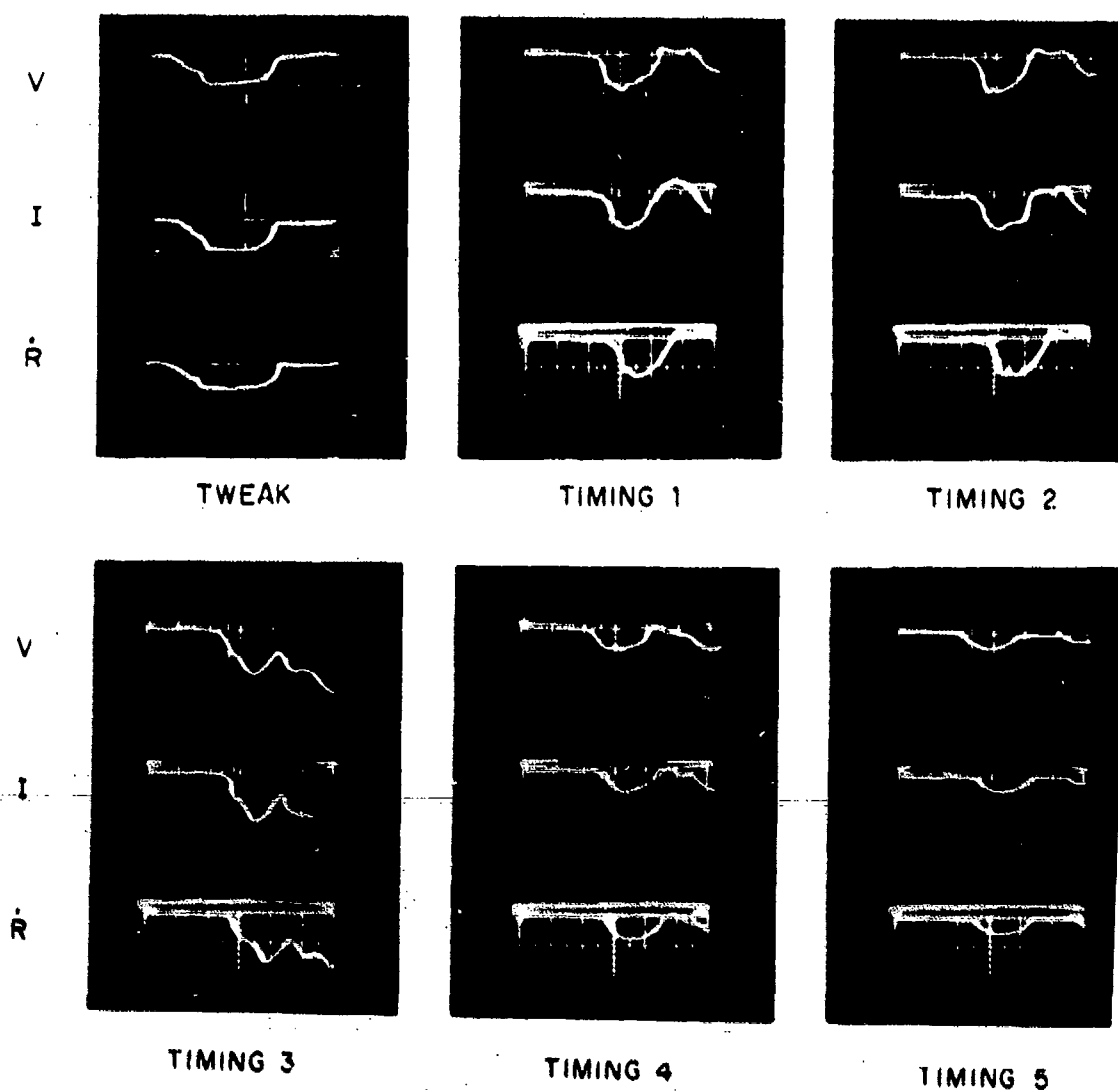
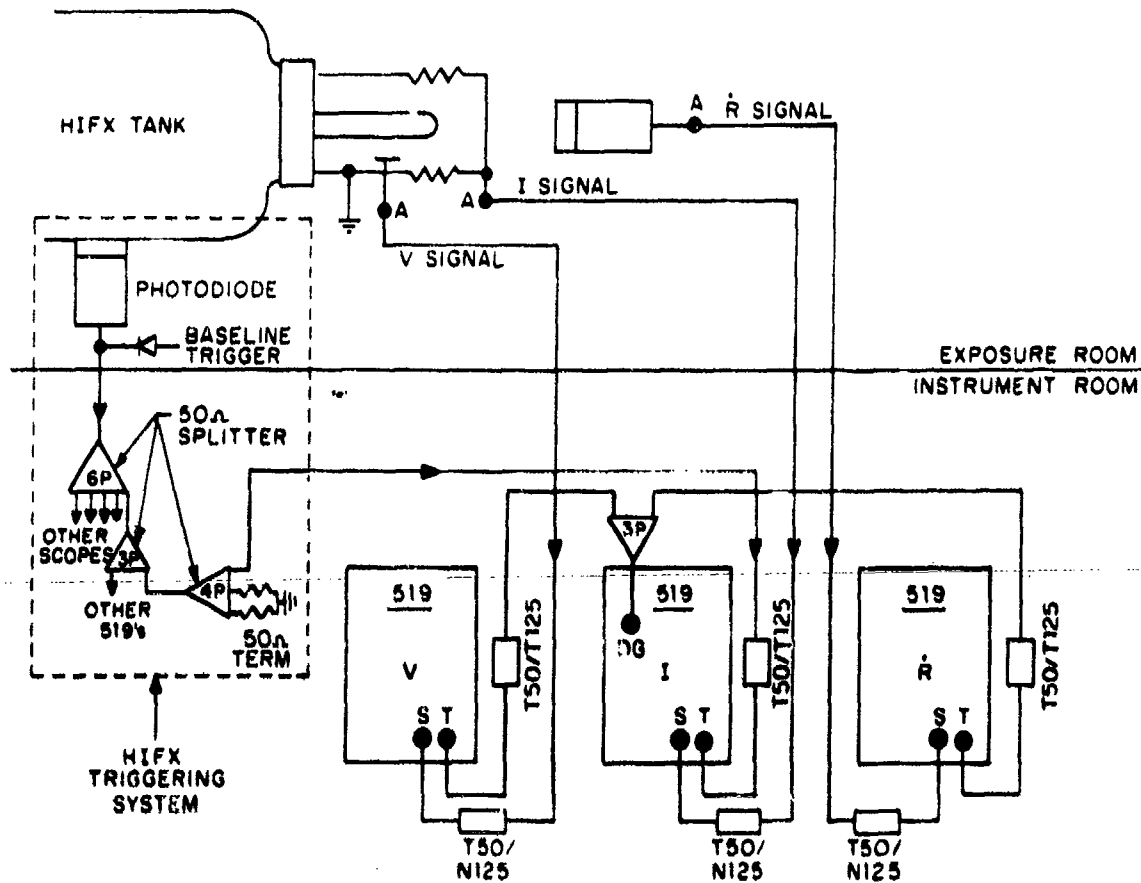


Figure B-2. Timing pulses obtained by synchronization method 1; X scale; 20 ns/div.

example of the three tweaked pulses. To check the success of the synchronization with actual monitor pulses, the signal from one of the monitors was split three ways and input to the three systems, again at points A. A sequence of timing check pulses for method 1 is also shown in figure B-2. It is evident that asynchronization to the extent of 6 or 7 ns on some shots could occur using this method.

Synchronization method 2 is shown in figure B-3. In this case only one of the three oscilloscopes (I in fig. B-3) is directly triggered by the HIFX triggering system. The other two are triggered by means of the delayed gate (DG) output of this scope. Thus,



**Figure B-3. Setup for pulse synchronization method 2.**

# APPENDIX B

synchronization of the three systems should not in any way be affected by shot-to-shot variations in the output of the HIFX Triggering System. A set of tweaked pulses and a sequence of timing check pulses using this method is shown in figure B-4. In this case, synchronization is within 4 ns.

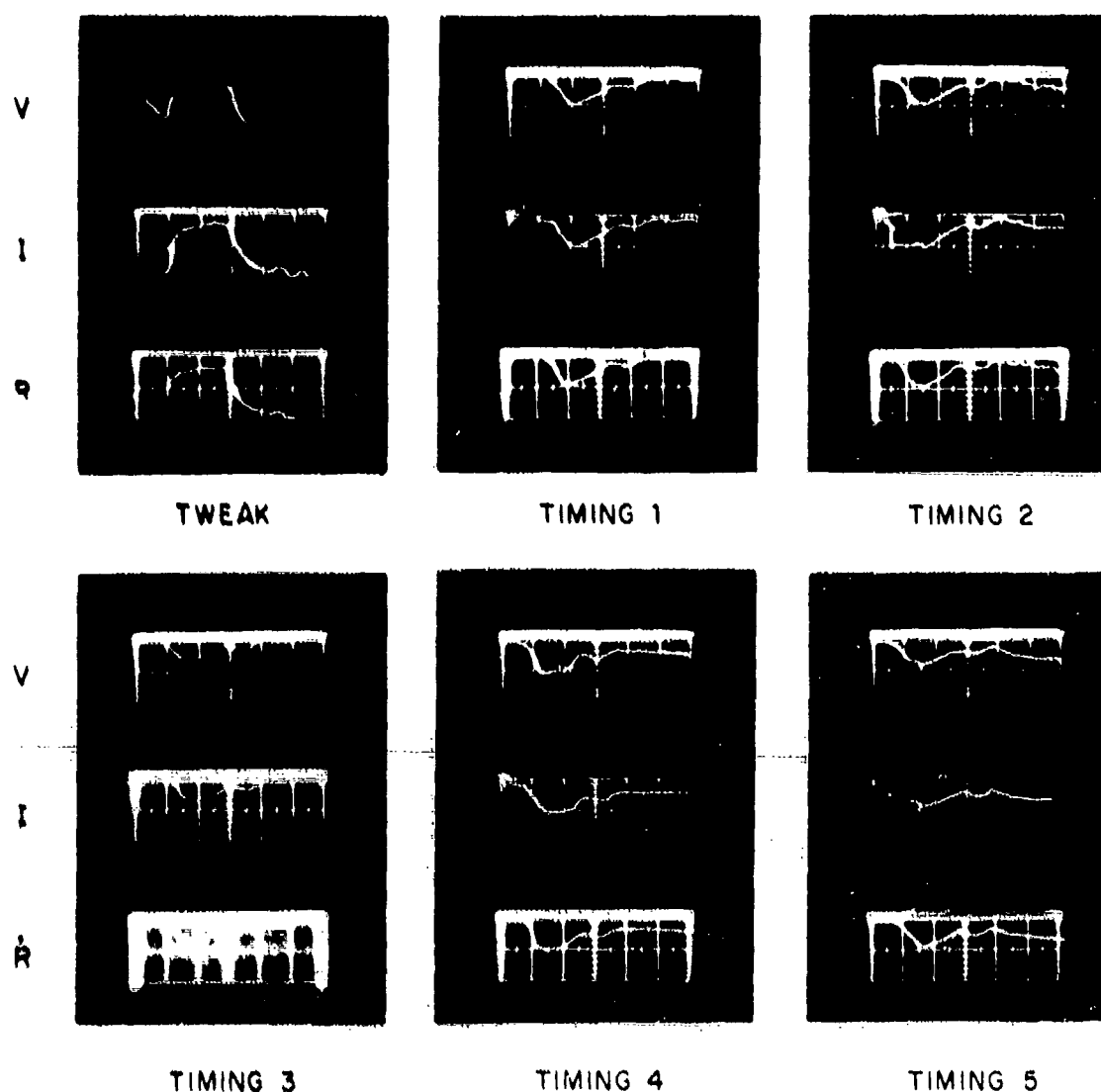


Figure B-4. Timing pulses obtained by synchronization method 2; X scale: 20 ns/div.

Synchronization method 3, shown in figure B-5, differs from synchronization method 2 in that one of the scopes is triggered by a portion of one of the monitor signals (I scope triggered by half of I signal in figure B-5) rather than by the HIFX Triggering System. Shot-to-shot reproducibility in the synchronization using this method seems to be as good as 1 ns, as is evidenced by the sequence of timing check pulses shown in figure B-6.

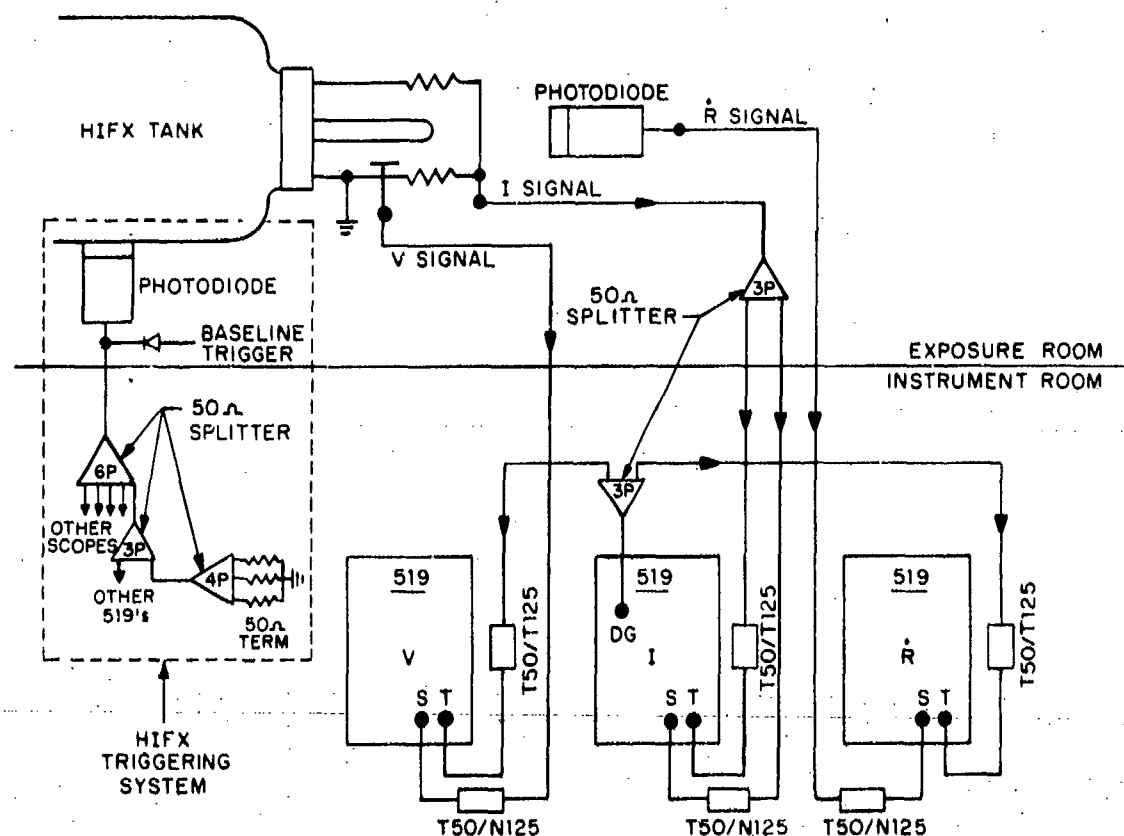


Figure B-5. Setup for pulse synchronization method 3.

# APPENDIX B

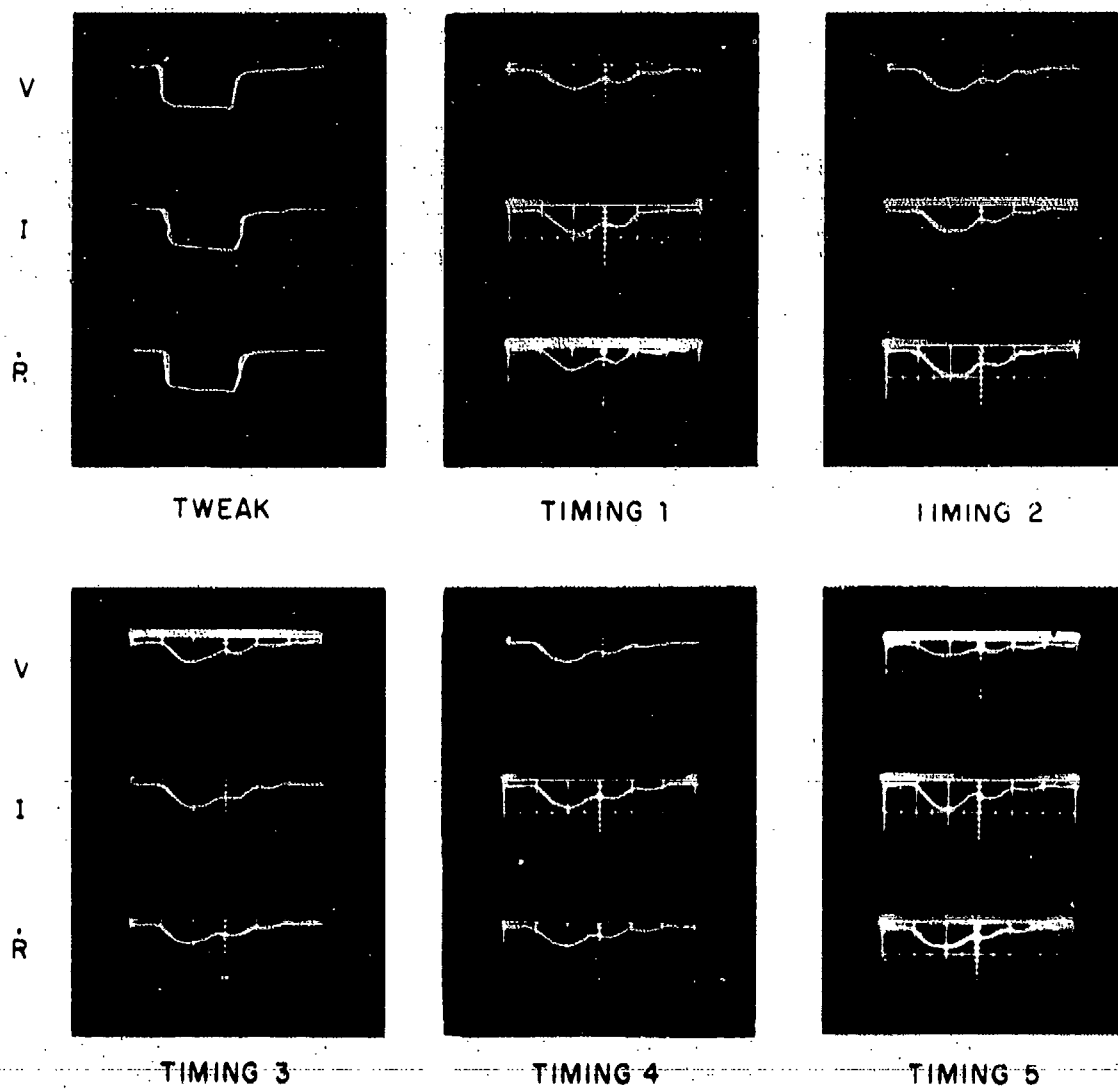


Figure B-6. Timing pulses obtained by synchronization method 3; X scale: 20 ns/div.



## APPENDIX C.--VOLTAGE-PULSE LATE TIME PHENOMENA

### FIGURES

	<u>Page</u>
C-1 High-impedance mode V pulses which do and do not return to X-axis at end of pulse . . . . .	117
C-2 High-impedance mode V pulses showing anomalous late time behavior . . . . .	118

# APPENDIX C.--VOLTAGE-PULSE LATE TIME PHENOMENA

The voltage (V) monitor pulses of figure C-1(a) (gap = 5.8 cm) at charge voltages of 4.0 and 5.0 MV do not return toward zero as do the V pulses of figure C-1(b) (gap = 1.5 cm).\* A closer investigation of this phenomenon is shown in figure C-2. Each pair of traces in this figure shows a V-monitor pulse recorded at sweep speeds of 20 and 500 ns per division. They were obtained in the high-impedance mode at various cathode-anode gaps and various charge voltages. In the upper left pair the voltage returns to zero and remains zero for all times after about 150 ns. In each of the other pulses, however, the V pulse has superimposed upon it a component which decays in many hundreds of

nanoseconds. In one of the 500 ns per division traces, the voltage repeatedly rises and decays in "sawtooth" fashion. As is evident from figure C-2, the amplitude of the slowly decaying components of the V-monitor pulse was sometimes large enough to distort the main pulse significantly. Fortu-

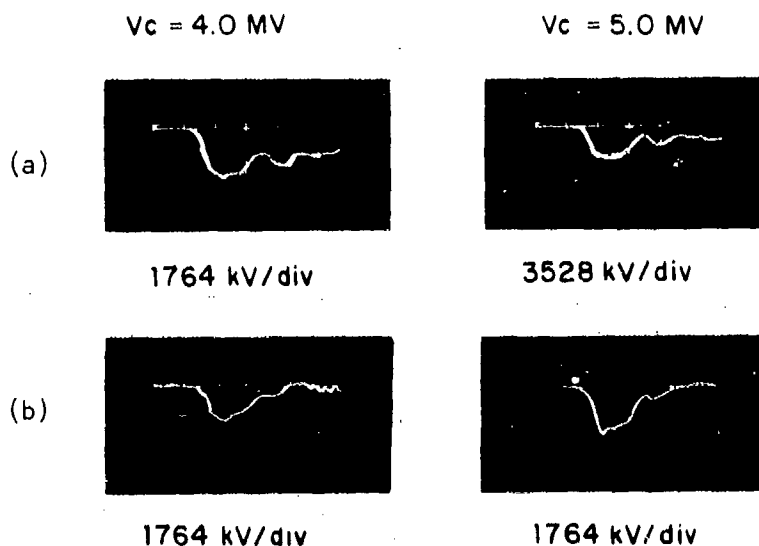


Figure C-1. High-impedance mode V pulses which do and do not return to X-axis at end of pulse; X scale: 20 ns/div (a) Gap = 5.8 cm (b) 1.5 cm

\*See also figures 20 through 23 versus figure 24 in the main body of the report.

# APPENDIX C

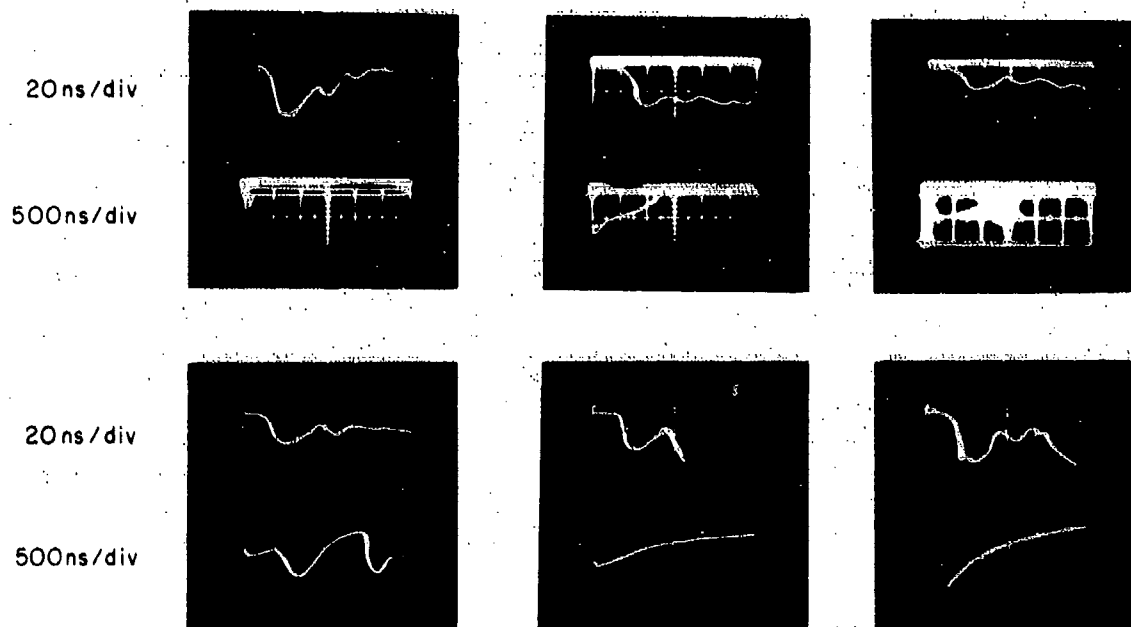


Figure C-2. High-impedance mode V pulses showing anomalous late time behavior.

nately, this was not always the case. However, at times, many high-impedance pulses had to be produced under the same machine conditions before a satisfactory V-monitor pulse could be obtained.

To interpret the late time V-monitor voltage in the same way as the main pulse would be to interpret it through\*

$$V_{out}(t) = V_{step} \left( \frac{C_1}{C_1 + C_2} \right) \left( \frac{R_{term}}{R_{term} + R_x} \right) \exp \frac{-t}{(R_{term} + R_x)(C_1 + C_2)}, \quad (C-1)$$

where

$V_{out}$  = output voltage,

$t$  = time,

$V_{step}$  = step voltage,

\*See appendix A, equation (A-1).

# APPENDIX C

- $C_1$  = shank-to-wall capacitance,
- $C_2$  = thin film capacitance,
- $R_{term}$  = a 50-ohm termination of the signal cable, and
- $R_x$  = a series resistance.

This would imply that diode voltages were sometimes even greater than the machine charge voltage and often for periods of hundreds of nanoseconds. Since there is no physical basis for such large diode voltages, these V-monitor signals would have to result from electrons impinging upon the inner capacitor plate of the monitor. However, all efforts to identify some part inside the field-emission (FE) tube as a possible source of late time electron emission failed. Such an identification was sought by substituting aluminum for the tantalum or titanium ordinarily used for the anode, for the stainless steel ordinarily used for the cathode shank and emitter, and for the lucite ordinarily used as the current (I) monitor insulator. However, these substitutions, which were made one at a time, produced changes neither in the average amplitude of the waveforms nor in the percentage of pulses in which they appeared. Other changes made in the FE tube which produced no reduction in the occurrence of these late time phenomena included variations in tube pressure below  $2 \times 10^{-4}$  Torr, variations in cathode-anode gap setting and application of various coatings to the 3.18-cm diam cathode shank, such as Dow Corning 704 fluid and polyurethane.

If there were low-energy secondary electrons contributing to the late time V signal which were emitted by some source in the vicinity of the V monitor, one should have been able to suppress them with a negative dc voltage. Negative dc potentials up to 1600 V were applied to the ungrounded plate of  $C_2$ . However, no reductions in the rate of occurrence nor in the size of the late-time signals were observed. Of course, electrons with kinetic energies greater than about 2 keV would

# APPENDIX C

not have been suppressed in these experiments. However, their transit and collection times would be much shorter than the few microseconds implied by the signals in figure C-2.

Another source of electron emission to be considered is that due to the field emission from the cathode shank itself. In general, electrons accelerating away from the shank will be turned back by the solenoidal magnetic field due to the current in the shank, causing these electrons to skip down the shank in cycloidal trajectories. A steady state analysis<sup>1</sup> of the electron trajectories in the case of concentric cylinders of inner and outer diameters  $d$  and  $D$  yields the maximum orbit diameter ( $d_{\max}$ ),

$$d_{\max} = d \exp \left[ \left( \frac{17,000}{I} \right) \left( \frac{Z/Z_o}{1 - (Z/Z_o)^2} \right) \right], \quad (C-2)$$

where diode impedance  $Z = V/I$ , and  $Z_o$  is the characteristic line impedance. In the present instance  $Z_o = 125$  ohms,  $I$  is typically 20,000 A,  $Z$  is typically 100 ohms, and  $d = 3.18$  cm. With these values equation (C-2) yields

$$d_{\max} = 20.83 \text{ cm}.$$

Thus, the electron cloud is not much smaller than the 24.5-cm diam of the HDL-built FE diode extension, and some electrons could conceivably strike the capacitor plate of the V monitor. A corresponding calculation for the low-impedance mode, for which  $I$  is typically 30,000 A,  $Z$  is typically 20 ohms, and  $d = 15.24$  cm, yields

$$d_{\max} = 20.32 \text{ cm}.$$

<sup>1</sup>J. R. Uglum, W. H. McNeill, J. E. Rizzo, and S. E. Graybill, *Research on Beam Stopping Due to Self-Magnetic Compression*, Final Report, Contract No. DASA-01-68-C0051 (November 1968).

# APPENDIX C

Thus in this case the electron cloud is probably sufficiently smaller than the 34.29-cm diam FE tube extension to prevent electrons from striking the V monitor. This great difference between  $d_{\text{max}}$  and tube extension i.d. could explain the absence of the late-time waveforms in low-impedance pulses.

A difficulty in explaining the late-time V-monitor waveforms in terms of charging due to field-emitted electrons, however, lies in the fact that the abrupt deposition of charge,  $-Q$ , due to these electrons on the V-monitor capacitor, should occur simultaneously with the abrupt rise in diode voltage. The net result of such a charge on the V-monitor signal would be simply an addition to the amplitude given in equation (C-1):

$$V_{\text{out}}(t) = \left( V_{\text{step}} + \frac{Q}{C} \right) \left( \frac{C_1}{C_1 + C_2} \right) \left( \frac{R_{\text{term}}}{R_{\text{term}} + R_x} \right) \exp \left\{ -t / \left[ (R_{\text{term}} + R_x) (C_1 + C_2) \right] \right\} \quad (\text{C-3})$$

Thus the pulse would rise and decay at the same rates as the main diode-voltage pulse, contrary to what is observed.

It is possible that one might obtain V pulses in the high-impedance mode without the complication of the large late-time components experienced here by using a voltage-divider-type V monitor fashioned after the design of one used for some low-impedance diodes,<sup>2</sup> if one could be built to withstand 3 MV or more.

<sup>2</sup>G. Yonas and P. Spence, *Experimental Investigations of High v/γ Electron Beam Transport*, Physics International PR-106 (1968).

# DISTRIBUTION

DEFENSE DOCUMENTATION CENTER  
CAMERON STATION, BUILDING 5  
ALEXANDRIA, VA 22314  
ATTN DDC-TCA (12 COPIES)

COMMANDER  
USA RSCH & STD GP (EUR)  
BOX 65  
FPO NEW YORK 09510  
ATTN LTC JAMES M. KENNEDY, JR.  
CHIEF, PHYSICS & MATH BRANCH

COMMANDER  
US ARMY MATERIEL DEVELOPMENT  
& READINESS COMMAND  
5001 EISENHOWER AVENUE  
ALEXANDRIA, VA 22333  
ATTN DRXAM-TL, HQ TECH LIBRARY  
ATTN DRCLDC, MR. JIM BENDER

COMMANDER  
US ARMY ARMAMENT MATERIEL  
READINESS COMMAND  
ROCK ISLAND ARSENAL  
ROCK ISLAND, IL 61201  
ATTN DRSAR-ASF, FUZE & MUNITIONS SPT DIV

COMMANDER  
USA MISSILE & MUNITIONS CENTER & SCHOOL  
REDSTONE ARSENAL, AL 35809  
ATTN ATSK-CTD-F

DIRECTOR  
DEFENSE NUCLEAR AGENCY  
WASHINGTON, DC 20305  
ATTN RAEV  
ATTN DDST, DR. ED CONRAD  
ATTN SPAS  
ATTN STVL  
ATTN RATN

DIRECTOR  
BALLISTICS RESEARCH LABORATORY  
ABERDEEN PROVING GROUND, MD 21005  
ATTN DRXAR-TE, MR. JULIUS MESZAROS

DIRECTOR  
ADVANCED BALLISTIC MISSILE DEFENSE AGENCY  
5001 EISENHOWER AVENUE  
ALEXANDRIA, VA 22333  
ATTN MR. ARCHIE GOLD

DEPUTY CHIEF OF STAFF  
FOR OPERATIONS AND PLANS  
TELECOMMUNICATIONS COMMAND  
AND CONTROL DIRECTORATE  
DEPARTMENT OF THE ARMY  
WASHINGTON, DC 20314  
ATTN DAMO-TOZ, TECH ADVISER,  
DR. P. J. KENNY

DEPUTY CHIEF OF STAFF FOR RESEARCH, DEVELOPMENT  
AND ACQUISITION  
DEPARTMENT OF THE ARMY  
WASHINGTON, DC 20310  
ATTN DAMA-AR, CHIEF SCI. DA AND DIR OF ARMY  
RESEARCH, DR. M. E. LASSER  
ATTN DAMA-AR, RESEARCH PROGRAMS  
ATTN DAMA-CSS-D, RESEARCH AND DEVELOPMENT TEAM  
ATTN DAMA-CSM-N, MUNITIONS DIV., NUCLEAR TEAM

COMMANDING GENERAL  
US ARMY ELECTRONICS COMMAND  
FORT MONMOUTH, NJ 07703  
ATTN DRSEL-TL-EN, DR. STANLEY KRONENBERG  
ATTN DRSEL-TL-IR/B, MR. R. FREIBERG

COMMANDER  
USA STACOMA  
FORT MONMOUTH, NJ 07703  
ATTN MR. BERNARD D. DONZ/BLDG 209

DIRECTOR  
US ARMY MATERIEL SYSTEMS ANALYSIS ACTIVITY  
ABERDEEN PROVING GROUND, MD 21005  
ATTN DRXSY-S, MR. MARK RECHES

COMMANDER  
US ARMY TEST AND EVALUATION COMMAND  
ABERDEEN PROVING GROUND, MD 21005  
ATTN DRSTE-FA, MR. RUSS GALASSO

US ARMY NUCLEAR AGENCY  
BLDG 2073, NORTH AREA  
FT. BELVOIR, VA 22060  
ATTN MAJ LIND

COMMANDER  
WHITE SANDS MISSILE RANGE  
WHITE SANDS, NM  
ATTN STEWS TE-AN, MR. B. K. CUMMINGS

COMMANDER  
ARMAMENTS RESEARCH AND DEVELOPMENT COMMAND  
BLDG 65  
DOVER, NJ 07801  
ATTN LCWSL, MR. M. A. RAVOTTO

OFFICE PROJECT MANAGER NUCLEAR MUNITIONS  
DOVER, NJ 07801  
ATTN MR. MELVIN MORGAN

US ARMY TANK AUTOMOTIVE R&D COMMAND  
28251 VAN DYKE  
WARREN, MI 48090  
ATTN DRDTA-RMC, MR. PIESCZAK

US ARMY BALLISTIC MISSILE ADVANCED  
TECHNOLOGY CENTER  
P.O. BOX 1500  
HUNTSVILLE, AL 35805  
ATTN BMDATC-T, MAJ SIDNEY W. WINSLOW

DISTRIBUTION (Cont'd)

HQ DEPARTMENT OF THE ARMY  
ODCSOPS  
WASHINGTON, DC 20301  
ATTN DAMO-SSN, MAJ SKERKER, RM 3B534

OSD-ODDRSE (TWP-LWO)  
RM 3E1025, THE PENTAGON  
WASHINGTON, DC 20301  
ATTN MR. K. R. STURDIVANT

DEFENSE NUCLEAR AGENCY, FIELD COMMAND  
KIRTLAND AFB, NM 87115  
ATTN MAJ J. N. PETERSON

OFFICE OF THE ASST SECRETARY OF DEFENSE  
(ATOMIC ENERGY)  
ROOM 3C124, THE PENTAGON  
WASHINGTON, DC 20301  
ATTN COL EDWARD J. PALANEK, USAF

COMMANDER  
NAVAL SURFACE WEAPONS CENTER/WOL  
SILVER SPRING, MD 20910  
ATTN CODE WA52, MR. ANDY SMITH, BLDG 132  
ATTN CODE WA52, DR. JED SAZAMA, BLDG 132  
ATTN CODE WX21, TECH LIBRARY, RM L-321  
ATTN CODE WR43, DR. LOUIS LIBELO

COMMANDER  
NAVAL RESEARCH LABORATORY  
WASHINGTON, DC 20375  
ATTN CODE 6654, MR. E. C. JONES  
ATTN CODE 7720, DR. G. COPPERSTEIN  
ATTN CODE 2620, LIBRARY

NAVAL SHIP ENGINEERING CENTER  
WASHINGTON, DC 20362  
ATTN CODE 6105D, MR. ROBERT E. FUSS

SUPERINTENDENT  
NAVAL POSTGRADUATE SCHOOL  
MONTEREY, CA 93940  
ATTN CODE 2124, TECH REPORTS

AF INSTITUTE OF TECHNOLOGY, AU  
WRIGHT-PATTERSON AFB, OH--45433  
ATTN TECH LIBRARY

AF WEAPONS LABORATORY  
KIRTLAND AFB, NM 87117  
ATTN TREF

COMMANDER  
AIR FORCE WEAPONS LABORATORY  
KIRTLAND AFB, NM 87117  
ATTN OVV, CPT JOHN MONAHAN  
ATTN AFWL-NSEW, MR. ROBERT O. SMITH  
ATTN AFTEC/TEZ, LT COL WILLIAM H. CARROLL, JR.

SANDIA LABORATORIES  
P.O. BOX 5800  
ALBUQUERQUE, NM 87115  
ATTN TECH LIBRARY

THE BOEING COMPANY  
P.O. BOX 3707  
SEATTLE, WA 98124  
ATTN MR. JOHN ADAMSKY (BREL)

SIMULATION PHYSICS, INC.  
PATRIOTS PARK  
BEDFORD, MA 01730  
ATTN MR. ROGER LITTLE

ION PHYSICS CORPORATION  
BURLINGTON, MA 01803  
ATTN DR. HELMUTH MILDE

HARRY DIAMOND LABORATORIES  
ATTN RAMSDEN, JOHN J., LTC, COMMANDER/  
FLYER, I.N./LANDIS, P.E./  
SOMMER, H./OSWALD, R. B.  
ATTN CARTER, W.W., DR., TECHNICAL  
DIRECTOR/MARCUS, S.M.  
ATTN KIMMEL, S., PAO  
ATTN CHIEF, 0021  
ATTN CHIEF, 0022  
ATTN CHIEF, LAB 100  
ATTN CHIEF, LAB 200  
ATTN CHIEF, LAB 300  
ATTN CHIEF, LAB 400  
ATTN CHIEF, LAB 500  
ATTN CHIEF, LAB 600  
ATTN CHIEF, DIV 700  
ATTN CHIEF, DIV 800  
ATTN CHIEF, LAB 900  
ATTN CHIEF, LAB 1000  
ATTN RECORD COPY, BR 041  
ATTN HDL LIBRARY (5 COPIES)  
ATTN CHAIRMAN, EDITORIAL COMMITTEE  
ATTN CHIEF, 047  
ATTN TECH REPORTS, 013  
ATTN PATENT LAW BRANCH, 071  
ATTN GIDEP OFFICE, 741  
ATTN LANHAM, C., 0021  
ATTN CHIEF, BR 210  
ATTN CHIEF, BR 230  
ATTN CHIEF, BR 280  
ATTN CHIEF, BR 290  
ATTN SILVERSTEIN, J. D., 290 (12 COPIES)  
ATTN STEWART, A. G., 290  
ATTN GRAYBILL, S. E., 290